

Design of concrete-filled steel tube composite columns with cores consisting of high-strength laminated steel plates

Michael Schäfers, M.Sc.

Vollständiger Abdruck der von der TUM School of Engineering and Design der Technischen Universität München zur Erlangung eines

Doktors der Ingenieurwissenschaften (Dr.-Ing.)

genehmigten Dissertation.

Vorsitz: Prof. Dr.-Ing. Oliver Fischer

Prüfende der Dissertation:

1. Prof. Dr.-Ing. Martin Mensinger
2. Prof. Dr.-Ing. Markus Schäfer
3. Prof. Dr.-Ing. Markus Feldmann

Die Dissertation wurde am 03.06.2024 bei der Technischen Universität München eingereicht und durch die TUM School of Engineering and Design am 18.12.2024 angenommen.

PREFACE

This thesis results from my employment as Research Associate at the Chair of Metal Structures at the Technical University of Munich in the years 2020 to 2024 under the supervision of Professor Dr.-Ing. Martin Mensinger. My sincerest gratitude goes to Prof. Mensinger for the supervision and for providing me with this research topic.

The research work was carried out as part of the IGF research project "Composite columns with laminated steel plates made of high-strength steels for building construction" (IGF 21366 N, FOSTA No. P1500). I would like to thank the research association and all industrial partners for their support. In the course of the work, numerous Bachelor's and Master's theses as well as student assistant work was supervised, and I would like to express my sincere thanks for the eager commitment of the students.

I would also like to thank Dr.-Ing. Norbert Sauerborn for mentoring this dissertation and for the numerous technical discussions.

I thank Prof. Dr.-Ing. Oliver Fischer for chairing the examination committee. Further, I would like to express my gratitude to Professor Dr.-Ing. Markus Schäfer for the discussions and for taking on the review of this work. I would also like to thank Professor Dr.-Ing. Markus Feldmann to be available as third reviewer.

I would like to thank my colleagues in the department for the time we spent together, full of discussions, suggestions, and mutual support.

Finally, I want to thank my family Sabine, Hans-Joachim, Sebastian, Frederik, Paulina and most importantly Vanessa for their unconditional love, understanding, support, and reliance at any time of the day or night.

Munich, May 2024

Michael Schäfers

ZUSAMMENFASSUNG

Die Anforderungen an Tragwerke im modernen Hochbau liegen zunehmend in einer optimierten Material- und Kosteneffizienz sowie der Konstruktion schlanker und damit platzsparender Bauweisen. Stahl-Beton-Verbundbauten sind bereits seit Langem eine etablierte Lösung aufgrund ihrer brandsicheren und hochtragfähigen Eigenschaften. Durch den Einsatz hochfester Stähle eröffnen sich trotz bislang eingeschränkter Verfügbarkeit dabei weitere Möglichkeiten zur Erhöhung der Tragfähigkeit. Im Zuge eines Forschungsprojekts („Blechlammellenstützen aus hochfesten Stählen für den Hochbau“, IGF-Nr. 21366 N) wurde eine neuartige Stahl-Beton-Verbundstütze entwickelt, bestehend aus einem Kern aus zusammengesetzten Blechlammellen in einem Hohlprofil mit Betonfüllung. Sowohl für das Kern- als auch für das Hohlprofil wurden hochfeste Stähle verwendet, für den Füllbeton wurde ein normalfester Beton genutzt. Der Verbund zwischen einzelnen Blechlammellen wurde gezielt mit vorgespannten Schrauben oder einem gezielten Einsatz von Schweißnähten hergestellt.

Die für das Tragverhalten entscheidenden Faktoren sind die aktivierbare Biegesteifigkeit der Stützenkonstruktion sowie der Einfluss geometrischer und struktureller Imperfektionen. Es wurden daher großmaßstäbliche Knickversuche mit exzentrischer Lasteinleitung sowie Vierpunktbiegeversuche durchgeführt. Durch die Kombination hochfester Stahlbleche und Rohre konnten erwartungsgemäß hohe Traglasten erzielt werden. Weiter konnte ein größerer Einfluss durch verlängerte Schweißnähte auf die Biegesteifigkeit beobachtet werden. Die Schraubenverbindungen zeigten nur eine geringfügige Erhöhung der Biegesteifigkeit. Die für das Stabilitätsverhalten entscheidenden Eigenspannungszustände der hochfesten Stahlbleche wurden durch zerstörende und zerstörungsfreie Verfahren ermittelt. Es zeigten sich hohe Zugeigenspannungen an den Brennschnittkanten, die im Gleichgewicht mit niedrigen Druckeigenspannungen in der Blechmitte standen. Die insgesamt geringeren Eigenspannungen führten zur Zuordnung einer vorteilhafteren Knicklinie gegenüber normalfesten Stahlblechen. Basierend auf Betondruck- und Stahlzugversuchen wurden geometrisch und materiell nichtlineare Finite Elemente Modelle validiert und verifiziert. Mithilfe parametrischer Modelle konnten detaillierte Untersuchungen an den Stützen durchgeführt werden. Es zeigte sich ein Einfluss auf die Biegesteifigkeit der Stützenquerschnitte aus der Länge der nicht verbundenen Bereiche der einzelnen Lamellen. Ein weiterer Einfluss resultierte aus der Normalkraftbeanspruchbarkeit des Kernprofils im Verhältnis des Gesamtquerschnitts. Durch eine optimierte Anordnung unterbrochener Schweißnähte konnte die Biegesteifigkeit der Stützen gezielt erhöht werden. Mit einem modifizierten Ansatz zur rechnerischen Bestimmung der Biegesteifigkeit wurde eine Bemessung mithilfe der Europäischen Knicklinien ermöglicht. Für den neuartigen Stütztyp zeigte sich eine hohe

Übereinstimmung mit Knicklinie a_0 . Die Berücksichtigung von geometrischen Imperfektionen in Form von exzentrischen Kernpositionen, wie sie in den experimentellen Versuchen festgestellt wurden, ergab eine Zuordnung zur Knicklinie a .

Die vorgestellten Ergebnisse stellen erste Forschungserkenntnisse zu einem neuartigen hochtragfähigen Verbundstützentyp dar. Die Untersuchungen wurden auf eine Kombination von zwei Stahlgüten und einer Betonfestigkeitsklasse fokussiert und sind dahingehend limitiert. Für eine generalisierte Anwendbarkeit des vorgeschlagenen Vorgehens zur Bemessung sind zusätzliche Untersuchungen notwendig. Weiterhin hat sich die unausweichliche Montagetoleranz des Kernprofils mit einem maßgebenden negativen Einfluss der Tragfähigkeit gezeigt. Für eine systematische Berücksichtigung dieser Imperfektion bedarf es eine statistische Überprüfung der zu berücksichtigenden Annahmen.

Die Arbeit stellt neuartige Erkenntnisse zum Tragverhalten und zur Beeinflussung der Biegesteifigkeit eines innovativen Stützentyps dar. Insbesondere der Einsatz hochfester Stähle ermöglicht eine Steigerung möglicher Tragfähigkeiten, verstärkt durch geringere Einflüsse aus strukturellen Imperfektionen.

ABSTRACT

Demands in modern building construction are increasing for material and cost efficiency as well as optimized space consumption of the structure. Steel-concrete composite structures offer firesafe and advantageous structural performance for such structures. The use of high-strength steel offers the potential to design improved structures, although its availability of sizes is limited. As a novel approach, a composite column consisting of laminated high-strength steel plates inside a high-strength tubular hollow section and concrete confinement was developed as part of a research project ("Laminated steel plate columns with high-strength steels for building construction", IGF-No. 21366 N). The individual plates in the core section were connected locally with targeted bolts or welds.

Decisive factors for the load-bearing behavior are the effective flexural stiffness as well as influences of structural and geometric imperfections. In the course of the research, large scale tests of fabricated columns were executed under uniaxial bending and compression as well as under four-point bending. The use of high-strength steel plates and high-strength tubular sections resulted in high load bearing capacities, as expected. Further, an increasing flexural stiffness could be observed with longer welds. Bolted connections of the plates showed only minor increases of flexural stiffness. Additionally, experimental investigations were conducted to assess the residual stresses in thick high-strength plates. The high-strength steel plates cut by oxy-fuel cutting showed high tensile stresses at the cut edges equilibrated by low compressive stresses in the middle section. The smaller residual stresses lead to a more favorable buckling behavior of the plates compared to normal-strength steel plates. Based on concrete compression tests and steel coupon tests, a developed finite element model was verified and validated. Parametric studies investigating alternated sections complemented the scope of research. These investigations revealed the free length between welded segments to be decisive for the effective flexural stiffness. Furthermore, the ratio of plastic resistance to axial force of the core section to the total section showed significant influence on the flexural stiffness. Optimized localization of discontinuous welds reached a targeted increase of flexural stiffness. A modified approach to calculate the effective flexural stiffness was proposed considering these factors. The use of this modified approach suggested the application of the European buckling curve a_0 for columns with centric core position. The consideration of an eccentric position of the core section, observed in the experiments, allowed an assignment to buckling curve a .

The presented results are limited by several aspects: the research was focused on a single combination of steel grades and concrete strengths and only conducted limited numerical calculations. An empirical evaluation of the results could not be executed due to the limitations

and thus the suggested concept must be verified with a wider range of numerical investigations. The experimental buckling tests revealed the significant influence of a non-centric position of the core profile. For a design concept, this should be accounted for but lacks statistically assured assumptions.

This work presents insights into the load-bearing behavior and the flexural stiffness of the novel construction method. Particularly the use of high-strength steel has led to a significant enhancement in column strengths.

TABLE OF CONTENT

1	Introduction	17
2	Review of the literature	22
2.1	Buckling of steel and steel-concrete composite members	22
2.2	Current research and design of composite columns	25
2.3	Research on residual stresses in steel plates	29
3	Experimental investigations	34
3.1	HSLP composite columns under compression and uniaxial bending	36
3.2	HSLP composite columns under four-point bending	49
3.3	Geometric imperfection measurements of HSLP composite columns	57
3.4	Residual stress measurements of high-strength steel plates	60
3.5	Discussion of the experimental results	67
4	Numerical investigations	71
4.1	Model setup	71
4.2	Verification and validation on experimental tests	75
4.3	Buckling behavior of high-strength flame-cut steel plates	80
4.4	Buckling behavior of high-strength tubular sections	81
4.5	Parametric investigation	82
4.5.1	Flexural stiffness of HSLP composite columns under pure bending	86
4.5.2	Flexural stiffness of HLSP composite columns under compression	87
4.5.3	Comparison of HSLP composite columns under bending and under compression	91
4.5.4	Eccentrically loaded HSLP composite columns under compression	93
4.6	Comparison of the numerical results to the European buckling curves	95
4.7	Discussion of the numerical results	101
5	Conclusion	105
	List of Tables	109
	Table of Figures	111
	Literature	115

SYMBOLS AND ABBREVIATIONS

Abbreviations and units

<i>3D</i>	Three-dimensional
<i>bc</i>	Buckling curve
<i>BE</i>	Beam element
<i>BR</i>	Bending test
<i>CDP</i>	Concrete damaged plasticity model
<i>CFST</i>	Concrete-filled steel tubes
<i>EC 0</i>	EN 1990
<i>EC 3-1-1</i>	EN 1993-1-1
<i>EC 4-1-1</i>	EN 1994-1-1
<i>GMNIA</i>	Geometrically and materially nonlinear analysis with imperfections included
<i>GPa</i>	Gigapascal
<i>HSLP</i>	High-strength laminated steel plates
<i>kN</i>	Kilonewton
<i>ksi</i>	Kilopound per square inch
<i>KR</i>	Buckling test
<i>LVDT</i>	Linear variable differential transformers
<i>m</i>	Meter
<i>mm</i>	Millimetre
<i>MN</i>	Meganewton
<i>MPa</i>	Megapascal
<i>N</i>	Newton

Symbols

α	Interaction factor for individual steel plates
δ	Chord height of camber
δ_c	Steel contribution ratio
Δl	Length difference
ε	Strain
ε_{c1}	Compressive strain in the concrete at the peak stress f_c
ε_{corr}	Correcting strain of the chord length
ε_{ctm}	Strain at mean axial tensile strength of concrete
ε_{cu}	Ultimate compressive strain in the concrete
ε_m	Strain of the middle fibre
κ	Curvature
λ	Wavelength
$\bar{\lambda}$	Relative slenderness
μ	Friction coefficient

ν	Poisson's ratio
θ	Radiation angle
σ_c	Compressive residual stresses
σ_r	Tensile residual stresses equivalent to yield strength.
σ_{RS}	Residual stress
$\varphi_{y,bottom,Nu}$	Bearing rotation around y-axis of bottom bearing at ultimate load
$\varphi_{y,top,Nu}$	Bearing rotation around y-axis of top bearing at ultimate load
χ	Reduction factor for flexural buckling
ψ	Dilatation angle
a_w	Weld thickness
b	Width of the zone with compressive residual stresses
c	Width of the zone with tensile residual stresses
c_{Ph}	Horizontal spring stiffness
c_{Pv}	Vertical spring stiffness
d	Distance of the atomic lattice
d_c	Damage parameter under compression
d_t	Damage parameter under tension
D	Ductility parameter
e_0	Load eccentricity
e_{0d}	Sinusoidal bow imperfection
e_{0K}	Eccentricity of the core profile
E_a	Modulus of elasticity of structural steel
E_c	Modulus of elasticity of concrete
E_{cm}	Secant modulus of elasticity of concrete
E_s	Modulus of elasticity of reinforcement steel
$(EI)_{eff}$	Effective flexural stiffness for calculation of relative slenderness
$(EI)_{eff,II}$	Effective flexural stiffness for use in second-order analysis
$(EI)_{a,k,St.}$	Flexural stiffness of activated Steiner terms of the core section
$(EI)_{a,k,St.,100\%}$	Flexural stiffness of the core section's Steiner terms at 100 % shear interaction
$(EI)_{a,k,FEM}$	Flexural stiffness of the core section from FEM
$(EI)_{a,k,Eigen}$	Flexural stiffness of the principal moments of inertia
$(EI)_{a,k,100\%}$	Flexural stiffness of the core section at 100 % shear interaction
F	Acting load
f_{cd}	Design value of concrete compressive strength
f_{ck}	Characteristic compressive cylinder strength of concrete at 28 days
f_{cm}	Mean value of concrete cylinder compressive strength
f_{ctk}	Characteristic axial tensile strength of concrete
f_{ctm}	Mean value of axial tensile strength of concrete
f_y	Yield strength

f_{yd}	Design value of the yield strength
I_a	Area moment of inertia of structural steel
I_c	Area moment of inertia of concrete
I_s	Area moment of inertia of reinforcement steel
K_e	Correction factor
l	Column length
l_{after}	Length after sectioning
l_{before}	Length before sectioning
l_{cr}	Critical buckling length
$l_{reference}$	Reference length
l_w	Length of the weld
L	Length measurement of the chord
n_w	Number of welds
$N_{b,Rd}$	Design value of buckling resistance
N_{cr}	Critical buckling load
N_E	Acting compressive load
$N_{pl,Rk}$	Characteristic plastic resistance to compression
$N_{pl,Rk}$	Design value of plastic resistance to compression
N_r	Compressive axial force resistance
N_u	Ultimate load
M_E	Acting bending moment
M_{Nu}	Acting bending moment at ultimate load
M_r	Bending resistance moment
P	Acting compressive load in Southwell's plot
RO	Diameter of tubular hollow section
$R_{p,0.2}$	Proof strength, stress at 0.2 % plastic strain
t	Plate thickness
u_x	Deformation in x-direction
$u_{x,Nu}$	Deformation in x-direction at ultimate load
v	Horizontal deformation in Southwell's plot
$w(x)$	Vertical deformation at midspan
w_0	Bow imperfection

Indices

κ	Section curvature
a	Structural steel
a,k	Core profile made of structural steel
a,h	Hollow section made of structural steel
BE	Bending equation
SW	Southwell's plot

1 Introduction

Since the sedentarization during the Neolithic Revolution, people began to assemble wooden and stone elements, using ground posts as beam columns, to build a roof structure over the formed living space. First advanced civilizations erected buildings using stone construction methods, further developed by the Roman *opus caementium* as a precursor to today's concrete. In the Middle Ages, the emergence of timber framing placed wooden columns at the center of architecture with the post-and-beam construction method. For the first time, it was possible to build several floors on top of each other in this way. With urban developments and higher story buildings, the demands on the materials used increased, while the traditional building materials had limited load-bearing capacities. Cast steel, which was first successfully used as structural element in the Iron Bridge in 1778, proved to be particularly useful for components subjected to compressive loads such as columns. The susceptibility of the newly invented steel columns to heat and the associated loss of strength in the event of fire was taken by Peter Wight in 1857 as an opportunity to design new types of columns with fireproof blocks as fire protection cladding (Figure 1-1). This protected iron column was developed in consequence of the Chicago Fire of 1874 and the following cancellation of fire insurance policies for all buildings in the city. This innovation of a fire-proof column revolutionized building construction and laid the foundation for present-day American skylines as the first composite column.

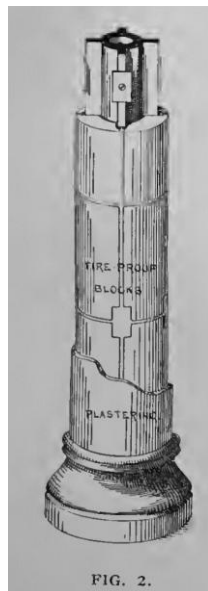


Figure 1-1 Fire safe iron column of Peter Wight from 1857, from [1].

Today's architectural requirements for the supporting structure of new buildings often demand for in a slender construction and free arrangement of the spanned space. The conversion of

existing buildings also requires a flexible floor plan design. By minimizing restrictions on the floor design, existing buildings can continue to be used sustainably and resource-intensive new buildings can be avoided. Due to the service life of 50-100 years generally expected of buildings, every new building must also be considered as a future existing building. This means that columns play a central role in modern building construction. Increasing building heights of up to 900 m additionally place high demands on the load bearing capacity of vertical components.

Composite columns have proven themselves as feasible alternatives for vertical elements: they consist of a combination of a steel profile and reinforced concrete. The large flexural stiffness of the steel is complemented with a fire-safe load bearing capacity of the concrete. The composition can be implemented in numerous forms, as a rolled profile with concrete casing or hollow profile with concrete filling. The use of an encasing steel profile enables a confinement effect and additional stabilization of the concrete. An additional further development involves the use of a steel core in the concrete-filled steel tube. This combination of steel tube, steel core and concrete filling in particular is an efficient method that enables a high degree of prefabrication, fast erection and simultaneously high load-bearing capacities with small cross-sectional dimensions. The use of concrete-filled steel tubes can also increase ductility when the ultimate load is reached.

One key limitation of current composite column constructions is the restricted load bearing capacity due to cross-sectional design with rolled profiles. Efforts to increase the proportion of steel cross-section and thus the load bearing capacity have led to the use of solid profiles in concrete or hollow profiles encased in concrete. However, these types of composite columns are severely limited: the use of profiles, especially solid profiles, is restricted by the maximum available dimensions. Furthermore, the calculable strength of the steel must be reduced from a product thickness of 40 mm and above, according to prEN 1993-1-1:2020-08 [2] (EC 3-1-1), which would result in a reduced efficiency of the steel cross-section. In addition, the residual stresses of round and square solid profiles increase with the diameter [3]. One approach to avoiding the limitations described above involves the use of decomposed cross-sections in the core profile. Previous work has therefore dealt with several individual circular cross-sections [4, 5]. The connection of the cross-section components plays a decisive role here: Since the individual components do not lie in the axis of gravity of the overall cross-section, an interaction must be taken into account with regard to the individual moments of inertia.

In the project of Munich highlight business towers [6], the design of the bracing members required large steel sections for axial loads of up to 19 MN. The limitations of solid sections larger than 100 mm led to the design of laminated steel plates as core profiles in concrete-

filled hollow sections for composite columns. For this, steel plates were stacked and connected along their entire length with weld seams. Flame-cut steel plates were a cost-effective and readily available basis to flexibly design the core profile and enabled the construction of these members. In contrast, the extensive welding process caused high costs for manufacturing and quality control.

A strong growth in availability of weldable high-strength steels with further increasing yield strengths in recent years has allowed for substantial improvements of shortcomings implied for present steel construction (Figure 1-2). The dimensions of available rolled products and plated steel products have been increased through improved manufacturing processes. Plates with high strengths of over 960 MPa are now also produced in thicknesses of up to 40 mm. The load bearing capacity of concrete has also increased enormously with the development of UHPC, for example.

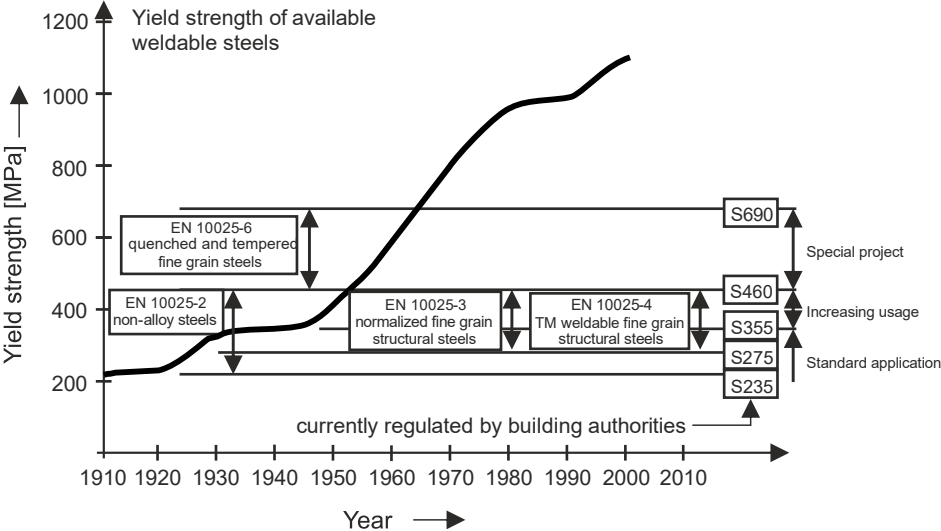


Figure 1-2 Development of yield strengths of high-strength constructional steels in 20th century acc. to [7].

Imperfections in steel profiles can result as geometric or structural imperfections and have great influence on the stability behavior of compressed members. They can originate from production, further processing, or tolerances during assembly. Geometric imperfections include camber, misalignment, or unplanned eccentricities of connecting members. Structural imperfections are usually characterized by stresses imprinted in the raw product during production or inhomogeneities in the material. These are particularly pronounced in large solid cross-sections, as the section cools down with a large internal temperature gradient. First investigations of high-strength steels imply lower ratios of residual stresses to yield strength leading to a beneficial behavior of members under compressive load (e.g. [8]).

The possibilities for using high-performance materials to increase load-bearing capacities of composite columns have been increasingly investigated in recent years. Until now, the steel strengths to be used for composite columns are limited to 460 MPa, according to the current standard prEN 1994-1-1:2024 [9] (EC 4-1-1). The load bearing capacity of columns can be increased by using high-strength materials, or the cross-section can be reduced while maintaining the same load bearing capacity. The use of high strength material increases the relative slenderness of the column compared to a comparable cross-section with the same dimensions. The term relative slenderness is to be understood as a measure of the square root of the ratio of plastic normal force resistance to critical buckling load. Consequently, the increase of strength is simultaneously reduced by an increased risk of buckling. Due to the increased risk of buckling, there is a simultaneous reduction in the increase in load-bearing capacity achieved via the strength. The load-increasing effect therefore plays a particularly important role for columns that are not or only slightly prone to buckling, with low slenderness.

In addition to the technical concept of relative slenderness, a colloquially slender column can meet the increasing demand of architecture to be able to design spaces more flexible. It is possible to realize smaller cross-section dimensions with the same load-bearing capacity or to reduce the number of columns required due to the increased load-bearing capacity. This is associated with a larger rentable floor area per floor. One aspect of the sustainable use of resources is the efficient use of the available strengths. The calculably necessary reductions due to large dimensions should be avoided. High-rise buildings in central Europe usually have an average floor height of 2.70 m to 4.00 m. Columns can be optimized with special attention to this length. For this floor height and considering average loads of 1.4 MN per floor¹, large diameters of over 356 mm are necessary for more than eight floors, using conventional composite columns. The application of high-strength column constructions appears advantageous beyond these construction heights. Particularly in large buildings with a repetitive floor plan, a high economic efficiency of the construction should be aimed for.

Even though the advantageous characteristics of composite columns, their limitations regarding bearing load and maximum available dimensions resulted in receding applications of this construction method. This has led to the development of a completely novel approach of composite columns, as part of a research project [10]. This state-of-the-art design consists of a high-strength steel tube (HSST) with a core profile of high-strength laminated steel plates (HSLP). The intermediate space is filled with concrete as confinement and fire protection layer. The individual plates should only be connected to each other to a limited extent to reduce the

¹ Design values for an assumed column pattern of 8x8 meters, 300 mm thick concrete slab, and 5 kN/m² live loads.

production costs depending on the required resistance. This design makes it possible to produce an economical column with a high load-bearing capacity.

The column design developed in the presented project features a combination of innovations that have not been investigated in previous research. Key parameters for a wholistic understanding of the load-bearing behavior are the material characteristics including geometric and structural imperfection, the shear interaction of the individual elements and thus the flexural resistance. To understand the bearing behavior and influence of each factor, material characteristics as well as detailed investigations were employed. In particular, the following questions arose and were studied:

1. What residual stresses can be detected in flame-cut high-strength steel plates as structural imperfections?
2. Does the targeted use of weld seams between the assembled laminated steel plates influence the flexural stiffness of the columns?
3. What load-bearing behavior do the innovative columns with HSLP in high-strength tubular section confined with normal-strength concrete exhibit if exposed to centric axial load?
4. What effect does the combination of high-strength steels (high strain capacity) with normal-strength concrete (low strain capacity) have on the design using strain-limited methods?
5. Can the new composite columns be designed using previous simplified design methods?

The following work is structured in four chapters. Chapter 2 gives an overview of current design standards and their historical background as well as an overview of present investigations on other innovative composite columns motivating this research. Chapter 3 presents large- and small-scale experimental tests of fabricated columns and their key findings as well as a discussion of the results and used methods. In Chapter 4 the implementation of nonlinear finite element model, its verification and validation process, and results including detailed investigations is presented. Based on the results, a design proposal is presented and discussed. The overall findings are concluded in Chapter 5, which also includes an outlook on future research possibilities.

2 Review of the literature

2.1 Buckling of steel and steel-concrete composite members

Buckling as stability failure is one of the predominant problems of components subjected to compression and especially addressed in steel construction. Slender design can lead to a loss of stability, analytically described as when the determinant of the stiffness matrix equals zero. Buckling failure is particularly problematic due to a sudden collapse without prior notice. The analytical solution to the buckling problem was already derived by Leonhard Euler in 1744 for elastic and perfectly straight members on the basis of which the relationship between buckling resistance N_{cr} and flexural stiffness EI can be derived [11].

$$N_{cr} = \frac{\pi^2 \cdot EI}{l_{cr}^2} \quad (2-1)$$

l_{cr} Critical buckling length

An extension of Euler's elastic buckling theory was independently described by Engesser in 1889 [12] and Tetmajer in 1903 [13], among others. It was recognized that in areas of low slenderness, the material strength has a decisive influence on the load-bearing behavior and the ideal critical buckling load could not be reached. This is referred to as plastic buckling. Based on empirically verified findings, Tetmajer defined material-specific slenderness limits below which a normal force failure becomes decisive as a stress problem. This range was described using a linear equation. Plastic buckling failure, as a state between elastic buckling and plastic normal force failure, was described clearly by Tetmajer. Materials with a yield point exhibit a constant stiffness (modulus of elasticity) under load until the yield point is reached. After the yield point is reached, the stiffness no longer corresponds to the constant initial value; it follows a tangent on the stress-strain relationship. The cross-section is assumed to have a plane strain distribution. The stresses of the stress-strain relationship resulting from the deformation are in equilibrium in their integral (Figure 2-1). As a result, areas that are already in the plastic range of the stress-strain relationship experience greater strain to compensate the stress of elastic regions. Due to the local loss of stiffness caused by the tangent modulus, there is a shift in the effective cross-section, so that additional drifting effects promote failure according to second-order analysis. [14]

The consequence of these relationships is a locally reduced flexural stiffness in areas of the greatest curvature, in the case of imperfect bars subjected to normal force at mid length of the member as well as a shift of the center of gravity.

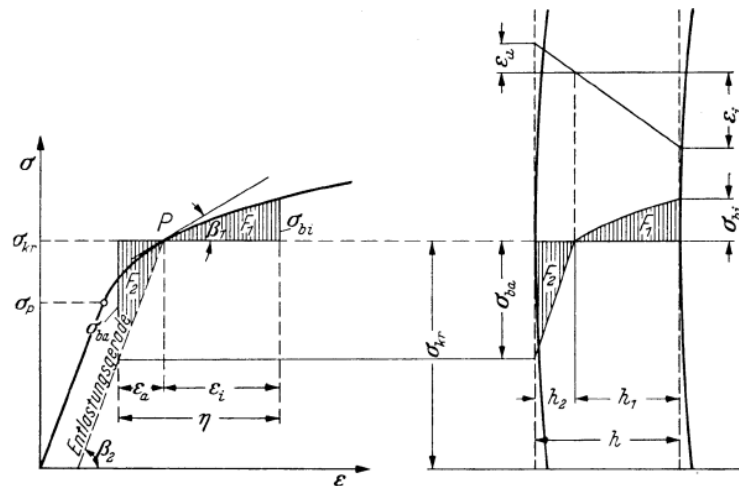


Figure 2-1 Stiffness reduction induced by local yielding during buckling failure acc. to [11].

Imperfections of members under compression can lead to a prior failure. Separated in geometric and structural imperfections, the origins are numerous. Geometric imperfections mostly occur from the manufacturing process where tolerances occur regarding straightness. Structural imperfections in contrast mostly consist of residual stresses as a result of uneven cooling processes. The imprinted stresses lead to premature failure of local sections. The extent can vary depending on the geometry and manufacturing process and therefore must be accounted for in the design.

Imperfections and the use of different material strengths required a standardized design for engineering applications. The introduction of the Eurocodes further necessitated a standardized design basis. To this end, Beer and Schulz [15] used a large collection of empirical data of buckling tests for the development of buckling curves in 1969, depending on material strength and profile geometry. They should enable the design of pin ended buckling members under pure compressive loading. The background to these buckling curves is shown in [16] or [17]. The buckling curves were officially described by the European Convention for Constructional Steelwork (ECCS) in 1976 [18]. In 1978, Maquoi and Rondal developed an analytical description of these lines based on the Ayrton-Perry equation [19] and still serve until today as a basis for the design of centrally compressed members according to prEN 1993-1-1:2020-08 [2].

These buckling curves are based on the analytical solution of the buckling problem of a pin ended column with a sinusoidal bow imperfection e_{0d} . The solution of this equation results in the following form of the Ayrton-Perry equation (Equation (2-2)) with further documentation in [20]. The reduction factor χ and normal force resistance N_r as well as flexural capacity M_r are respected.

$$(1 - \chi)(1 - \chi \cdot \bar{\lambda}^2) = e_{0d} \cdot \frac{N_r}{M_r} = \eta\chi \quad (2-2)$$

The newly introduced factor η is intended to consider for imperfections in the form of residual stresses, geometric bow imperfection and eccentric load. To additionally consider the influence of the column length, the factor was set to $\eta = \alpha(\bar{\lambda} - 0,2)$ with α as the correction value of the respective buckling line, resulting in Equation (2-3).

$$(1 - \chi)(1 - \chi \cdot \bar{\lambda}^2) = \alpha(\bar{\lambda} - 0,2) \cdot \chi \quad (2-3)$$

It is visible that the cross-section-dependent variables N_r/M_r or A/W_{el} are not regarded in this approach. The correction values of the buckling curves were determined in historical tests of low steel grades.

The influence of the yield strength of the beam is considered in the relative slenderness $\bar{\lambda}$ described by the plastic normal load capacity $N_{pl,Rd}$ and the critical buckling load N_{cr} (Equation (2-4)).

$$\bar{\lambda} = \sqrt{\frac{N_{pl,Rk}}{N_{cr}}} \quad (2-4)$$

The design buckling resistance for members subjected to centric compression $N_{b,Rd}$ is therefore calculated with the plastic normal force capacity $N_{pl,Rd}$ and the reduction factor χ from the respective buckling curve.

$$N_{b,Rd} = \chi \cdot N_{pl,Rd} \quad (2-5)$$

It is noticeable that the use of high-strength steel grades leads to opposing effects: The numerator of Equation (2-4) increases in the relative slenderness term while the denominator remains the same. This leads to a higher relative slenderness and therefore an increased risk of buckling failure, whereas the plastic resistance is enhanced further. To conclude, it seems more beneficial to use high-strength steel in ranges of lower relative slenderness. The applicability of previous imperfection approaches and assignment of suitable buckling curves is the subject of current research (e.g. [21]).

Based on the analytical relationships of the buckling member, Southwell [22] developed a graphical non-destructive method for evaluating experimental buckling tests in 1932. This

approach takes into account a centrally compressed bar with a bow imperfection. The theoretical derivation of this evaluation is based on a sequence of the effects of various imperfections. According to Southwell, the geometric imperfection dominates the load-bearing behavior with increasing load, which corresponds to the first mode shape of a pin ended member under compression. In graphical terms, this manifests as a straight line between the horizontal deflection in the middle of the bar on the abscissa and the ratio of the acting force to the deflection on the ordinate. The critical elastic buckling load can be read from the linear gradient, while the intercept represents the chord of the initial bow imperfection. The so-called Southwell plot can also be applied to other problems: in 1934, Fisher [23] demonstrated its validity for eccentrically loaded pin ended members that can be described as compressive members under centric loading with uniform transverse loads. His demonstration was based on using the example of wind-loaded airplane wings. The extension the applicability of the Southwell plot from elastic buckling to the area of plastic buckling was also shown by Singer in 1989 [24]. Cross-sections with variable geometries have been validated by Marcinowski, Sadowski et al. in 2022 [25]. The relationships of stability failure described by Southwell can also be used in the evaluation of bars prone to lateral-torsional buckling, e.g. [26]. This method thus represents a versatile non-destructive determination of a critical buckling load of a compressed member.

2.2 Current research and design of composite columns

Composite columns represent a consequent development of fire safe iron columns first developed by Peter Wight in 1857 and additionally offer high load bearing capacities with flexible section design. They are versatile structural members and can be adopted freely, especially as concrete-filled steel tube (CFST). The architectural possibilities offered by combinations of different profiles result in a wide range of design options. Innovative composite column cross-sections and their architectural requirements are summarized in excerpts in Empelmann, Oettel et al. [27]. Design methods provided by the current standard prEN 1994-1-1:2024 [9] entail limited applicability. Due to the highly individual composition of different material strengths, different strain capacities and geometries, composite columns have been a central part of steel research for years.

Current design methods

In the standard EC 4-1-1 [9], composite columns are defined as a composition of steel profiles and concrete. The steel profiles can be either concrete encased rolled profiles or concrete-

filled steel tubes, or a combination of the two. Further, the proportion of the steel profile δ_c may account for between 20 and 90 % of the normal load-bearing capacity, otherwise they are referred to as concrete or steel columns, respectively. The load-bearing behavior of composite columns is primarily defined by the interaction of the cross-sectional parts. In the case of an acting bending load, the concrete cross-section fails in parts of the cross-section subjected to tensile stress, which is compensated for by the steel profile. In the compressed area, both the steel and concrete cross-sections transfer the load in accordance with their stiffness. The design of composite columns can be done using the simplified design method, following EC 4-1-1 [9]. This method is only applicable to doubly symmetrical members with a relative slenderness $\bar{\lambda} \leq 2.0$ and cannot be used with two or more unconnected sections.

In this design method, columns subjected to axial load and bending can be calculated using a fully plastic cross-sectional interaction curve. This is derived for individual combinations of compression and bending. To consider strain limitation of the concrete and steel components at maximum load, a reduction in the respective plastic moment resistance is required. These are specified with constant values for steel grades S235 and S355 as 0.8 and for S460 as 0.9.

This design method is further simplified for members under pure axial compression analogous to the previously described buckling curves for steel profiles according to EC 3-1-1 [2]. This design is applicable for defined cross-sections with assigned buckling curves. Due to the selected cross-section shape, the influence of structural imperfections in the steel sections is considered in this form of design. The effective flexural stiffness $(EI)_{eff}$, necessary for the determination of the critical buckling load N_{cr} is calculated following Equation (2-5). This term of the effective flexural stiffness dates back to investigations of Roik et al. [28, 29] where the factor for the concrete section was calibrated from experimental results and did not follow a statistical safety analysis, according to Bergmann [30]. Further research for the use of the buckling curves as design method and assignment of the buckling curves date back to work mainly driven by Bergmann, Lindner and others from the 1980s and 1990s [31–35]. Alternative approaches to calculate the flexural stiffness of composite columns in different standards are concisely described in [36].

$$(EI)_{eff} = E_a \cdot I_a + E_s \cdot I_s + 0.6 \cdot E_{cm} \cdot I_c \quad (2-6)$$

$E_a \cdot I_a$	Flexural stiffness of the structural steel section
$E_s \cdot I_s$	Flexural stiffness of the reinforcement steel section
$E_{cm} \cdot I_c$	Flexural stiffness of the concrete section

For composite columns that are not covered by the tabulated buckling curves, the general method can be used for design. Considering the vast progress of finite-element methods in constructional engineering, this method provides a concept for non-linear analysis including effects from residual stresses from prEN 1993-1-14:2023 [37] and geometrical imperfections. The geometrical imperfections are defined as a function of δ_c reaching from $L/250$ to $L/1000$, the latter used as a common value used for steel members (e.g. [18] and more). The material behavior of steel and concrete must be addressed non-linear. The design value of the column resistance is then determined by applying safety factors on the mean value of resistance that consider scattering of material properties. Experimental tests can be used to benchmark the numerical model and reduce the safety factor of modeling uncertainty. An overall safety factor for the material property covers uncertainties of material properties, resistances, geometric scattering and further geometric properties.

The two design methods have individual advantages and disadvantages: the simplified method allows a fast design of columns using buckling curves but is very much restricted to loading and the column's section. The general method requires advanced knowledge about the residual stresses of the used steel profiles and sophisticated finite element software including an experienced user but allows the design of various sections.

Experimental buckling tests on innovative composite columns

The buckling behavior of composite columns depends on numerous parameters such as the cross-section geometry, materials used and load condition. Due to the increased use of high-strength steels, the transferability of previous findings on the load-bearing behavior of composite columns needs to be clarified. The first experimental results on the use of high-strength steels were obtained by Lippes [38] with concrete-filled hollow sections and a round solid core of steel grade S460. Neuenschwander et al. [39] and Kleibömer [40] carried out supplementary investigations of analog column cross-sections. Buckling tests on the mentioned sections including high-strength steels of up to 960 MPa were substance of Nonn,

Feldmann et al. [41]. As a further development of the column cross-sections, Chanou [4] and Mensinger, Röß et al. [6] used individual core sections consisting of several full-round sections of steel grades S355, and S670, respectively.

Alternative cross-section shapes as so-called double hollow section composite columns with concrete filling were investigated by Liew and Xiong [42], [43], and Romero et al. [44], among others, using high-strength concretes and normal-strength steels. In addition, these cross-sections were tested by Schurgacz, Knobloch et al. [45] and investigated numerically by Espinos et al. [46] with high-strength steel grades up to S700 or S960, respectively.

Buckling tests by Lai, Liew et al. [47] were carried out on fully encased steel profiles of steel grade S690 and concrete of grade C90 with an eccentric load application of 30 and 60 mm. The test results indicated a significant deviation from the effective flexural stiffness of the column cross-sections as determined by prEN 1994-1-1:2024 [9]. An extensive summary of investigations and evaluation of the static performance of high-strength composite columns was presented by Lai et al. [48].

Experimental four-point bending tests

As pointed out, the flexural stiffness serves as a key parameter for the resistance of composite columns. Bending tests offer the possibility to experimentally determine the isolated interaction of composed members with or without axial load. However, only a little number of investigations on composite columns under pure bending are known to date.

Theoretical studies to develop analytical interaction relationships of slender columns under biaxial bending loading have been carried out by Bonet, Romero et al. [49]. Experimental bending tests on composite columns were carried out by Han [50] and Han, Lu et al. [51]. The columns consisted of concrete-filled steel tubes with fiber-reinforced concrete. Further bending tests were carried out by Lai and Liew [52] on cast-in-place steel sections with high-strength concrete and Tretyakov et al. [53] on hollow section composite columns with fiber-reinforced concrete. Both also tested under pure bending without normal force loading. Huang, Uy et al. [54] investigated concrete-filled steel tubes made of high-strength steels under combined axial and bending load.

In the presented literature, no research could be found addressing the innovative section design consisting of HSLP as core section in a combination with high-strength steel components such as tubular sections.

2.3 Research on residual stresses in steel plates

Structural imperfections are a critical factor in components subjected to compressive stress: compressive residual stresses in the load direction can cause the yield point to be reached early under load, as stresses are already imprinted. The yielding of individual steel fibers can cause these cross-sectional parts to fail and reduce the effective cross-section. The change in the effective cross-section results in a shift in the center of gravity of the cross-section and, as a result of the additional increase in deformation, finally an early buckling failure. The ideal buckling load can therefore not be achieved, and the component fails prematurely. This effect is taken into account in the buckling curves according to prEN 1993-1-1:2020-08 [2], depending on the shape of the steel profile.

The laminated steel plates of this research project are applied in the longitudinal axis of the plates, i.e. in the rolling direction, residual stresses in this direction are of interest. The following considerations relate exclusively to these stresses.

There are a number of factors that lead to the formation of residual stresses. One source is in the manufacturing process. During cold forming, external influences such as rolling or stretching impose forced deformations on the unheated steel. Since the rolling process usually cannot form a component entirely, i.e. over the entire thickness of the component, changes in shape and thus strains occur near the surface. These are compensated for by internal equilibrium in the center of the part. The resulting stresses are a function of component thickness, rolling pressure and material strength. Post-treatments such as shot peening also correspond to such cold forming.

In hot forming, this forced deformation of the component takes place at an elevated temperature. The influence of the subsequent cooling process is crucial. Due to the temperature-dependent material behavior of the steel, the superficially cooled areas gain strength while the inner areas have not yet cooled. As a result of the temperature gradient and the increasing cooling of the inner areas, a stress occurs in which the core contracts but is prevented from doing so by the already solidified outer areas. This results in compressive residual stresses near the surface and tensile residual stresses in the interior of the part.

The cooling process during manufacturing and its influences on the residual stress distributions were already investigated in 1968 by Alpsten [55], whereby a uniformly heated steel plate with a yield strength of 30 ksi (\approx 207 MPa), a thickness of 89 mm, and a width of 61 mm was cooled in the course of a simulation. From the temperature distributions, the material properties of the respective temperature state were taken into account stepwise using a subroutine and

so simulating the development of internal stresses. This simulation was repeated for different plate thicknesses. The result of such a simulation is shown in Figure 2-2, where it can be seen that the residual compressive stresses have elliptical distributions in the edge areas and represent a linear distribution across the cross-section in the area of the axis of symmetry.

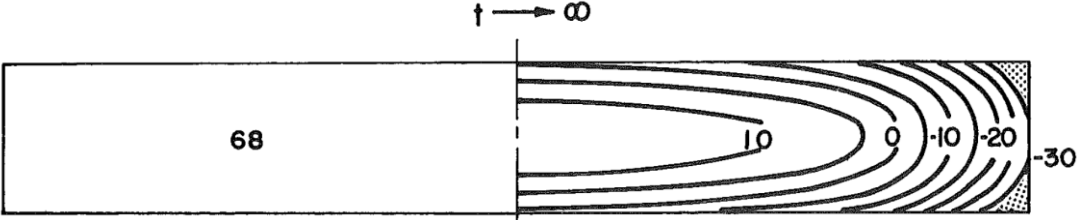


Figure 2-2 Simulation results of fully cooled steel plate (values in ksi) from [55].

Alpsten observed an influence of the plate’s width on the level of residual stresses. Higher residual compressive stresses were observed at the outer edges and, as a result, higher residual tensile stresses in the core of the plates. The propagation of the compressive stress zones in the direction of the core was also observed with increasing plate thickness. The widths of the tested plates were 150, 305, 500 and 610 mm with thicknesses of 12.7, 51, 89, and 102 mm. When the width-to-thickness ratio of the steel plates was standardized, an almost constant tensile residual stress was observed in the core of the plates. At the edges, however, the compressive stress increased with the plate thickness and width. The stresses reached the yield point of the material in the thickest plates. The tests showed that most of the residual stresses only developed at lower temperatures, which is presumably due to the reduced strength at higher temperatures.

The effects of different cooling rates on the formation of residual stresses were determined by Lippes [38] for round steels of steel grades S235 to S460 by means of numerical investigations. Due to the lack of experimental investigations, it is unclear whether these findings can be extrapolated to accelerated cooled, high-strength steel grades (> S460).

Another source of residual stresses can result from the cutting of steel components. Flame cutting causes localized heating above the melting point of the material. The gradient of the local heat input quickly dissipates in the middle of the material and causes high tensile stresses at the cut edges up to the yield point of the base material. For reasons of equilibrium, residual compressive stresses occur in the center of the material.

The research work of Kishima, Alpsten et al. [56] dealt with steel plates of different thicknesses of strength class A572(50) ($f_y = 345$ MPa). Young and Dwight [57] also examined steel plates with thicknesses of 6.3 and 12.1 mm and yield strengths of 160, 240, and 480 MPa. Of

particular interest were the residual stresses in the flame cuts and welds of the flame-cut plates. The investigations showed an analogous behavior of the flame cut and weld effects with a range of high residual tensile stresses at the outer edges reaching up to the yield point of the material. The finding was consistent with different material strengths tested.

Plate thickness was found to have a significant influence on the width of the tensile zone along the flame-cut edge. The explanation given was that the larger cut surface allowed more heat to penetrate the plate. Roa and Tall [58] defined a sheet thickness of 5 mm as the lower limit at which there is no distribution of residual stresses across the sheet thickness. Investigations by Odar et al. [59] were carried out on high-strength quenched and tempered steel plates (type "T-1") with yield strengths of 765 MPa of various widths in welded and unworked form using the sectioning method. It was found that the residual stresses due to the flame cutting and welding processes showed a uniform distribution. Decreasing compressive stresses were found in the central area with increasing plate width. No clear dependence of the measured compressive values could be derived from the plate thickness. With respect to the measured values, a higher scatter was observed for less wide plate cross-sections, which decreased with increasing plate width, see Figure 2-3. A slight increase in the residual tensile stresses at the edge was observed for the specimens welded symmetrically on both sides; otherwise, there was little difference from the flame-cut plates.

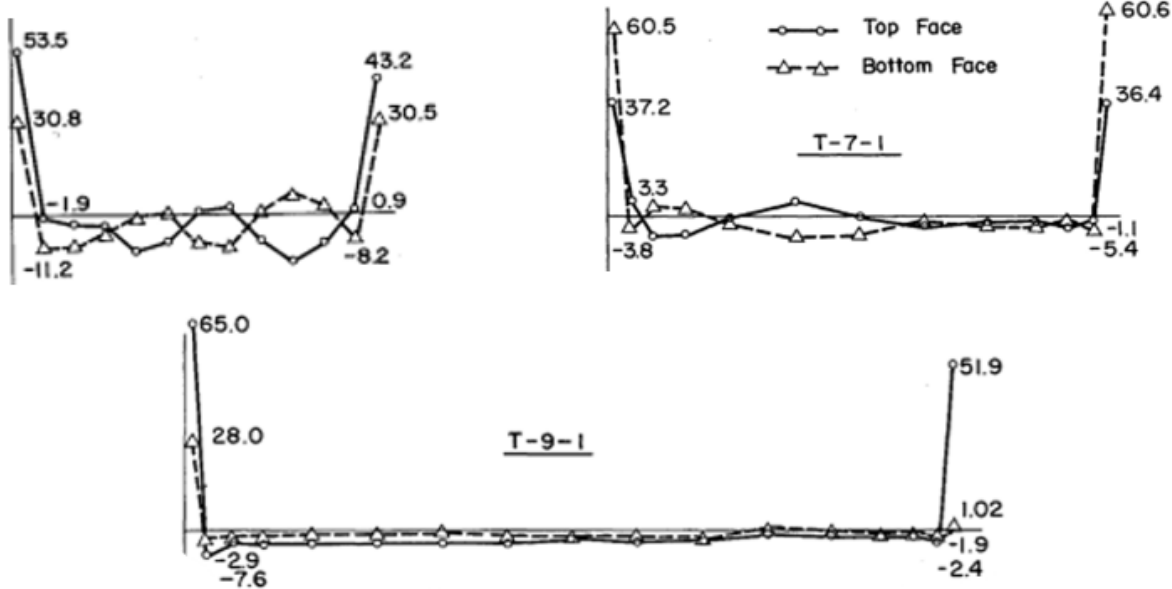


Figure 2-3 Residual stress distribution of steel plates with 305, 406 and 610 mm width, thickness each 12.7, 12.7, and 25.4 mm, respectively (values in ksi) from [60].

Due to the limited plate thicknesses in previous investigations, Thiébaud [61] investigated flame-cut 60 mm thick, 600 mm wide steel plates of grade S355 using the sectioning method. The investigations confirmed pronounced tensile zones at the cut edges and low compressive residual stresses in the central areas. These observations were in good agreement with previous findings on the influence of flame cutting on steel plates.

An analytical approach based on the historical investigations was published by ECCS [18] to determine the spatial distribution of residual stresses in single and double-sided flame-cut plates. The determining parameters are the thickness t , the yield point of the material and the plate width b . A simplified distribution in the form of constant stress blocks is assumed for the stress distribution (Figure 2-4). At the flame-cut edges, the tensile stress σ_r is presumed to be the level of the yield strength of the base material. By integrating the stress blocks, the level of the mean residual compressive stress σ_c , decisive for premature yielding under compressive load can be determined:

$$\sigma_c = \sigma_r \frac{2c}{(b - 2c)} \tag{2-7}$$

- σ_r Tensile residual stresses at the flame-cut edge, corresponds to $R_{p,02}$
- c Width of the tensile zone
- b Width of the zone with compressive residual stresses

The width of the stress block of tensile residual stresses c depends on the yield stress and plate thickness t .

$$c = \frac{1100 \sqrt{t}}{\sigma_r} \quad (2-8)$$

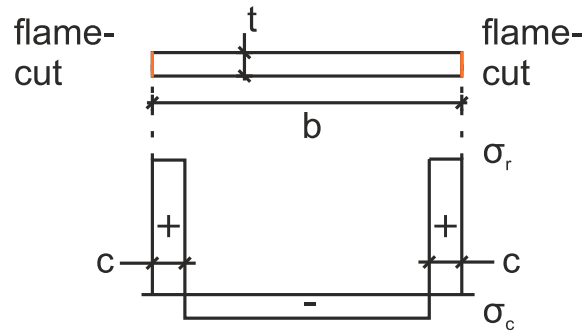


Figure 2-4 Residual stresses of two-sided flame-cut plates from [18].

Therefore, the dominant influences on the residual stresses of flame-cut plates can be concluded as the yield strength of the material, the plate thickness, and the plate width. Steel plates with yield strengths above 700 MPa have not been considered in previous experimental investigations.

Since residual stresses are caused and influenced by all thermal processes, post-treatments such as welding also have an effect on the steel. There is a consistent finding in the literature that high compressive residual stresses are localized in the vicinity of the weld. As the distance from the weld increases, these compressive stresses decrease rapidly. Schaupp et al. [62] investigated the formation of residual stresses as a result of so-called dummy welds with different energy input on high-strength quenched and tempered steels of grade S960 QL and thermomechanically rolled steels of grade S960 TM. A behavior analogous to previous findings on low-strength steels was observed, with increased tensile residual stresses in the heat-affected zone and decreasing stresses away from the weld. The residual stresses reached values of 250 to 300 MPa. For the quenched and tempered structural steel, the level of residual stresses was found to be independent of the selected energy input, whereas the thermomechanically rolled steel developed greater residual stresses in the weld at higher energy inputs.

3 Experimental investigations

A completely new section design was developed and manufactured to tackle the limitations of by current solutions for composite columns such as high residual stresses and limited size of the deployed solid core profiles in CFST. The section consists of laminated steel plates that are deployed as core section into a tubular hollow section and subsequently confined with filling concrete. Substantial gains of load bearing capacity were pursued using high-strength steel plates of steel grade S960QL as well as high-strength steel tubes of steel grade S890QL. In comparison only little load bearing was expected from the concrete section, so a filling concrete of concrete class C30/37 was used to confine the voids between core profile and tube. The filling degree of the HSLP section was maximized by approximating a circular cross-section and concurrently to ensure a minimum concrete cover of 25 mm (Figure 3-1). Steel plates of 40 mm thickness, chamfered at the edges, and graduated 20 mm steel plates were used as sections. The diameter of the tube was chosen as 244.5 mm with a wall thickness of 12.5 mm for all specimens. A further innovation was employed in the core section, where the amount of shear connection was limited to local connections between the plates, using bolts or fillet and butt welds. This approach should limit the construction effort to the minimum that would be needed by the design of the column.

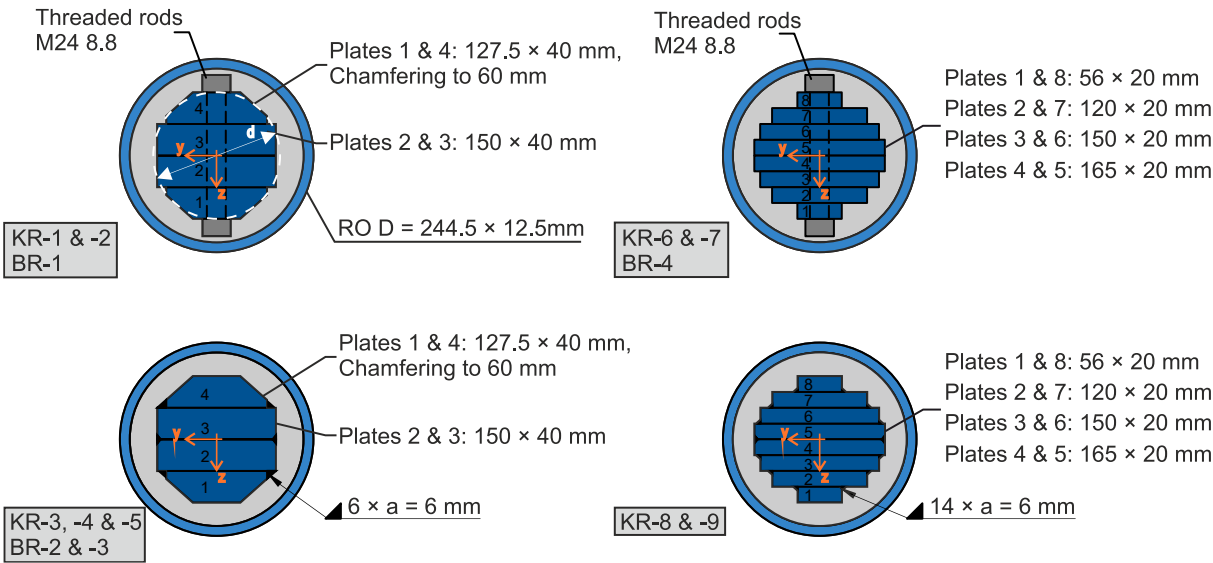


Figure 3-1 Sections of specimens for large scale tests [63].

Thirteen of these innovative columns were constructed for a large experimental testing series, as this type of column has not been tested before. The construction procedure started with the fuel-cutting of steel plates and subsequently stacking (Figure 3-2). The core sections were connected by bolts, (M24 8.8) that were prestressed with a torque lever to a preload of 190 kN

or alternatively fillet and butt welds at a preheating temperature of 100°C ($a_w = 6$ mm, wire electrode G 89 4 M21). Prestressing as well as welding processes were executed in a directed procedure from the middle part of the plates towards the ends to evade possible constraining effects. The HSLP was then equipped with fiber-concrete spacer evenly distributed around the circumference and along the length of the section. Subsequently, the plate stack was inserted into the tubular hollow section using a crane. Geometric variations needed to be considered with a small gap between tube and spacers as mounting tolerances. The columns were equipped with end plates and confined with filling concrete in an upright position.

Overall it could be concluded from the manufacturing process that a sufficient space between the spacers and cladding tube needs to be regarded to ensure a unproblematic assembly. Also, due to the high-strength characteristic of the steel plates caused decelerated process of fire-cutting and drilling. In consequence, many cutting errors and an increased wear of drill heads was observed. Fixed positions of the bolts implied further constraints for the assembly.

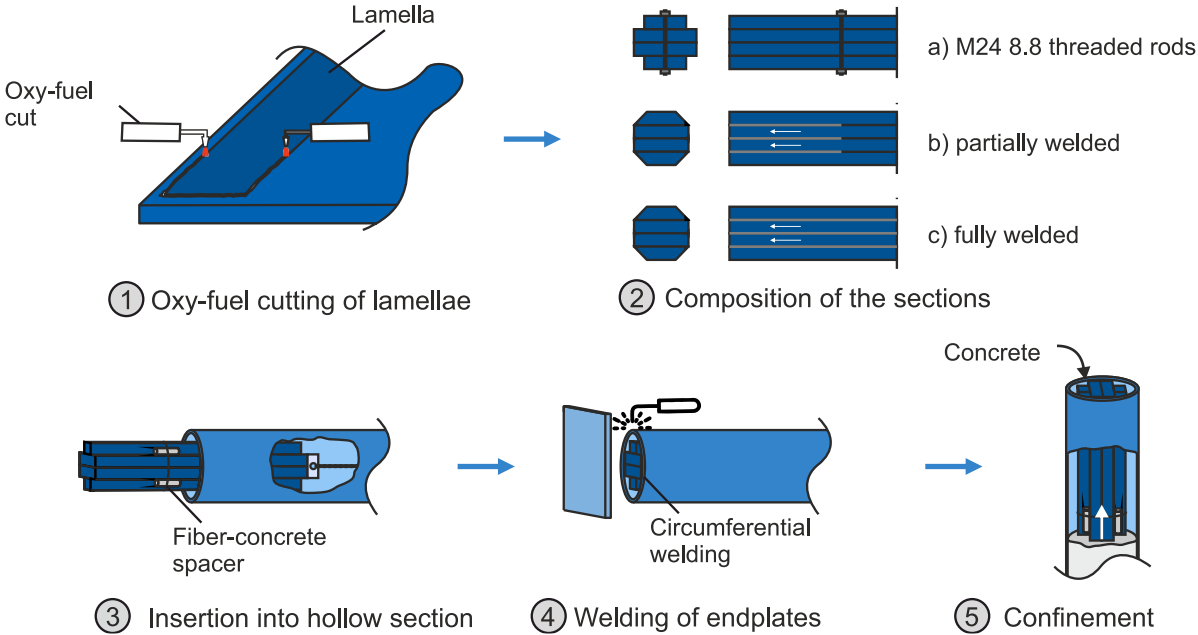


Figure 3-2 Schematic display of the construction process [63].

3.1 HSLP composite columns under compression and uniaxial bending

The load bearing capacity of composite columns is defined by various parameters: geometrical and structural imperfections, material strengths, load eccentricities, and many more. A realistic confirmation of the interaction of these influences can only be enabled by experimental buckling tests. In this investigation, the buckling behavior under uniaxial bending and compression was investigated.

Methods

Nine full-scale buckling tests were performed on one-story columns (Table 3-1). Hot-formed hollow sections with constant diameter and wall thickness were used. A maximum concrete cover of 25 mm was used to achieve a high degree of filling. The core sections can be divided into 40 mm and 20 mm plate thicknesses, with the 40 mm plates chamfered at the corners. In order to investigate the effect of slenderness, two analogous cross-sections were constructed with typical floor heights of 2.60 m and 3.90 m, respectively. The aim of the experimental tests was to investigate the influence of a limited, local connection between the laminated steel plates. The plates of test specimens KR-3 and 4 as well as KR-8 and 9 were designed with a weld length of 20 % of the total length, situated at both ends of the column. Welding high-strength fine-grain structural steels is considered complex and error-prone, so the core sections of KR-1 and 2 and KR-6 and 7 were bolted with threaded rods (M24 grade 8.8). As a control specimen, KR-5 was designed with a core profile containing welds along the entire length of the specimen.

Table 3-1 Experimental test program of the buckling tests.

No.	No. of core plates [-]	Thickness of HSLP [mm]	Width of HSLP [mm]	Shear connection	Length [mm]	Tube diameter [mm]	Tube wall thickness [mm]	$R_{p0.2 \text{ tube}}$	Concrete
KR-1	4	40		4 × M24 8.8	2600	244.5	12.5	890	C30/37
KR-2	4	40		5 × M24 8.8	3900	244.5	12.5	890	C30/37
KR-3	4	40	2×60/150 (chamfered)	$l_w = 0.2 l$	2600	244.5	12.5	890	C30/37
KR-4	4	40	2×150 mm	$l_w = 0.2 l$	3900	244.5	12.5	890	C30/37
KR-5	4	40		$l_w = 1.0 l$	2600	244.5	12.5	890	C30/37
KR-6	8	20		4 × M24 8.8	2600	244.5	12.5	890	C30/37
KR-7	8	20	2×56 mm	5 × M24 8.8	3900	244.5	12.5	890	C30/37
KR-8	8	20	2×120 mm	$l_w = 0.2 l$	2600	244.5	12.5	890	C30/37
KR-9	8	20	2×150 mm 2×165 mm	$l_w = 0.2 l$	3900	244.5	12.5	890	C30/37

The tests were carried out at the KIBKON Test Institute for Structural Engineering at the Ruhr University Bochum. The testing machine had a maximum test specimen height of 10 m and a maximum test load (compression and tension) of 20 MN. Design details of the testing machine have already been described in various reports, e.g. [45]. The test setup (Figure 3-3) was equipped with two almost frictionless spherical plain bearings that transferred the load to the test specimens. The pivot point of the bearings was located on the surface of the spherical mold. An adapter plate ($t = 100$ mm) enabled the end plates of the columns to be bolted to the test setup. Due to the adapter plates and the end plates, the effective buckling length increased by a total of 280 mm, 140 mm in each direction. The load was applied eccentrically to avoid sudden buckling failure and to protect the test equipment and hall personnel from damage. Furthermore, the direction of buckling was clearly defined, with the spherical plain bearing allowing free deflection in all directions. The uniaxial bending moment acted along the y-axis, leading to an isolated bending in the direction of the individual shear connection of the plates.

The test specimens were fitted with strain gauges (Tokyo Measuring Lab., type FLAB-3-11-5LJCT-F and QFLAB-3-11-6FA5LT-F as high-temperature sensors in the welded cross-sections) at three levels in the longitudinal direction during production. Before the tests, the strain gauges were added to the outer hollow section at the height of the measuring levels, indicated as strain gauge 1 - 4 (abbreviated SG) in Figure 3-3. An optical measuring system from GOM was used to monitor the deformation during the test. Reflection points on the test body were photographed at a fixed frequency and then analyzed using digital image correlation. The inclinations of the bearings were also recorded.

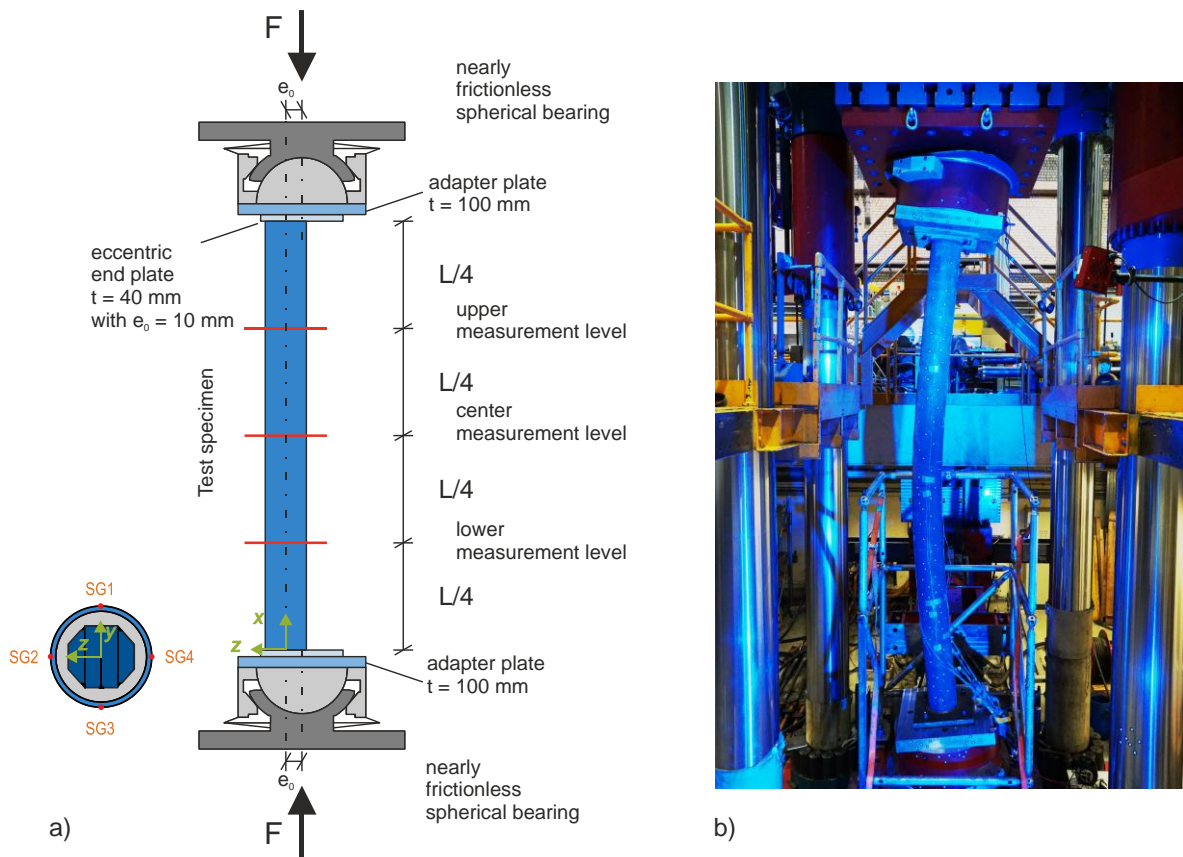


Figure 3-3 Experimental setup a) and failed test specimen in testing facility b) [63].

According to current standardization [9], there is no clear regulation for the experimental testing of composite columns. Annex B gives a recommendation for carrying out tests for composite beams, which has already served as a template for carrying out tests in some research projects [4, 5, 38, 45]. As adaptation of this testing procedure the parts of sequence A to C were first carried out under "preload" in all tests and then the load was increased in sections D and E as part of the "ultimate load test" until the test specimen failed (Figure 3-4).

After exceeding the maximum load, a spherical inclination of 8° was used as the limit criterion for the tests to avoid damage to the test facility. Each test was then completed. Following the test, all columns were removed and examined more closely.

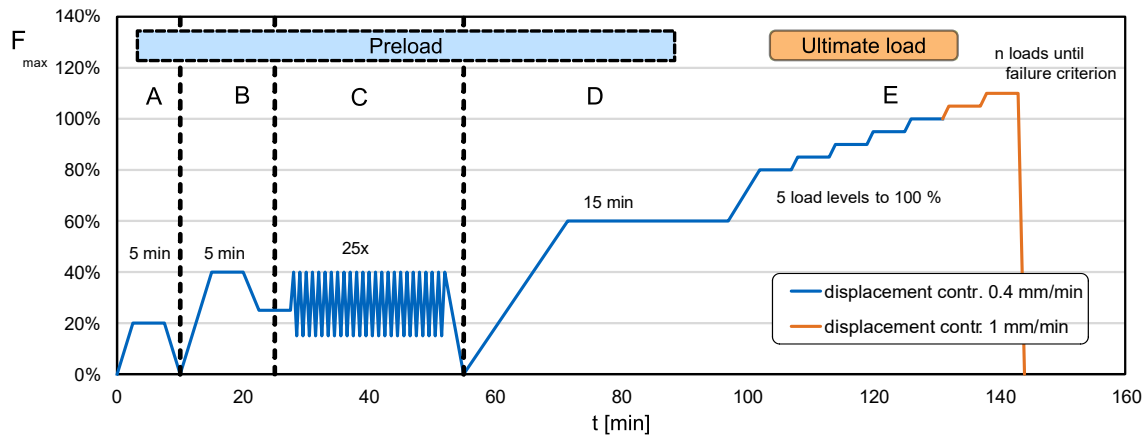


Figure 3-4 Experimental procedure acc. to prEN 1994-1-1:2024 Annex B.

The flexural stiffness $(EI)_y$ of a member under bending assuming Bernoulli's assumption of plane sections remaining plane can be derived using the beam equation thus following the relation of acting bending moment $M_E(z)$ and curvature κ of the section, see Equation (3-1).

$$(EI)_y = \frac{M_E(z)}{\kappa} \quad (3-1)$$

The curvature of the cross-section could be determined from recordings of the strain gauges on the cladding tube of the test specimens. The curvature κ from Equation (3-2) was formed from the difference between two opposing strain measurements ε_2 and ε_4 (see Figure 3-3).

$$\kappa = \frac{\varepsilon_4 - \varepsilon_2}{D} \quad (3-2)$$

With D : Diameter of the hollow section

The acting moment (3-3) could be calculated according to second-order analysis from the acting normal force N_E , the initial eccentricity of the testing facility e_0 , the deformation in buckling direction u_z , and the global bow imperfection w_0 :

$$M_E(z) = N_E \cdot [e_0 + u_z + w_0] \quad (3-3)$$

A coordinate system that describes the deformations and structural details was defined for all subsequent descriptions. This will be used in the following (Figure 3-5).

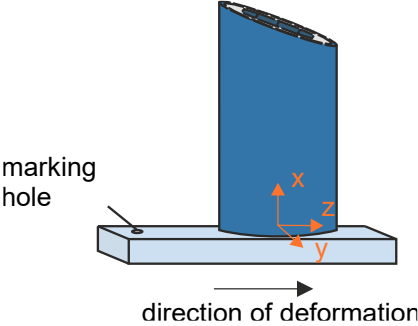


Figure 3-5 Definition of axes of the test specimens in buckling tests.

Results

In all tests, the test specimens were loaded up to their maximum load capacity and ended at the defined test target of a maximum bearing rotation of 8°. Each test specimen deflected in the defined z-direction (Figure 3-6) uniformly, without large differences in the group of short and long columns. A nearly linear elastic deformation was seen for shorter columns, with longer columns of a more pronounced horizontal deformation at lower axial load. Only minor deformations were observed perpendicular to the buckling direction (Figure 3-7). The maximum loads of the tests are shown in Table 3-2. The failure of the test specimens proved to be extremely ductile; there was no spalling or cracking in the cladding tube. In some test specimens, a bulge formed in the cladding tube on the side subjected to compressive stress, but only in the supercritical range after the ultimate load was reached. The bearing loads can be grouped according to the length of the test specimens, with the columns with a length of 2.60 m achieving bearing loads between 14,605 kN (KR-8) and 13,545 kN (KR-6). The columns with a length of 3.90 m achieved loads of up to 9,372 kN (KR-4) and 8,930 kN (KR-7). The horizontal deformations on reaching the load capacity were 26.5 mm (KR-6) and 55.2 mm (KR-4). Detailed recordings of the experimental tests are displayed in the Annex, Figure 6-1 to Figure 6-9.

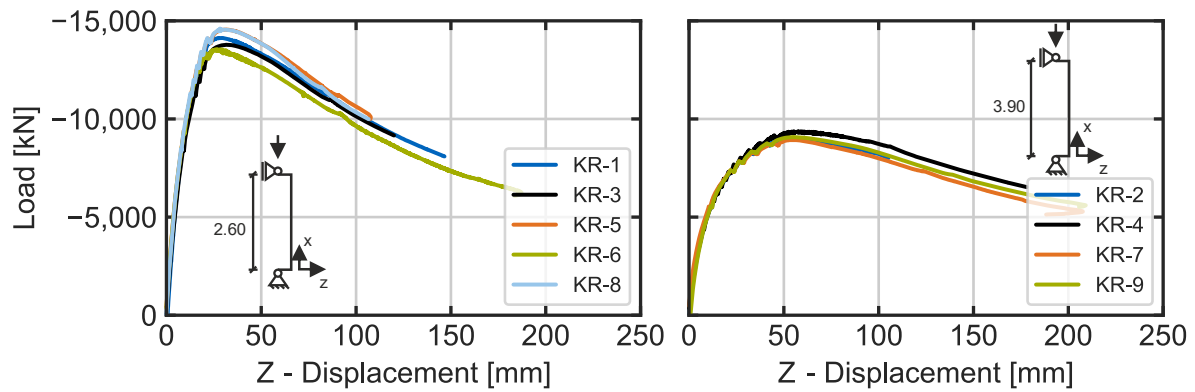


Figure 3-6 Displacement in buckling direction of the buckling tests [63].

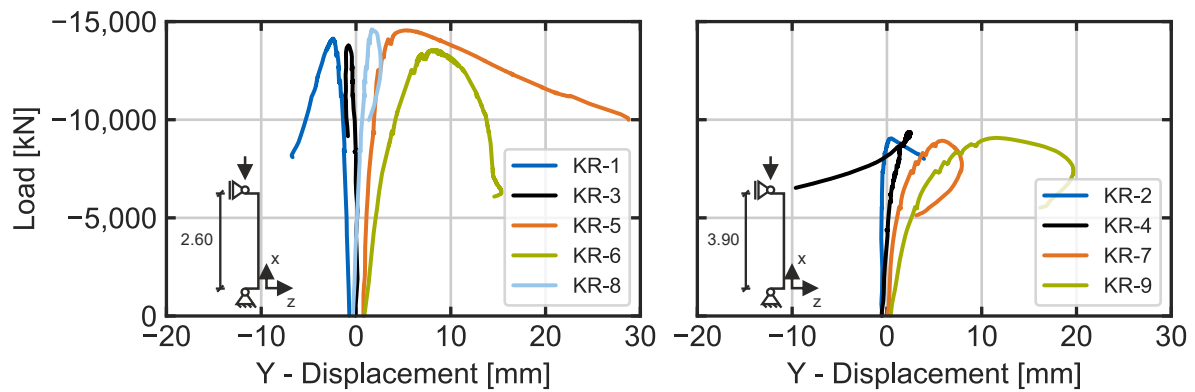


Figure 3-7 Displacement perpendicular to buckling direction of the buckling tests [63].

Table 3-2 Ultimate loads of the buckling tests.

Nr.	N_u [kN]	$u_{z,Nu}$ [mm]	$\varphi_{y,bottom,Nu}$ [°]	$\varphi_{y,top,Nu}$ [°]	M_{Nu} [kNm]	$(EI)_{Nu,mid}$ [kNm ²]
KR-1	-14,129	28.2	-1.809	1.531	565.8	16,905
KR-2	-9,047	53.8	-2.558	2.285	577.8	17,611
KR-3	-13,780	31.6	-2.182	1.948	592.9	12,679
KR-4	-9,373	55.2	-2.497	2.458	642.3	18,588
KR-5	-14,554	30.8	-0.040	2.200	626.6	16,633
KR-6	-13,545	26.5	-1.893	0.796	501.7	15,699
KR-7	-8,930	55.0	-1.959	2.329	611.2	18,448
KR-8	-14,605	28.2	-1.889	2.229	606.6	16,019
KR-9	-9,082	54.9	-1.842	2.269	610.2	18,847

The effective flexural stiffness was evaluated for the experimental tests using Equation (3-1). The necessary scale of the bow imperfection of the columns were recorded prior to the tests,

thoroughly described in Chapter 3.3. The strain gauges in the upper and lower measurement levels were used to evaluate the local flexural stiffness in these planes. In all tests, the flexural stiffness was higher in the upper and lower measuring planes than in the middle plane (see Figure 3-8). This was consistent with the assumption in the literature, whereby the flexural stiffness is reduced in the middle of the column due to cracking in the concrete and, with increasing stress, local plasticization. A higher flexural stiffness remains in the edge areas. The normatively determined value $(EI)_{eff}$ for simplified design method, considering $0.6 \cdot (EI)_c$ presumably displays an averaged value that lies between these stiffnesses [64].

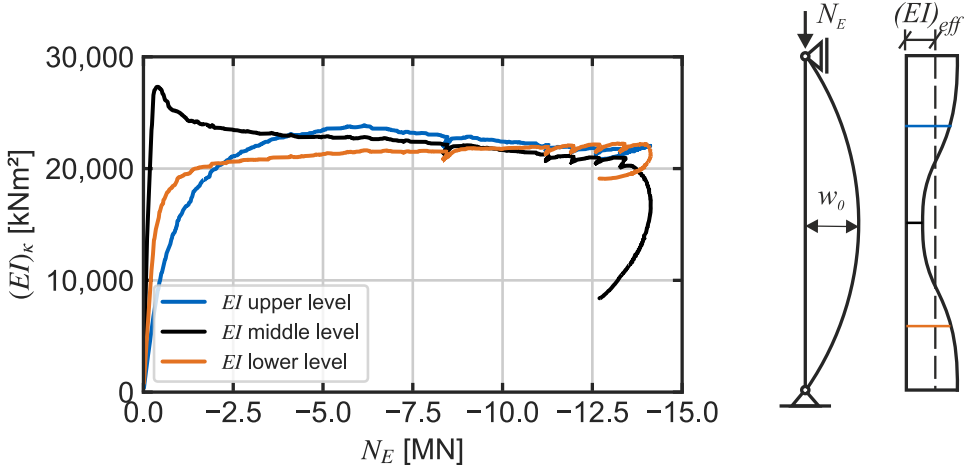


Figure 3-8 Flexural stiffness on upper, lower and mid measurement level of KR-1, scheme from [64].

The calculated flexural stiffness during loading (Figure 3-9) showed a sharp increase in all tests at the start of loading, with the values suggesting stiffnesses that could not be mechanically justified. On the one hand, this could be explained by an initial clamping effect of the bearings. Due to the initially low rotations, this resulted in increased static friction of the spherical bearing. On the other hand, Equation (3-1) resulted in an artificially high stiffness at the beginning due to the low curvatures. With increasing load, the flexural stiffnesses in the center of the test specimen approached an almost horizontal curve until they dropped shortly before reaching the maximum load bearing capacity. When comparing the flexural stiffnesses calculated in this way, it appeared that the flexural stiffnesses of the short columns varied more than those of the long columns.

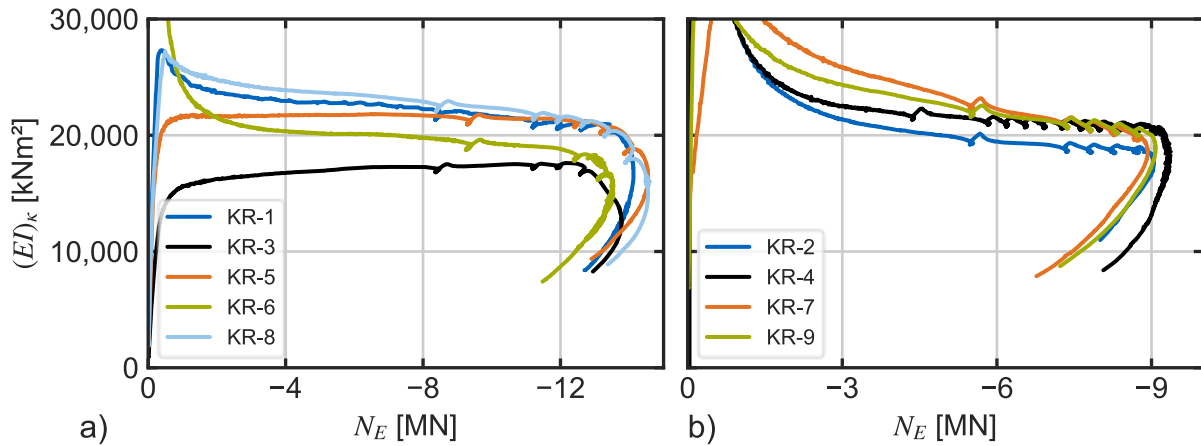


Figure 3-9 Calculated experimental flexural stiffness under applied load a) $l=2.60$ m and b) $l=3.90$ m using Eq. (3-1).

As a complementary method for determining effective flexural stiffness, the load deformation behavior was evaluated using the Southwell method. Figure 3-10 shows the test curve of horizontal deflection v ($= u_z$), the applied load P , and the relevant data for the Southwell plot. According to [22], the method is suitable for evaluating the elastic deformations, but the evaluation is only possible when the deformation approaches a sinusoidal shape. In the case of KR-1, for example, there was only little deformation at the beginning, so the lower limit of the data used for the plot needed to be defined at 35 % of the maximum load, and the upper limit was set at 95 % of the ultimate load. All tests showed that a linear regression was possible in the selected range. The R^2 value of the regression line was determined to be ≥ 0.995 for all tests. The critical buckling load could be derived from the slope of the regression line, and thus the effective flexural stiffness could be determined (Table 3-3).

It was found that the results of the Southwell plot showed an agreement with the flexural stiffnesses obtained from the method using the columns curvature. In some cases, there were larger deviations that could not be explained by the background of the individual methods. The calculated bow imperfection from the Southwell-plot w_0 are based on a centric equivalent beam and could not be used to evaluate the actual imperfections. There appeared to be a dependency between imperfection and flexural stiffness, with larger deviations between the flexural stiffnesses determined by the two different methods occurring at higher bow imperfection from the Southwell plot. For example, KR-7, which had the lowest imperfection, also had the highest agreement between the two values.

Table 3-3 Results of Southwell's method.

	KR-1	KR-2	KR-3	KR-4	KR-5	KR-6	KR-7	KR-8	KR-9
$N_{cr,SW}$ [kN]	25,018	11,238	22,092	11,570	22,212	21,799	10,435	22,808	11,373
w_0 [mm]	17	12	15	13	13	13	10	13	13
R^2	0.9957	0.9991	0.9975	0.9992	0.9977	0.9954	0.9984	0.9979	0.9986
$(EI)_{SW}$ [kNm ²]	21,025	19,897	18,566	20,483	18,667	18,320	18,474	19,168	20,136
$(EI)_x$ [kNm ²]	16,905	17,611	12,679	18,588	16,633	15,699	18,448	16,019	18,847

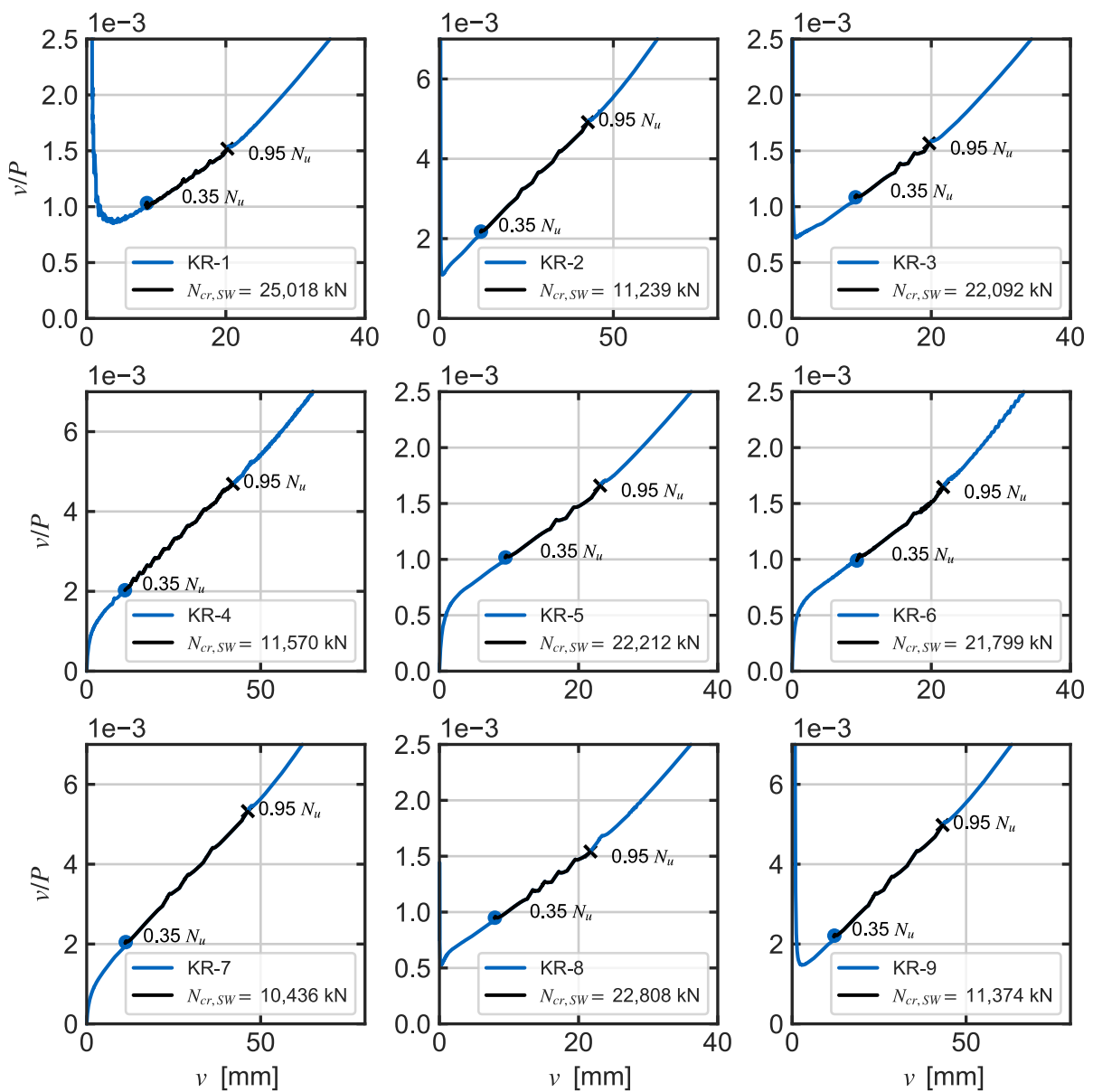


Figure 3-10 Southwell-Method on experimental buckling tests with critical buckling load $N_{cr,SW}$.

Strain gauges on each component of the section allowed the evaluation of the strain distribution over the height of the section. Figure 3-11 shows the strains over the section height in 25 % increments until ultimate load. It could be seen that a plane strain state occurred in all tests, regardless of the joint configurations used for the core profile. The sign of the strains was reversed only when the ultimate load was reached and tensile strains occurred on the side below the section and thus in the buckling direction, before which the entire section was fully compressed. In none of the tests a clearly noticeable strain difference between adjacent strain measurements was present, as would be expected with a partial bond.

Since the sequence of loading was known and was applied continuously during loading, stresses could also be determined from the strain measurements using correlated averaged material curves from the tensile tests above the linear elastic range. With respect to the experimentally determined yield strength of the material, it was thus possible to locate the cross-sectional areas where plastic material behavior occurred. In the KR-2 and KR-4 tests, some strain measurements failed in the central area, but in the KR-1, KR-3, and KR-5 tests, plastic strains could be detected up to the plates at the edge. In the columns with 8x20 mm plates KR-6 to KR-9, only the hollow profile reached its yield strength; no plastic deformation occurred in the plates. Regardless of the cross-section, it could be seen that the long columns experienced less compressive strain under load on the opposite side of the buckling direction. Concurrently, larger tensile strains occurred on the side facing the buckling direction.

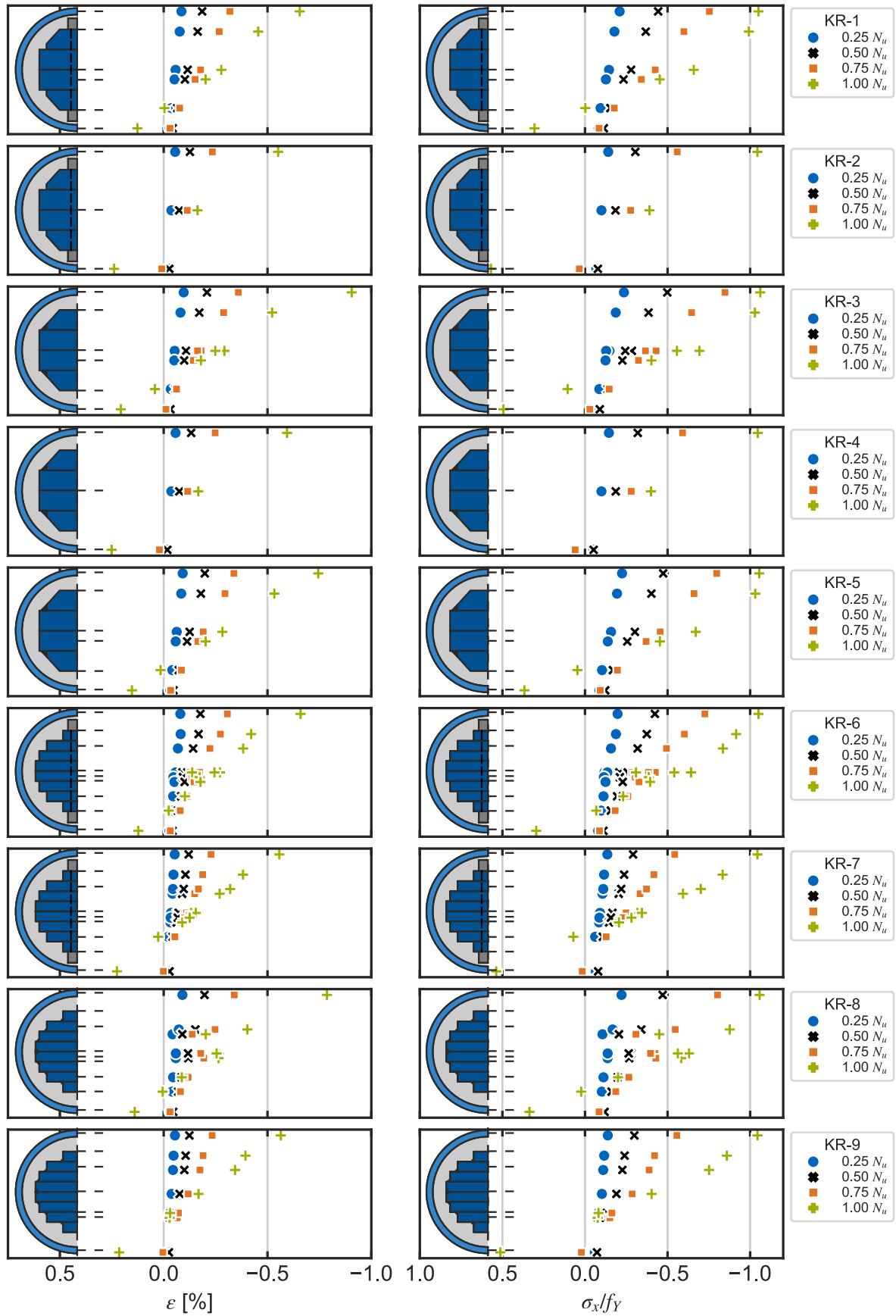


Figure 3-11 Strain distribution of buckling tests with yielded zones over the section height.

After the tests, the end plates were removed from all test specimens; in some cases, selected test specimens were also completely dismantled. At the open ends of the columns, a relative displacement was observed in the bolted cross-sections (KR-1, KR-2, KR-6 and KR-7; Figure 3-12 left), but no relative displacement of the laminated plates of all partially/fully welded cross-sections (Figure 3-12 right). Due to the strong deformation after exceeding the ultimate load, the seam between the end plate and the hollow section of KR-6 (bolted connection) fractured after discharge of the load (Figure 3-13).



Figure 3-12 Relative displacement of the core profile (left KR-6, bolted; right KR-8, partially welded) [63].



Figure 3-13 Rupture of the filled welding seam of endplate and hollow section (KR-6).

The tubes of the columns KR-3, KR-4 and KR-9 were fully opened. All test specimens showed largely intact concrete (Figure 3-14). No defects such as gravel pockets or segregation of the concrete could be detected. The documented cracks in the concrete surface could not be clearly attributed to its causes: fracture during the test or from the opening of the tube and the prevailing constraining forces from severe deformation. The existing cracks led to large, approx. 200-400 mm long concrete fragments (Figure 3-15). A narrow strip of broken concrete was visible in the compression area of the columns subjected to flexural buckling. It was unclear at what point of the load the cracking started; all test specimens were loaded further after reaching the maximum load until a defined final rotation of the bearings. This could also have led to increased crack formation, which was not yet prevalent when the ultimate load was reached. It was not possible to assess this correlation conclusively.



Figure 3-14 Concrete section after testing with tensile zone (top) and compressive zone (bottom).



Figure 3-15 Concrete section in the compressive zone (top) and tensile zone (bottom) for KR-6.

3.2 HSLP composite columns under four-point bending

The flexural stiffness is a critical feature in the determination of critical buckling load. The newly developed sections consist of high-strength laminated steel plates that are connected by locally concentrated shear connections using bolts and welds. Thus, the interaction between the individual plates and the resulting flexural stiffness of the columns is of interest. Four-point bending tests are considered an established method to experimentally determine the flexural stiffness of a wide range of composite structures. This method is significantly less influenced by imperfections than buckling tests. In contrast to a three-point bending test, the statically determined bearings results in a free length in the central area of the specimen with stresses from pure bending moment and without shear force. In a testing procedure, the flexural resistance of columns under four-point bending was investigated. Due to the high technical complexity, a test rig for pure bending stress without normal force was selected in this study.

Methods

Since the composite effect of the different components in the core profile is of particular interest for the composite columns presented, four four-point bending tests were carried out on representative cross-sections, similar to the buckling tests from Chapter 3.1 (Table 3-4). In addition to the locally bolted and welded cross-sections, test specimen BR-3 with the core profile fully welded along its length was examined as a benchmark.

Table 3-4 Experimental testing program under four-point bending.

Specimen	HSLP number x width [mm]	Shear configuration	Length [mm]	Tubular section	Concrete
BR-1		Bolted M24 8.8 (n=4)	3,550	244.5x12.5 mm S890QL	C30/37
BR-2	4xt = 40: 2x60/150 mm (chamfered) 2x150 mm	Partially welded ($l_w = 0.2 l$)	3,550	244.5x12.5 mm S890QL	C30/37
BR-3		Fully welded ($l_w = l$)	3,550	244.5x12.5 mm S890QL	C30/37
BR-4	4xt = 20: 2x56 mm 2x120 mm 2x150 mm 2x165 mm	Bolted M24 8.8 (n=4)	3,550	244.5x12.5 mm S890QL	C30/37

A specially designed test setup was developed to carry out the four-point bending tests. The applied loads were transferred to the floor of the test facility via vertical bearings realized by U-profiles and high-strength threaded rods. In order to avoid concentrated point loads due to the anchoring of the threaded rods in the hall floor, the test rig was designed so that the

hydraulic cylinders pressed the test body upwards against the bearings. Against horizontal deformation of the bearings, a stiffening effect was achieved via an additional horizontal U-profile connecting the vertical bearings. In this way, the profiles could be coupled together. The distance between load introductions and bearings was carried out in a grid of 1 meter, resulting in a remaining projection of 0.275 m at the free ends. The described test setup (Figure 3-16) was used for all tests with the same dimensions. The load was applied via hydraulic cylinder to half shells welded onto the hollow profile as load transfer. Two load cells with built-in spherical caps were inserted between the cylinders and the load application in order to ensure a vertically applied load. The cylinder paths were measured with linear variable differential transformers (LVDT). The cylinders were coupled hydraulically and force-controlled manually via a valve on the hydraulic unit. Slight deviations in the cylinder forces could occur due to friction differences in the cylinder seals. Horizontal movement of the specimen under load was ensured on the outer sides of the single-span beam by roller bearings. Strain gauges were attached to the outer tube and the core profile in the center of the specimen, attached prior to the manufacturing. The vertical deformation in the center of the beam was also monitored by LVDT. Before the start of the test, all end plates of the columns were removed so that possible relative displacement of the individual plates could be acquired using 3D laser scanning.

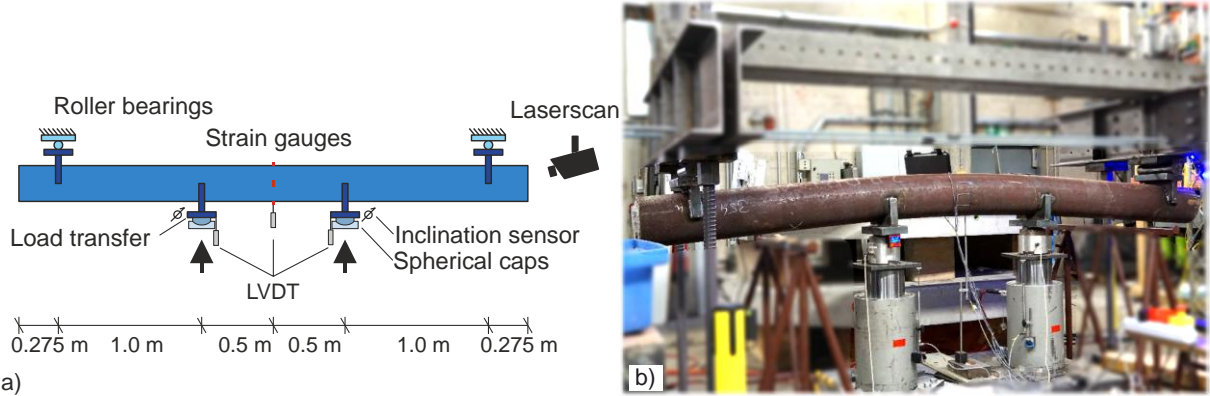


Figure 3-16 Four-point bending test setup a) schematically and b) in the laboratory.

The load was increased in several stages, as described in the previous chapter. In the range of plastic deformation, the load was held constant after every load step of 100 kN. Due to the ductile yielding of the cladding tube, no maximum loads or fracture criteria could be defined. A maximum inclination of 3° at the spherical caps was defined as the test termination criterion to avoid damage to the test equipment.

During the load of BR-1, the instrumentation experienced an interference signal during the test, presumably due to a damaged signal cable. Considerable noise signals made it impossible to evaluate the data. Individual strain gauges embedded in concrete onto the core profile failed

in all test specimens, presumably due to cable damage caused by the sealing silicone in the cable outlet from the specimens.

There were two methods for evaluating the results and determining the flexural stiffness of the test specimens. The statically determined system results in a single-span beam with a constant moment at midspan. Analogue to the buckling tests in Chapter 3.2.1, the flexural stiffness could be determined using Equation (3-1) via the section curvature and the acting moment. Alternatively, the flexural stiffness can be recalculated from the vertical deformation in the center of the span by rearranging the analytical description of the bending equation $EI \cdot w(x)$ of a single-span beam under the load of two symmetrical concentrated loads F :

$$EI \cdot w(x) = \frac{23 \cdot F \cdot l^3}{648} \quad (3-4)$$

$w(x)$	Vertical deformation at midspan
F	Acting load
l	Total length of the single-span beam, here $l = 3.0$ m

This results in a flexural stiffness, derived from the bending equation $(EI)_{BE}$:

$$(EI)_{BE} = \frac{23 \cdot F \cdot l^3}{648 \cdot w(x)} \quad (3-5)$$

Ideally, these two approaches would give consistent results as they are derived from the same bending line. However, in experimental testing, for example, it may be advantageous to use the less error-prone method of cross-sectional curvature, due to the possible elastic flexibility of the test stand, to avoid falsifying the stiffness by additional deflection of the structure.

Results

The bending test results were in line with expectations. As anticipated, there were minor variations in the load applied by the hydraulic cylinder. The holding phases, during which there was no movement and thus no friction between the cylinders and the seals, allowed the hydraulic pressure to equalize and the applied forces to balance out. The difference between the loads was a maximum of 11 % for the BR-4 and a maximum of about 5 % for the other

tests. With the help of the opposite lateral strain gauges on the tube, it was possible to rule out biaxial bending due to eccentric load application.

The load-deformation behavior is shown in Figure 3-17. The specimens initially showed linear elastic behavior with only slight differences between the different cross-sections. From an applied moment of 600 kNm, BR-4 showed non-linear behavior, whereas this only occurred for BR-3 at about 750 kNm and for BR-2 at about 800 kNm. Plastic deformation occurred, resulting in a significant increase in deformation with a slight increase in resistance. In the plastic range, specimen BR-3 with a continuous weld along the core profile showed the highest stiffness. Moreover, the specimens with bolted core profiles BR-1 and BR-4 showed the lowest stiffness.

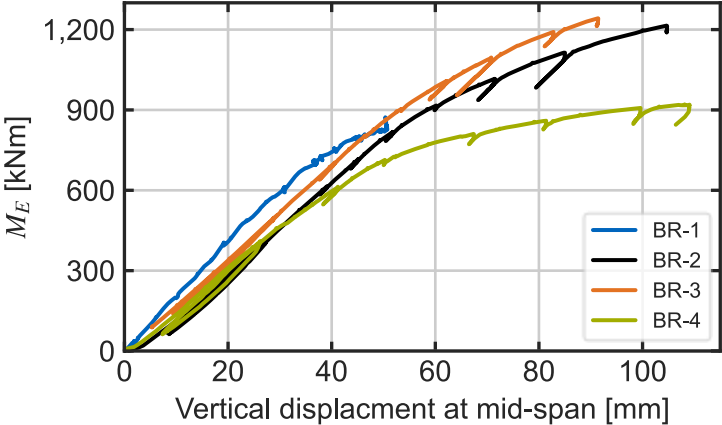


Figure 3-17 Load displacement behavior at midspan under four-point bending.

The relative deformation of the sections measured with the 3D scanner [65] was determined at regular intervals of the load levels. In the bolted core sections (BR-1 and BR-4), a relative deformation of individual core plates to each other was determined (Figure 3-18). Therefore, it could be assumed that the frictional resistance of the bolted joint was overcome, and slip occurred between the plates. In the case of the partially welded BR-2 and fully welded BR-3 core sections, no relative deformation could be detected at the end of the test specimens. It could be assumed that in both the fully welded and the limited length welded laminations, the weld seams were not fully plastic deformed over their entire length. Slip must have occurred in the unwelded region of BR-2, resulting in a less rigid deformation behavior under load.

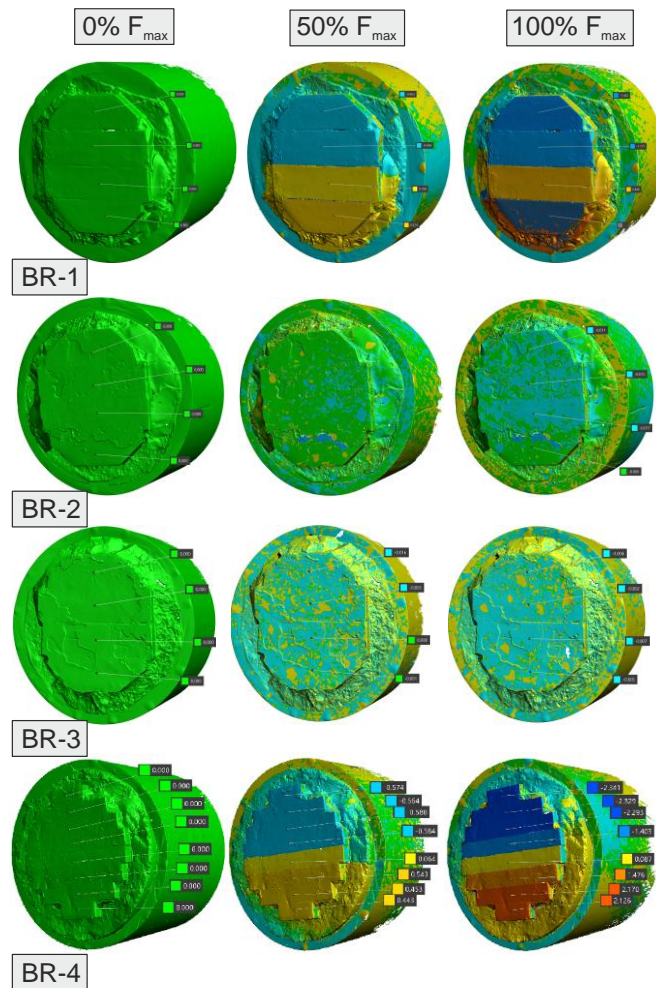


Figure 3-18 Relative displacement of individual plates in the core section at a) no load, b) 50 % of maximum load and c) 100 % maximum load.

The flexural behavior of the specimens was determined for all specimens using the previously mentioned method of evaluating the experimental flexural stiffness over the curvature of the cross-section (Figure 3-19, Figure 3-20). The use of the bending equation (Equation (3-5)) yielded deviating results, due to an anticipated elastic deformation of the bearing test rig. All the specimens initially exhibited almost constant flexural stiffness. The values showed good agreement with the approach for calculating the effective flexural stiffness $(EI)_{eff}$ according to prEN 1994-1-1:2024 [9] Equation (8.49). With increasing load, the tubular section underwent plastic deformation in all tests, resulting in a non-linear decrease of the flexural stiffness. Again, BR-3 exhibited the highest stiffness of all specimens. Initially, the flexural stiffness appeared to increase slightly until a horizontal plateau as reached. Only at a load of 800 kNm the flexural stiffness fell below the normative level and was followed by a non-linear decline. The flexural stiffness of specimen BR-2 was also at a level similar to that determined by the standard, although it dropped slightly below this value at an earlier stage. At high bending moments, there was an analogous drop in stiffness with a greater gradient than for BR-3. In contrast,

specimen BR-4 initially showed a flexural stiffness in good accordance with the normative approach but was already undercut at 450 kNm load. At 500 kNm there was a sudden drop in stiffness, which could have happened due to slippage inside the core section. As the load increased, the flexural stiffness continued to drop sharply.

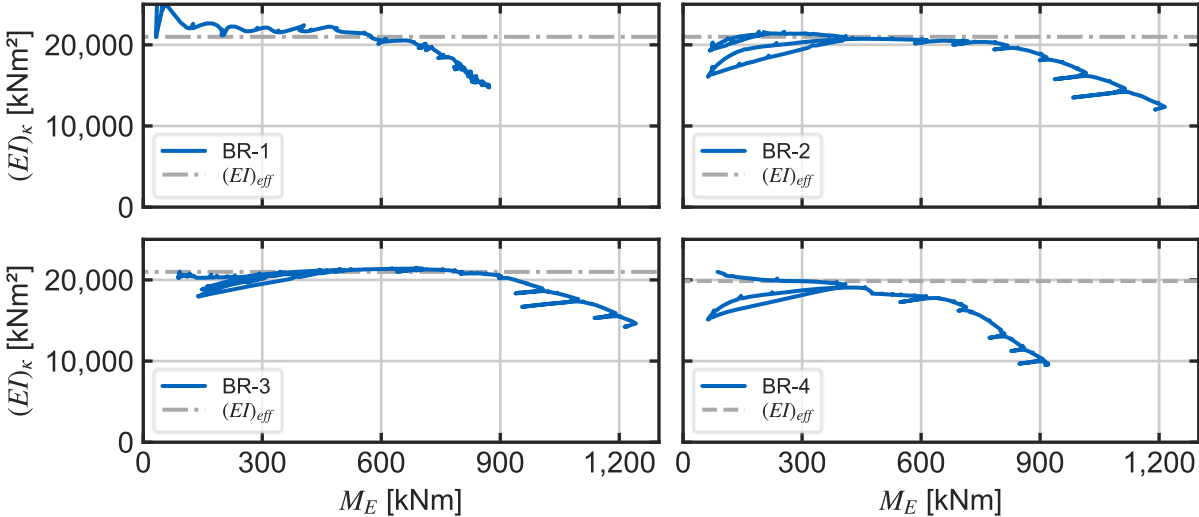


Figure 3-19 Experimental flexural stiffness over acting moment, compared with effective flexural stiffnesses $(EI)_{eff}$ [16].

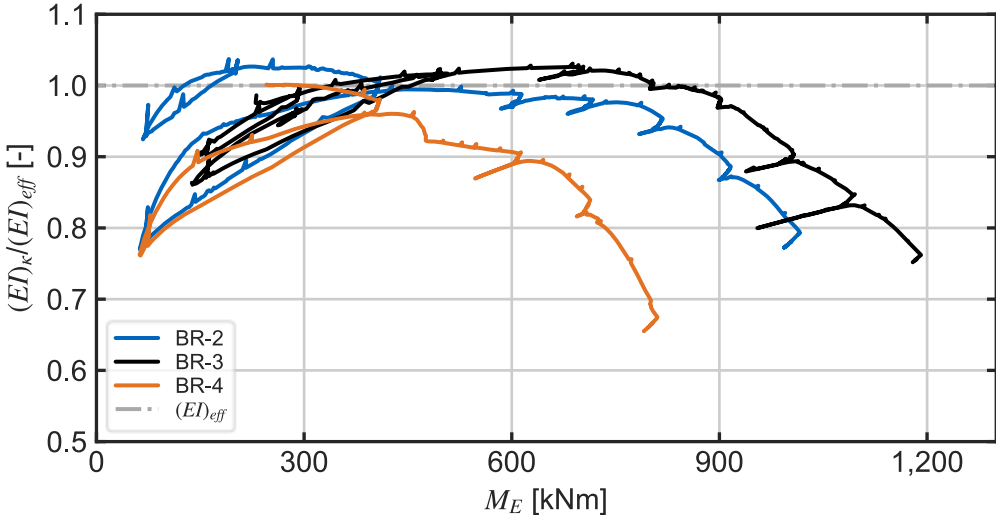


Figure 3-20 Comparison of the experimental flexural stiffness with the effective flexural stiffness from EC 4-1-1.

Using the strain gauges on the tubular section and in the core profile, it was possible to determine the strain distribution over the cross-section height during the test (Figure 3-21). A plane strain distribution over the cross-section in the axis of symmetry was observed in all tests until the maximum test load was reached. Thus, the requirements of the Bernoulli hypothesis

for the application of bending theory were met for midspan. Since the load path of the specimen was known, stress from the tensile tests could be assigned to the strains. It could be seen that no plastic strain occurred in any of the specimens up to 500 kNm. Plastic deformation of the tubular section was not reached in any of the tests until approximately 750 kNm. BR-3 showed consistently lower strains at each load level due to its higher flexural stiffness. Plastic strains of the laminated steel plates were only visible in the last load step. For BR-2 (partially welded along its length) and BR-4 (bolted connection), no plastic strain could be detected on the core section. This was probably due to the reduced stiffness caused by the slip between the plates. Consequently, an increase of deformation increased without further incline of resistance. This confirmed the observation from the 3D scans of the column ends, where slip between the plates could only be detected for BR-1 and BR-4. However, for BR-2 and BR-3 with partially and fully welded laminated plates along the length, no slip could be detected at the ends, indicating slip only occurred in the non-welded area for BR-2.

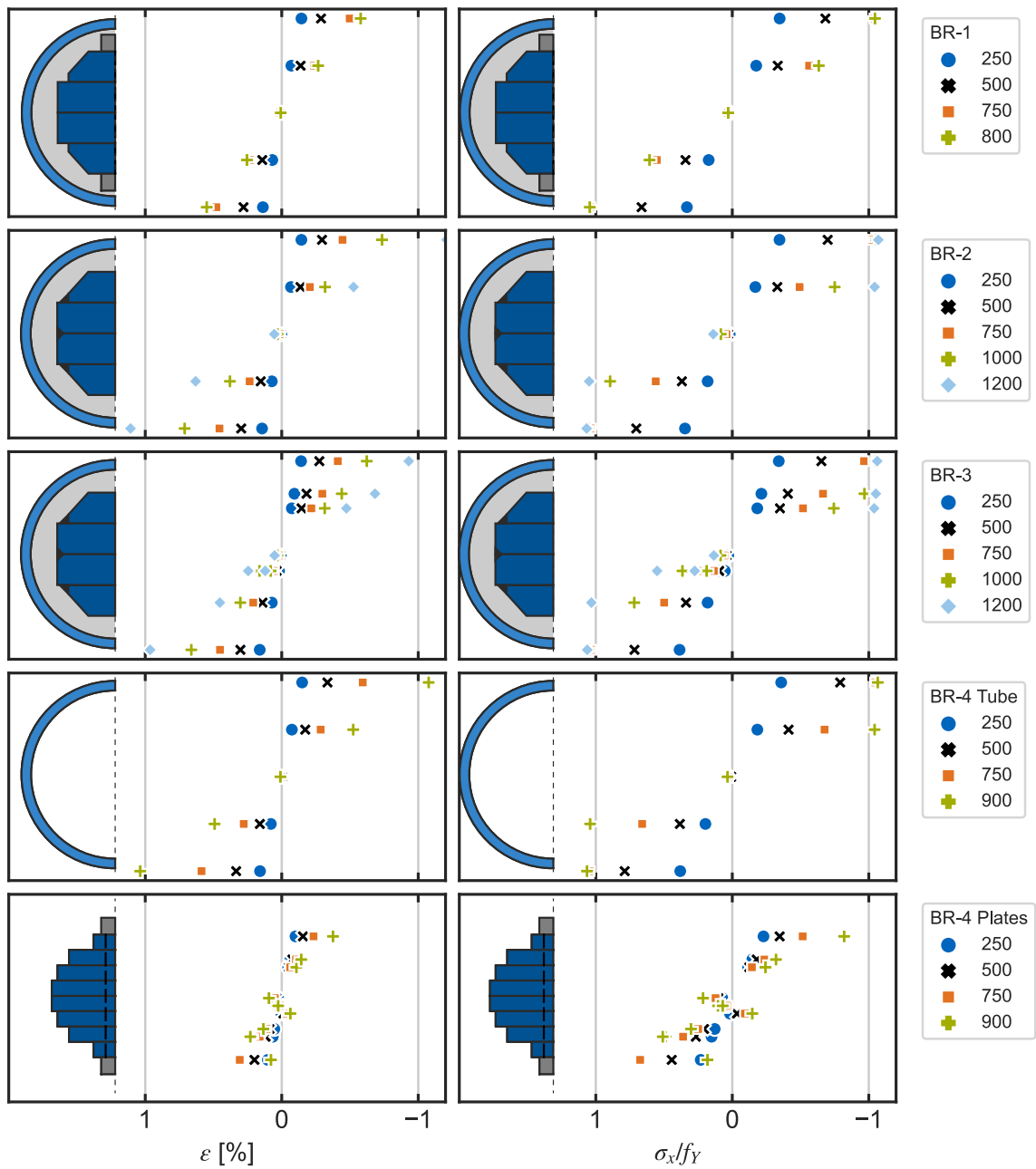


Figure 3-21 Strain distribution under four-point load, load steps in kNm.

3.3 Geometric imperfection measurements of HSLP composite columns

Imperfections have a major influence on load-bearing behavior of components subjected to compressive stress. In concrete-filled steel tubes containing a core profile, the geometric imperfections can only be recorded to a limited extent from the total cross-section. It must be assumed that a potential bow imperfection of the hollow section defines the global camber and that all other cross-sectional parts follow this shape [66]. Geometric imperfections of the tested columns were analyzed prior to and after the buckling tests. The imperfections determined were used in the further evaluation of the test results for the determination of the amplified bending load according to the second-order analysis and as a basis for numerical modeling.

Methods

With the aid of a 3D scanner, all test specimens were geometrically measured upright so that deformations due to dead load could be excluded. The scanner captured objects with an accuracy of $0.020 \text{ mm} + 0.040 \text{ mm/m}$ [65]. From the scans of the test specimens, the geometric imperfections could be evaluated in further steps using the product software. A centerline of each column could be derived from the scanned outer shell of the columns. The diagonal centerline was used to determine the start and end points of the column cross-sections and the deviation of the centerline from this straight line (Figure 3-22). Due to the three-dimensional recording, this bow imperfection could be evaluated both in the buckling direction and at right angles to it. The axis definition was selected according to a marking in the end plates (Figure 3-5).

A sinusoidal half-wave or parabolic bow imperfection could be determined for almost all columns. Only in the case of KR-6 did the camber more correspond to a full sine wave, so that the height of imperfection in the center of the column was almost zero. In the y-direction at right angles to this, the full sine wave was only evident in KR-8 and KR-9. The maximum bow height of the hot-finished profiles was 1.7 mm in the z-direction and up to 2.1 mm at right angles to this. Related to the column lengths, an imperfection of $L/2,000$ in the buckling direction or $L/1,400$ at right angles to it was determined for the columns with a length of 2.60 m, $L/2,700$ in or against the buckling direction and $L/3,000$ in the y-direction for the columns with a length of 3.90 m. According to the current standard for hot-finished hollow sections for steel construction DIN EN 10210-2:2019-06 Tab. 2 [67], an out-of-straightness of less than 0.2 % or 3 mm is required over every 1 m length. These tolerances were deemed to have been met here.

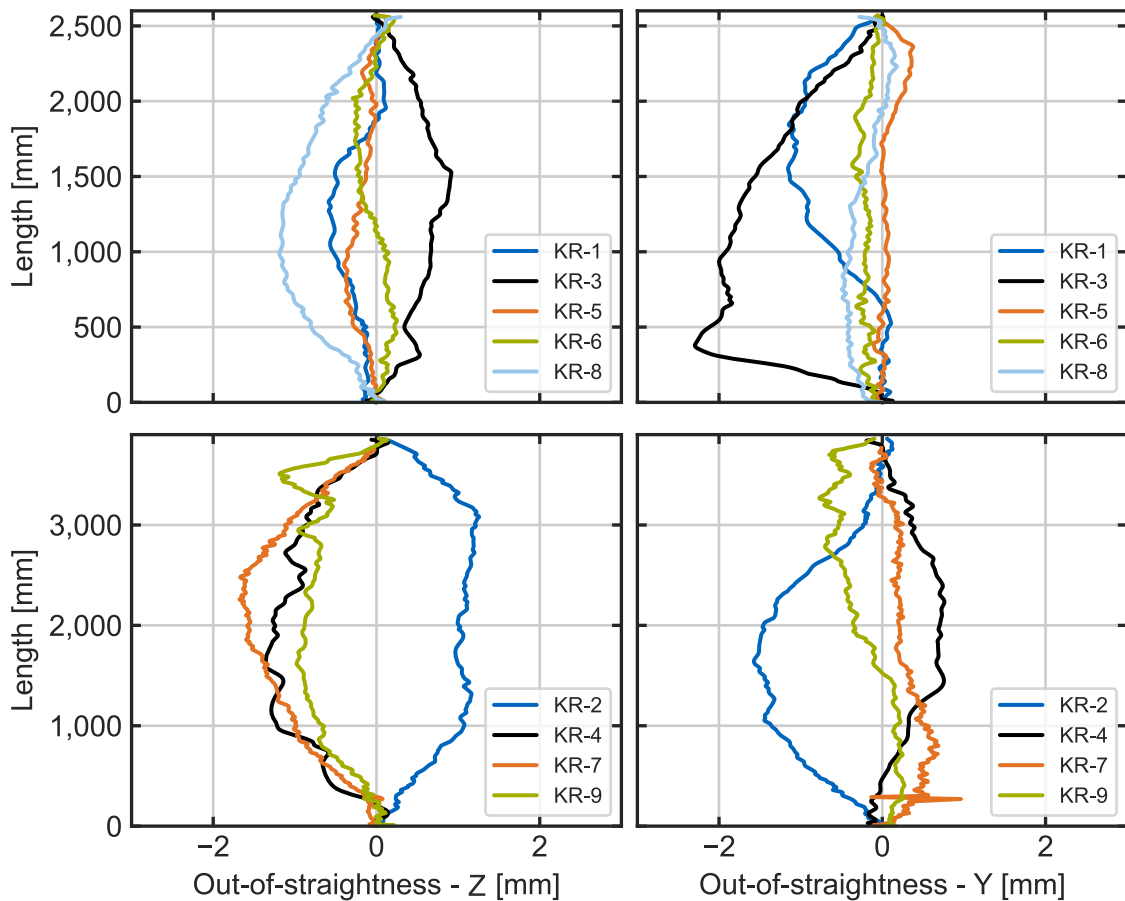


Figure 3-22 Bow imperfection of the specimens before test.

In addition to the bow imperfection, the deviations of the tubular cross-sections from the perfect circular shape could also be determined. For this purpose, sectional planes were extracted from the three-dimensional scans at the quarter points and a deviation from the ideal cross-section was determined in 1° increments. This revealed an almost perfectly round geometry with deviations of only up to 0.5 mm in the positive radial direction (see Figure 3-23). According to DIN EN 10210-2:2019-06 [67], manufacturing tolerances of up to $\pm 1\%$, i.e. ± 2.445 mm, are permissible for the cross-sections examined here. The wall thickness of the cross-sections was randomly measured by hand and showed a homogeneous thickness of 12.5 mm, without significant deviations. It would be possible to fall below the nominal thickness by up to 12.5 % within the tolerances. It could be shown that the hollow profiles complied with all normative limit values. Out-of-roundness, as a measure of the deviation between two coordinate systems positioned at right angles to each other, was only found to be a significant difference of 0.7 mm ($\pm 0.29\%$) in KR-4, which was also within the normative limit of 2 %.

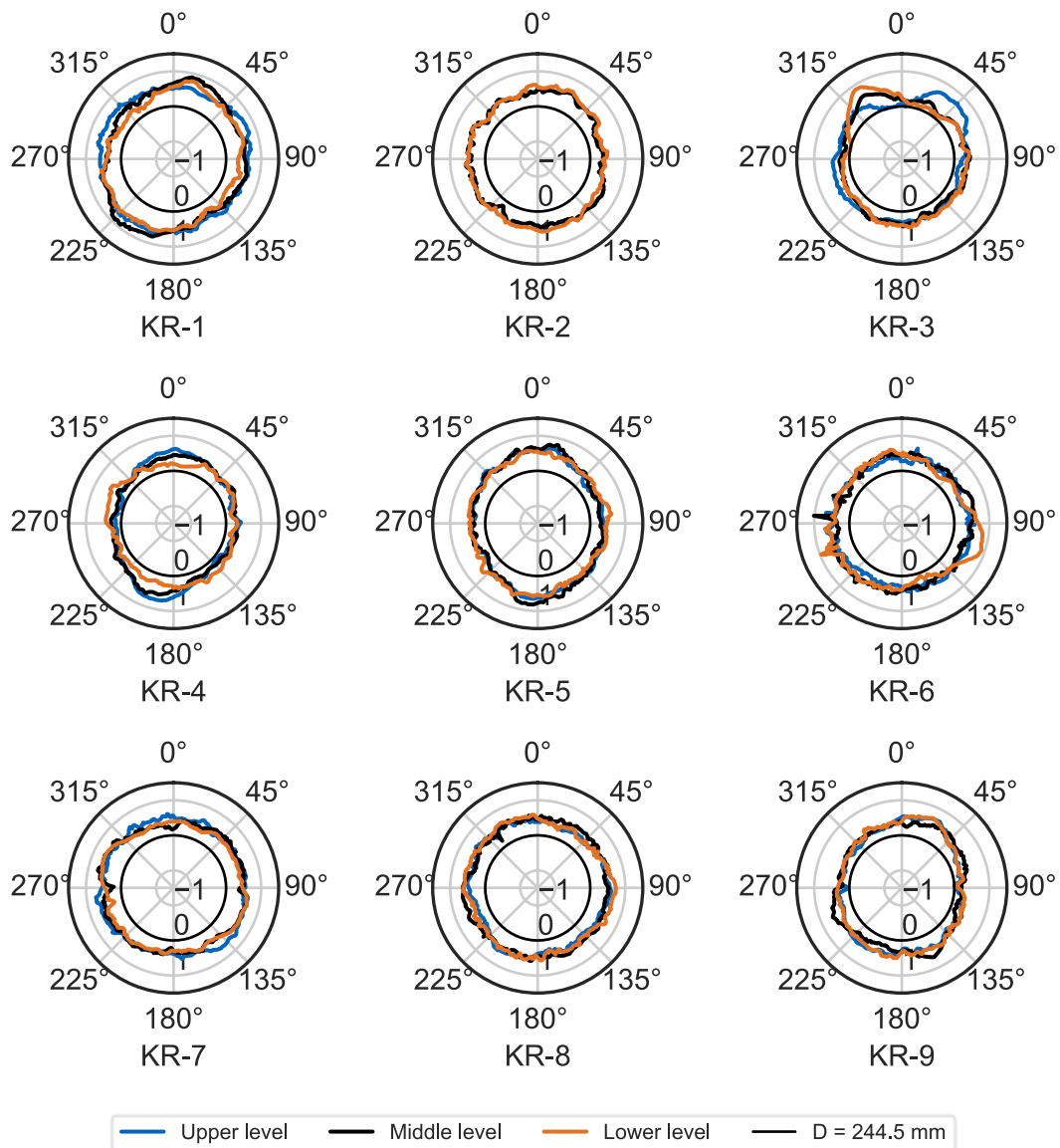


Figure 3-23 Radial imperfection of hot rolled tubular sections on three levels.

After the experimental tests, selected column cross-sections were disassembled. This revealed a different concrete cover between the tube and the core profile. For test specimens of KR-3, a concrete cover of 35 mm was found on the compression side and a concrete cover of 27 mm on the tension side, i.e. in the buckling direction (see Figure 3-24). It could therefore be assumed that the core profile could not be positioned centrally in the cladding tube. The reasons could be multiple:

- Planned mounting tolerance between laminated plates and hollow section
- Deviating tube geometry
- Cutting tolerances of the laminated plates
- Thickness tolerances of the heavy plates

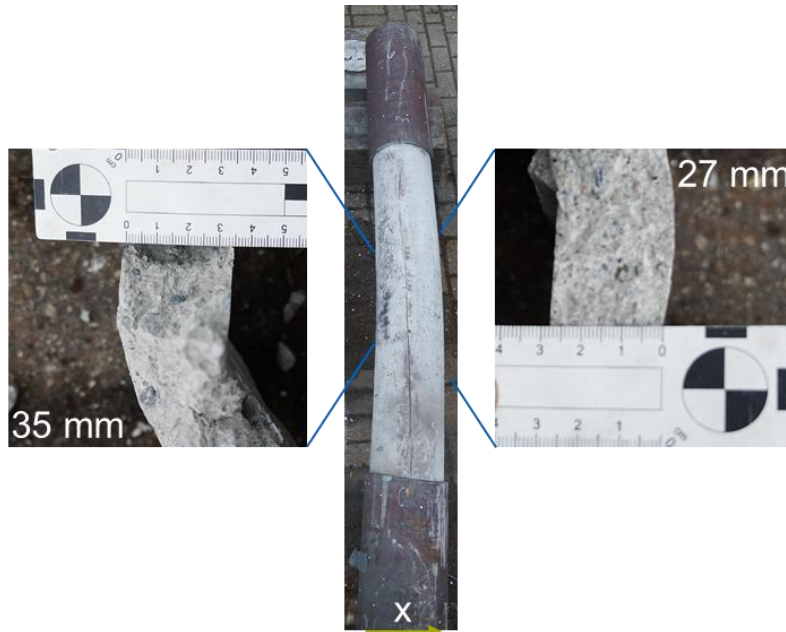


Figure 3-24 Non-centric position of the core profile of tested specimen KR-3, x as direction of buckling failure.

3.4 Residual stress measurements of high-strength steel plates

Next to geometrical imperfections, residual stresses determine the load-bearing behavior of structural elements under compressive loads as structural imperfections. Previous research did not investigate residual stresses of thick high-strength steel plates. As the steel plates have an essential proportion in the load-bearing resistance of the newly developed composite column, the quantification of the stresses is of large interest. The residual stresses of 41 mm thick steel plates of steel grade S960QL were measured in experimental tests using destructive and non-destructive procedures.

Methods

The residual stresses were measured in the longitudinal direction of the tested plates, corresponding to the principal stresses of the steel plates installed in the column. The sectioning method was used, and selected specimens were additionally examined by X-ray diffraction [68].

For the tests, three plates were cut from a 41 mm thick heavy plate using an oxyacetylene flame cutter (Figure 3-25). Specimens 1 and 2 were 150 mm wide, corresponding to the

lamellas used in the columns in Section 3.1 and 3.2. Specimen 3 was 300 mm wide. For the sectioning method, two sections were prepared for each specimen. As recommended in the literature, a length of 1 to 1.5 times the specimen width was provided in front of and behind the area to be tested. This avoided the influence of transverse flame cuts on the longitudinal stress state. The possible influence on stresses from post-treatment in the form of the shot peening (round grain, surface roughness $Sa\ 2\ \frac{1}{2}$ [69] resp. [70]) of the plates was investigated by comparison with untreated raw surfaces. Two test specimens with 15 and 30 segments per plate were provided.

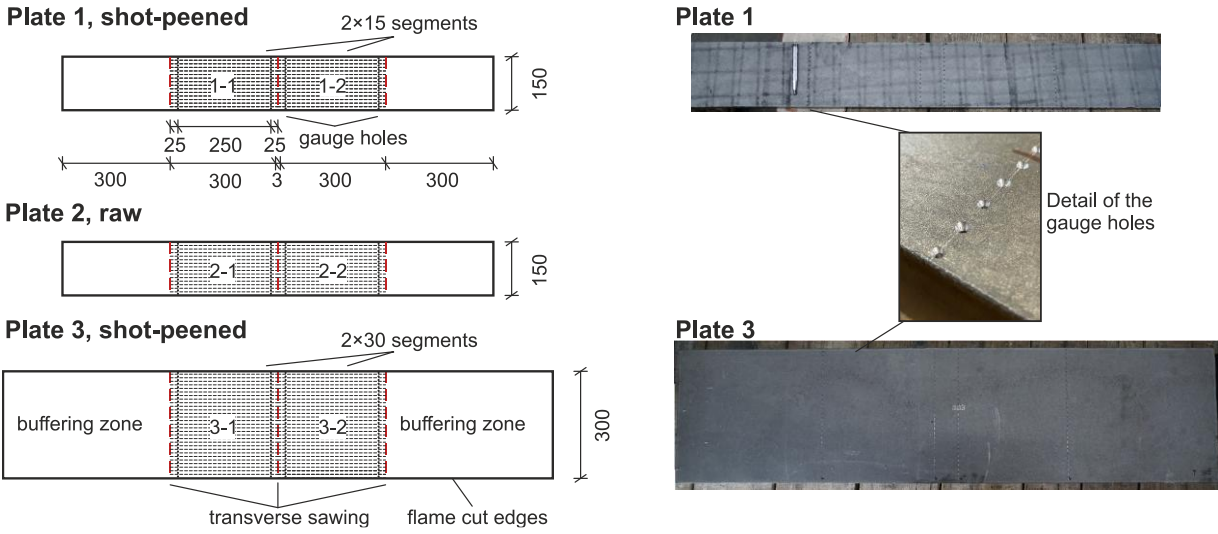


Figure 3-25 Test specimens for the sectioning method with prepared holes.

The components were prepared for the use of a manual deformeter. Strips of 10 mm in width were marked on the surface and prepared with a center drill so that the spherical measuring tip, approximately 4 mm in diameter, could be securely positioned. Care was taken to ensure that the holes were uniform in position and depth, free of burrs, and cleaned of impurities with compressed air. The measurement length of the selected deformeter (MGM 250, Figure 3-26) was 250 mm, with a measurement tolerance of ± 5 mm. The gage measured to a calibrated accuracy of 0.01 mm, giving a final stress measurement accuracy of at least ± 8.4 MPa ($210,000\ MPa \cdot \left(\frac{0.01}{250}\right)\ mm = 8.4\ MPa$).

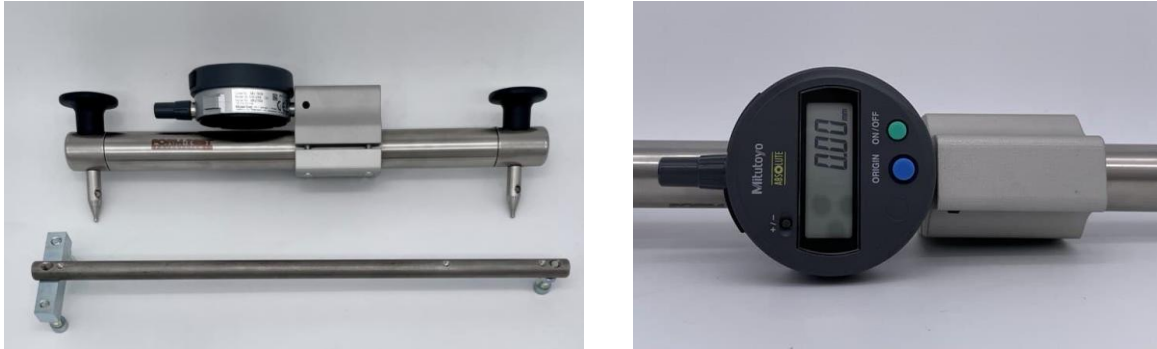


Figure 3-26 Deformeter MGM 250 with Invar calibration rod (left) and gauge with displayed precision (right).

The distance between the holes was measured using the instrument on the top and bottom. Due to the high susceptibility to interference with small occurring strains, each measurement was carried out at least three times. If the deviations of these three samples were < 0.015 mm, the measurement was accepted. For deviations of ≥ 0.015 - 0.02 mm, two repeating measurements were carried out. For larger measurement tolerances, the values were discarded, and the complete measurement was repeated. All measurements were carried out at a room temperature of $20\text{ }^{\circ}\text{C} \pm 2\text{ }^{\circ}\text{C}$ and without the effects of solar radiation, so that strains due to temperature effects could be excluded. Every ten measurements, the measurement distance was calibrated using the Invar bar to avoid temperature-induced strains. For data transmission, it proved practical to use electronic transmission to the recording computer.

The transverse cuts were made with a band saw. When cutting out the strips, noticeable wear of the tool became apparent after just a few cuts. Due to the high steel strength, the feed rate was greatly reduced, and despite constant cooling with the aid of coolant, it was not possible to prevent the segments from heating up considerably. The dimensional accuracy of the cuts could also not be guaranteed. As a result, the cutting process had to be changed to water jet cutting (Figure 3-27 b)). The main advantages of this process were the high precision of the cuts, the low wear on the cutting tool and the constant cooling provided by the surrounding water bath. Disadvantages such as high costs and low cutting speed were outweighed by the benefits in this case. The segments could be reliably cut out of the sections.



Figure 3-27 a) Strain measurement with deformer b) sawing of the segments and c) water jet cutting of the segments.

Again, the distance between the holes on the top and bottom of the separated segments was measured. Each measurement was carried out at least three times. If the deviations of these three samples were < 0.015 mm, the measurement was accepted. For deviations of ≥ 0.015 - 0.02 mm, two repeating measurements were carried out. For larger measurement tolerances, the values were discarded, and the complete measurement repeated.

To calculate the elongation, the change in length Δl before (l_{before}) and after separation (l_{after}) was determined using Equation (3-6). The difference in length related to the measuring length l corresponded to the elongation ε of the tested strip.

$$\varepsilon = \frac{\Delta l}{l} = \left[\frac{l_{before} - l_{after}}{l_{before}} \right] \quad (3-6)$$

Based on Bernoulli's theorem of plane cross-sections, the elongation of the middle fiber ε_m resulted from the mean value of the elongation on the top and bottom, according to Equation (3-7).

$$\varepsilon_m = \frac{\varepsilon_1 + \varepsilon_2}{2} \quad (3-7)$$

Since residual stresses only induce elastic strains, the previously prevalent residual stresses σ_{RS} could be determined from the change in length using Hooke's law by multiplying the strain by the modulus of elasticity E , Equation (3-8).

$$\sigma_{RS} = \varepsilon \cdot E \quad (3-8)$$

In areas close to the flame-cut edge, the component curved significantly due to the strong residual stresses. To simplify matters, this could be described as a circular deformation. Since

the measurement was taken at the arc length before cutting and the same geometry corresponded to the circular chord with a strong warping after cutting, a correction of the measured length was required. The following correction term from Thiébaud [61] was used for this purpose:

$$\varepsilon_{corr} = \frac{\left(\frac{\delta}{L}\right)^2}{6\left(\frac{\delta}{L}\right)^4 + 1} \quad (3-9)$$

ε_{corr}	Correctional term of strain measurement
δ	Chord height of camber
L	Length measurement of the chord

The determined strain was therefore calculated taking the correction into account:

$$\varepsilon = \frac{\varepsilon_2 - \varepsilon_1}{2} + \varepsilon_{corr} \quad (3-10)$$

The residual stress state in the thickness direction was determined using X-ray diffraction on three selected segments separated by the sectioning method.

An X-ray source was used to send rays at an angle of 35° onto the base material and the reflected radiation was measured using a detector. The procedure was carried out according to Debye-Scherrer using the $\cos\alpha$ -method [71, 72]. The reflected radiation corresponded to the maximum radiation intensity when the Bragg Equation (3-11) [73] was fulfilled:

$$2 \cdot d \cdot \sin(\theta) = \lambda \quad (3-11)$$

Using the known wavelength λ and the measured radiation angle θ , the distance d of the atomic lattice planes could be determined:

$$d = \frac{\lambda}{2 \cdot \sin(\theta)} \quad (3-12)$$

These correspond to the strain state of these lattice structures. Using the transverse strain coefficient ν and the modulus of elasticity of the material, the stress state could be calculated in this way. The measurement accuracy was ± 30 MPa [68]. To create a profile over the depth,

material was gradually removed from a measuring point using acid. In the process, the atomic lattice was exposed on the plate surface and the lateral cut edge using electrochemical etching.

Results

The results of the sectioning method showed high residual tensile stresses in the area of the flame-cut edges (Figure 3-28). These were overcome after the first cut, and low residual compressive stresses of approximately 30-70 MPa were found in the central area of the plate. The measurement data showed a high degree of scatter, which was higher for the narrower specimens (1-1 to 2-2) than for the wider specimens (3-1 and 3-2). Residual stresses technically must be equal; however measurement errors were noticed in the integration of all stresses, displayed as Integral I in the legend of Figure 3-28. The overall results were in good agreement with findings in the literature, e.g. [60]. The curves showed no differences with respect to subsequent processing (shot-peened or rolled skin). An influence of the specimen width could be seen in the level of residual compressive stresses, which averaged -40 MPa for all narrow specimens, while the average compressive stress of the wide specimens was -24 MPa. The distribution of residual stresses was in good agreement with literature studies on steel plates of different strengths [3, 61, 74]. Assuming a uniformly distributed tensile zone at the edge with stresses up to the yield point, the width of the zone could be calculated by integrating all the compressive stresses. This resulted in a width of 5-7 mm, which was in good agreement with the analytical determination using Equation (2-7) according to ECCS [18]. The amount and resulting dimensions of this approach were displayed as boxes in Figure 3-28. Although the measurements were subjected to large scattering, the dimensions of Equation (2-7) appear logic.

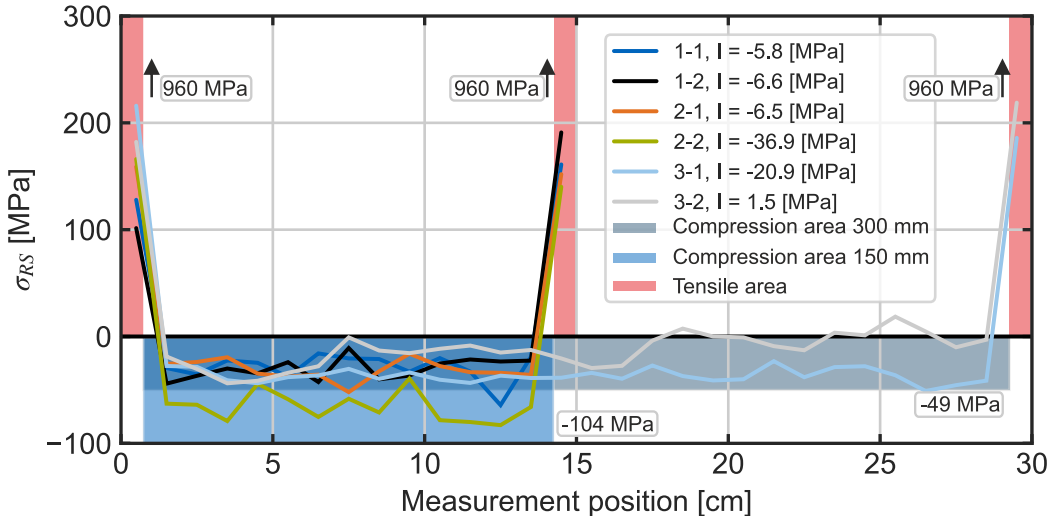


Figure 3-28 Longitudinal residual stresses from the sectioning method with the integral I as error measure in legend and comparison with constant stress blocks from ECCS [18].

Using X-Ray diffraction, residual stresses were evaluated in the thickness direction (Figure 3-29, Table 6-7, Table 6-8). This showed a clear difference between the shot-peened and untreated samples. In the case of the shot-peened specimens, residual compressive stresses of approximately -500 MPa could be determined up to a depth of 250 μm in the edge region. Thereafter they were similar to the untreated sample at -100 MPa. Compressive residual stresses were detectable up to about 800 μm , from which internal tensile residual stresses of about 16 MPa were determined using the equilibrium condition. Further measurements at greater depths were not possible. To confirm the measurements and to obtain a profile of the plate thickness, the longitudinal residual stresses were determined at larger intervals on the cut surface of the segments. Again, a compressive residual stress of -100 MPa was found near the rolled surface, changing to a slight tensile residual stress after about 8 mm. At equilibrium, the tensile stress in the mid-range is close to 0 MPa, which is within the tolerance of the measuring method. To illustrate the curve, a polynomial fit was inserted into the curve of the highly scattering data points (Figure 3-30, Table 6-9).

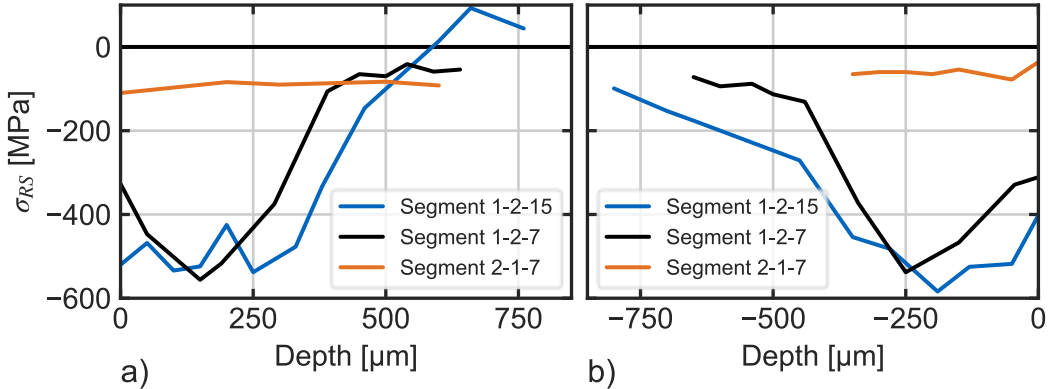


Figure 3-29 Longitudinal residual stresses from X-Ray diffraction on shot-peened (1-2) and raw surfaces (2-1) on the a) upper and b) lower side of the section.

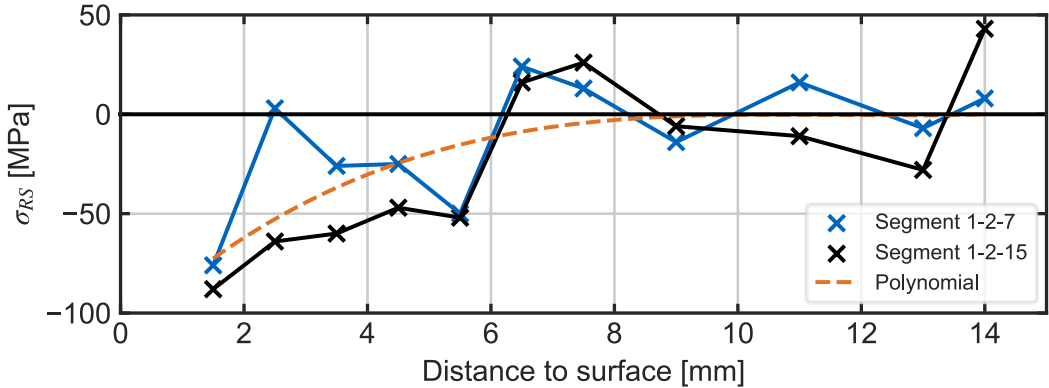


Figure 3-30 Longitudinal residual stresses from X-Ray diffraction on the surface of the water jet cutting edge.

3.5 Discussion of the experimental results

Buckling tests and their geometric imperfections

Nine large scale buckling tests provided insight into the structural performance of the new composite sections. The tests were conducted on two lengths of specimens with different shear connection of the HSLP. The load was applied with a constant eccentricity of 10 mm for all tests. Experimental loads showed higher compressive resistances for shorter columns as for larger columns, as anticipated. Flexural stiffness was determined from the acting moment after second-order analysis using lateral deflection, eccentricity, and initially measured bow imperfection. Obtained values showed a high scattering and no definitive conclusion could be drawn with respect to different shear connections of the individual plates. Yet, it was observed that the longer specimens had a higher flexural stiffness than the shorter specimens.

Geometric imperfections of the specimens were recorded externally, prior to the buckling tests. Bow imperfections of the tube were found minor and within the range of manufacturing tolerances. Selected cross-sections were dismantled after the tests. The positions of the core were found to be eccentric with respect to the center of the tube section both in and against the buckling direction with up to 5 mm. This meant a positive effect on the ultimate load for geometric deviations in the direction opposite to the buckling direction; The initial eccentricity was reduced. Conversely, an eccentric position in the buckling direction reduced the maximum resistance due to an additional increase of the initial eccentricity. Due to these deviations, the acting bending moment and results of experimental tests must be corrected and can hardly be transferred to ideal cross-sections. Since the test specimens were built under typical conditions of the industry, the occurrence of geometric imperfections in form of a misplaced core profile seemed inevitable. Removing the endplates of all specimens revealed a relative displacement of individual plates of the core section only for bolted specimens. Welded specimens indicated no relative displacement and thus no plastic deformation of the welds on the ends of the plates.

The two methods for evaluating flexural stiffness from test data have shown various advantages and disadvantages in their implementation. In the method using the cross-section curvature, the acting bending moment is determined from factors that must be measured as accurately as possible. However, it was shown that the core profiles of the test specimens were eccentric, resulting in a deviating, unknown total eccentricity and thus an incorrect determination of the acting moment. Therefore, the experimental results of this method are not directly applicable for further use and no clear difference can be pointed out regarding different shear connection of the HSLP. The Southwell method, on the other hand, only determined the flexural stiffness via the horizontal deformation as a scattering variable, whereby the optical

measurement technology used here was also subjected to greater scattering. Additionally, it should be noted that the Southwell method determined the critical buckling load from the reciprocal of the approximated straight slope. This method was found to be extremely sensitive to the selection of data points used. Small deviations in the raw data or changes in the selection range of the data strongly affected the equation and led to a considerable influence on the result.

The eccentric load test method proved to be a useful means of clearly defining the buckling direction and avoiding damage to the test equipment. However, due to the bending stress of the eccentric load, the results could not be used for comparison of buckling curves. The effect of residual stresses, which as structural imperfections can significantly influence the bearing load under compressive load, are generally minor in eccentric loaded tests. A guideline for the performance of buckling tests has been developed by [75] and recommends the use of centric tests, but with the note that the recommendations are also valid for eccentric test methods. Thus, it is up to the testing institute to choose between centric and eccentric tests with their respective advantages and disadvantages. Due to the very ductile failure of the concrete filled steel tubes observed in these tests, a sudden failure and thus endangerment of the test facility could be excluded for further tests under deformation-controlled load. Ultimately, however, the method chosen could be considered useful for the effective flexural stiffness investigations performed here.

Four-point bending tests

Four four-point bending tests were conducted on the innovative columns and enabled further understanding of the flexural behavior. The experimental tests were conducted on columns with different configurations of the shear connection of HSLP under the influence of isolated bending load and no axial load. Important findings included the lack of plastic deformation of fillet and butt welds in the core section even for larger bending moments. Longer segments of welding seams yielded a higher flexural stiffnesses at similar deformation, indicating that slip occurred in the unwelded segments. In contrast, bolted sections displayed relative displacements of the individual core plates at the specimens' ends indicating slip over the whole length. Consequently, welded sections presented higher flexural stiffness compared to bolted sections. The results could be compared to the analytical solution for composite columns provided by the code. The values showed a high level of agreement in the elastic region. With first yielding of the tubular section, the experimental flexural stiffness was significantly reduced.

Interfering signals of specimen BR-1 have made it impossible to systematically analyze the conducted results, reducing the scope of research. Overall, the tests of pure bending proved to be little affected by manufacturing imperfections and thus yielded in reliable results. Nevertheless, the experimental test rig exhibited elastic deformation under load. The flexural resistance of the specimens could only be derived from the section curvature, as the measured deflection included a total displacement of specimen and test rig.

Flexural stiffnesses determined in the buckling tests were falsified by later discovered non-centric positions of the HSLP core. A comparison of the results for both experimental testing series was precluded.

Residual stress measurements

Longitudinal residual stresses of six 41 mm thick high-strength steel plates of steel grade S960QL were conducted experimentally using destructive testing by separating segments of the specimens. Further non-destructive testing using X-ray diffraction was performed on selected cut segments. Prior to the test the plates were cut using oxyfuel cutting and had two different widths. Two of the specimens underwent no post-treatment whereas the other four specimens were shot peened. Results from the sectioning method were subjected to large scattering, exhibiting large tensile stresses on the specimens' edges and comparatively low compressive stresses in the center area. The wider specimens had less compressive stresses compared to narrower specimens, whereas the tensile stresses were at a similar level for all specimens. Differences between untreated and shot-peened plates was only recognized as increased compressive stresses close to the surface of the segments up to a depth of 800 μm .

In the case of the sectioning method, the strip width of 10 mm per cut was found to be insufficiently small to achieve a higher local resolution of the residual tensile stresses due to the strong gradient of residual stresses in the area of the flame cuts. However, the strip width was limited by the minimum dimensions for reliable cutting with a water jet or saw and could not have been selected smaller. No final conclusion could be drawn concerning the maximum tensile residual stresses on the flame-cut edges. The assumptions from literature [18] that the stresses reach the yield stress were therefore adapted. Following the approach of Equation (2-7), only little difference would be achieved by a modification of tensile stresses lower than the yield stress. Due to the comparably large area of compressive stresses, the amount of compressive stress would not change significantly. Still, the region of the tensile stresses appeared overcome just after the first segment, indicating a narrow area of tensile stress. A more general modification of the presented simplified description might be achieved with measurements of different plate thicknesses. Further insights might be available to clarify the

width of the tensile zone, see Equation (2-8). In this limited scope of research this could not be examined. Thus, lacking further information, the presented approach from ECCS [18] can be accepted with sufficient accordance.

The sectioning method traditionally is a simple but robust procedure to examine the residual stresses of steel sections and was widely accepted for centuries even until today (e.g. [76]). An alternative method of the sectioning method would be the use of strain gauges instead of the manual deformeter to measure strains (e.g. [77]), which minimizes the measuring tolerance of the manual measuring tool used by the user. The effort involved in the cutting process can be further reduced by partial cutting. However, this modification is limited, as strain gages are very susceptible to moisture and mechanical manipulation. The measurement of local stresses might imply higher scattering, which cannot be averaged in contrary to the significant length of measurements implemented in the presented investigation.

The results of X-ray diffraction were subjected to high scatter but helped understanding the spatial distribution of stresses more closely as a complementing method to the sectioning method. More reliable findings could only be obtained by frequently repeating measurements. The obtained differences of superficially increased compressive stresses due to post-treatment turned out to be at such micro-scale, their influence could be neglected in the following investigations.

Further measurement methods for residual stresses and decision-making aids are given in [78].

4 Numerical investigations

Experimental tests of the HSLP composite columns under axial load and pure bending enabled a first understanding of the bearing behavior of the innovative columns. Although, no clear results could be determined regarding the interaction of the individual components and the influence of alternated section designs. The buckling loads determined experimentally included an eccentric load and can therefore not be compared to buckling curves. Overall, the scope of the investigated columns was limited and thus must be complemented with finite element models. Detailed investigations of geometric and structural imperfections and other material properties provided fundamental information. The numerical models were designed, verified, and validated on experimental results and conducted as geometrically and materially nonlinear analysis with imperfections included (GMNIA). Detailed investigations of the buckling behavior of isolated plates and tubes were conducted to anticipate the buckling behavior of individual components. It was the general aim to determine the flexural stiffness of columns with HSLP as core and ultimately the buckling behavior of centrally loaded columns with different diameters, lengths, and shear connections to finally conclude a generalized method as basis for design.

4.1 Model setup

The composite columns were generated in the finite element application Abaqus from Simulia [79] using three-dimensional solid elements. C3D8R elements were selected as standard elements. These have eight nodes and reduced integration, making them less susceptible to shear locking effects and are very computationally efficient. First, the experimental specimens were completely redesigned to verify them using the test results. For the buckling tests, the experimental setup was considered with its full dimensions, neglecting symmetry conditions to simulate the free deflection by the spherical bearing (Figure 4-1). Later parametric studies were mapped axisymmetric along the longitudinal direction of the column to optimize the computation time; the boundary conditions were selected accordingly along the axis of symmetry (Figure 4-2). The material laws of the model were based on miniature tensile tests of the steel components and concrete compression tests on concrete cylinders at the time of testing. The material curves used were averaged from the test data.

In the experimental tests of the column cross-sections under four-point bending, a uniaxial bending without biaxial deflection was determined. Thus, for the modeling in Abaqus, the symmetry in the longitudinal direction of the column was considered in addition to the central symmetry condition. The distances between the rotation points of the roller bearings were

considered by connecting reference points for load application with kinematic couplings to the cladding tube (Figure 4-3).

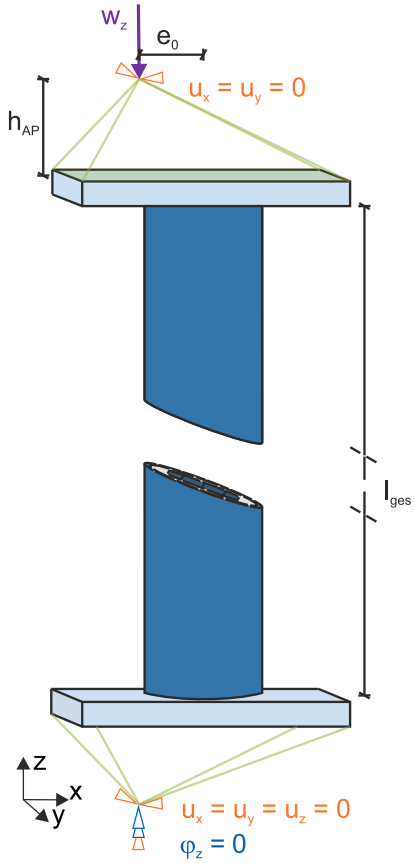


Figure 4-1 Boundary conditions of the Abaqus buckling model.

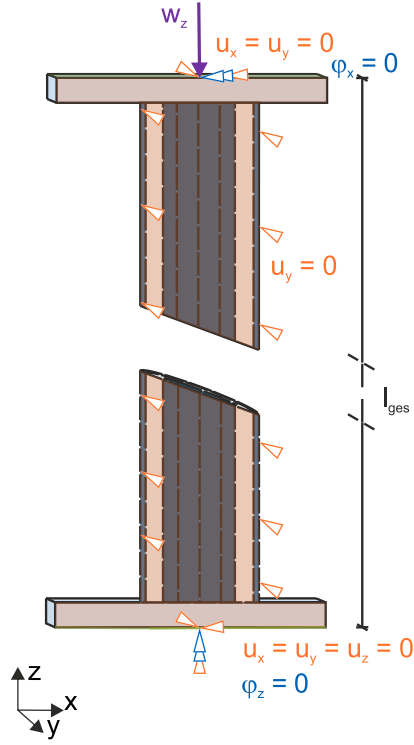


Figure 4-2 Boundary conditions of the parametric Abaqus buckling model with symmetry conditions.

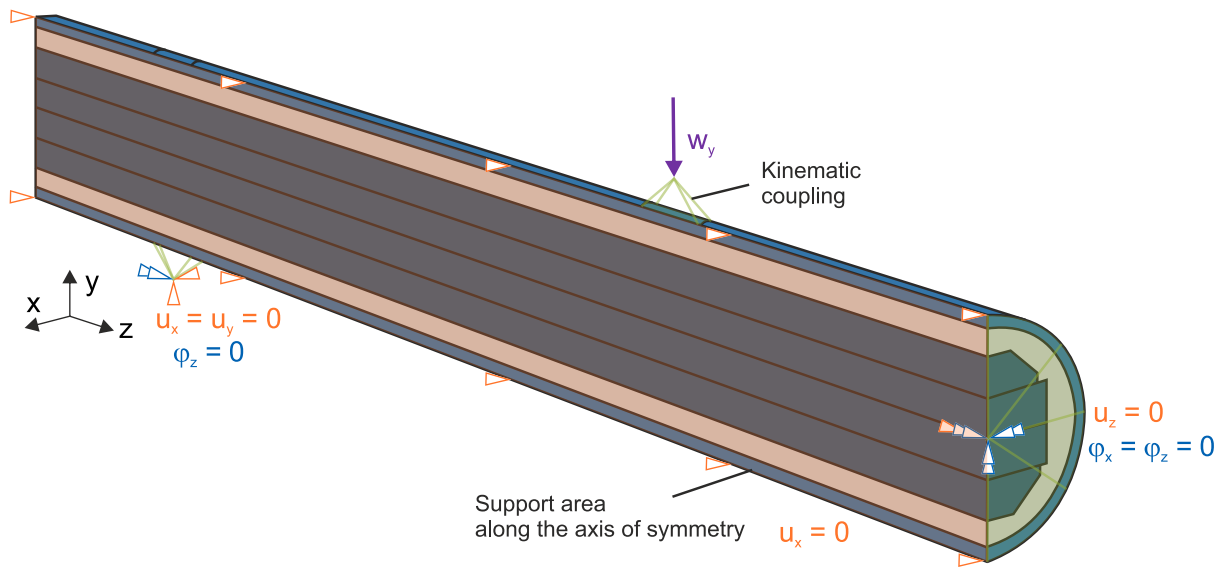


Figure 4-3 Boundary conditions of the Abaqus model under four-point bending, coupled surfaces (green) and planar bearing (orange).

The concrete was depicted using a nonlinear model supported by the concrete damaged plasticity (CDP) model. A model for the compressive behavior according to Sargin [80] represents an established method and is also recommended in EN 1992-1-1:2011-01 [81] and was adapted here (Figure 4-4). Deviating from the latter recommendation, the ductility parameter D of 0.7 was chosen larger than the recommended 0.0; the thereof resulting underestimation of the compressive strength reduction of the concrete was accepted with the aim of achieving a more stable convergence of the calculations. The tensile behavior was modeled according to Hillerborg [82]. The damage parameters for compression d_c and tension d_t defined softening after exceeding the limit strains ε_{c1} and ε_{ctm} , respectively. Lacking experimental data for the two parameters they were calculated following the common practice with estimating Equations (4-1) and (4-2) (e.g. [83, 84]). The remaining input parameters of the CDP were chosen according to Kueres et al. [85] for normal strength concretes, including the mean value of the modulus of elasticity E_{cm} from experimental data (see Table 4-1).

$$d_c = 1 - \frac{\sigma_i}{f_{cm}} \quad (4-1)$$

σ_i	Overcritical compressive stress
f_{cm}	Mean compressive strength

$$d_t = 1 - \frac{\sigma_i}{f_{ctm}} \quad (4-2)$$

σ_i Overcritical tensile stress

f_{ctm} Mean tensile strength

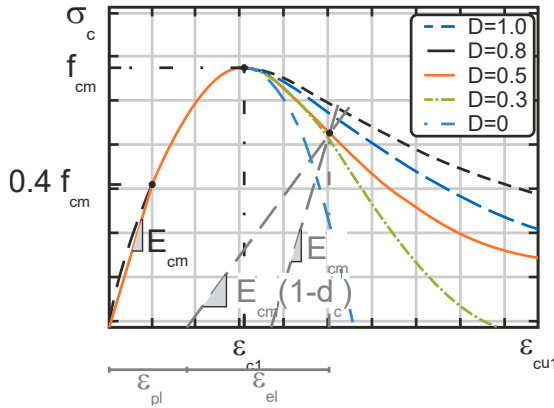


Figure 4-4 Compressive behavior of concrete with CDP acc. to [80].

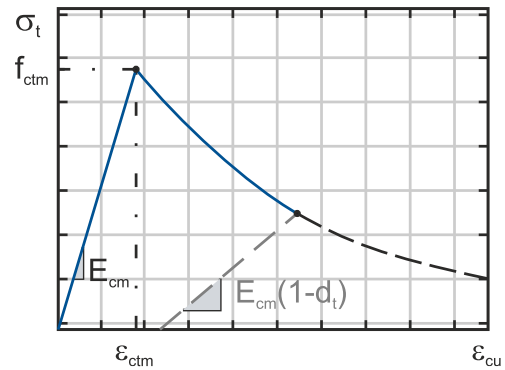


Figure 4-5 Tensile behavior of concrete acc. to [62].

Table 4-1 Input parameters for the CDP module.

Young's modulus [MPa]	ν [-]	ψ [°]	ε [-]	σ_{b0}/σ_{c0} [-]	K_c [-]	D [-]
20,684	0.2	35	0.1	1.16	0.67	1×10^{-4}

For parametric investigations, the material models of the steel cross-sections were simplified to a bilinear stress-strain behavior with a tangent modulus of $E/100$ according to prEN 1993-1-14:2023 5.3.3 (3) [37]; the nominal values were used as the yield strength f_y (Figure 4-7). As the mean moduli of elasticity determined in the miniature tensile specimens (Figure 4-6) were less than 210,000 MPa, the measured values were used for the parametric analysis. The concrete model was not changed further due to the overall minor influence. The desired non-linear and softening effects were more important.

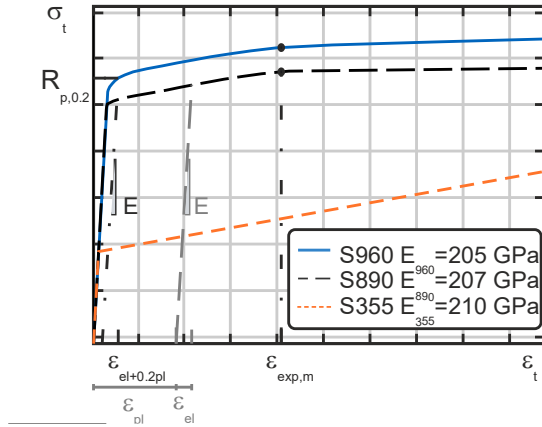


Figure 4-6 Material behavior of the steel sections for recalculation.

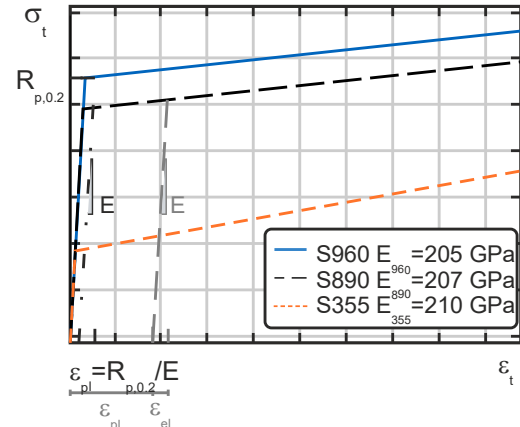


Figure 4-7 Bilinear material behavior of the steel section for parametric studies.

The plates were shot-peened to a surface roughness of Sa 2 ½ ([69] resp. [70]). Small part tests to determine the coefficient of static friction of similarly treated plates yielded a value of 0.34. DIN EN 1090-2:2018 [86] recommends a coefficient of static friction of 0.3 to 0.5. In consequence, a frictional and detachable "hard contact" with a coefficient of friction of $\mu = 0.3$ was defined between all non-welded contact surfaces. A simplified modeling of all welds was performed using rigid solid connections, called "ties", both for the connection of the cladding tube and the end plates and for the welds between the plates.

Geometric imperfections of the buckling tests were considered as an amplified buckling mode using an upstream buckling analysis prior to the nonlinear analysis. The respective chord of the bow imperfection was selected according to the measurements, see Chapter 3.3. As a common value from several literatures (e.g. [75]), a global bow imperfection of $L/1,000$ was considered for the parametric calculations. The tolerances of the plate thicknesses were determined on the basis of the manufacturer's delivery certificates and considered in the recalculations using an adjusted thickness, accordingly. For parametric investigations, nominal plate thicknesses were used.

4.2 Verification and validation on experimental tests

The verification of the model was carried out systematically. Excerpts of the results of the material characteristics have already been presented. By means of a convergence analysis, the accuracy of the model was proven sufficient. For the four-point bending models, an element length of 50 mm in the longitudinal direction of the column and 25 mm in the transverse direction was found adequate. For the buckling tests, the element lengths were reduced to 30 mm and to 15 mm in width and height resulting in sufficient convergence.

The simplified modeling of the welding seams as “tie”-connection implied a significant overestimation of the shear bearing capacity by a factor of four but was chosen to vastly reduce the modeling and calculation effort. In a study of detailed models with three-dimensional representation of the welds with an appropriate shear strength only a small difference of 0.3 % in ultimate load of composite columns under four-point bending as well as under buckling load could be observed. In the experimental tests, no plastic deformation of the welding seams was observed suggesting a more significant influence of the welding’s stiffness than the plastic shear capacity. To verify this simplified depiction the buckling behavior of two colinear beam elements was examined in a simplified model (Figure 4-8). The beam elements were connected by discrete springs in vertical and horizontal directions. The horizontal springs have infinitely high stiffnesses, representing hard contact. The spring stiffness of the vertically arranged springs was modified parametrically.

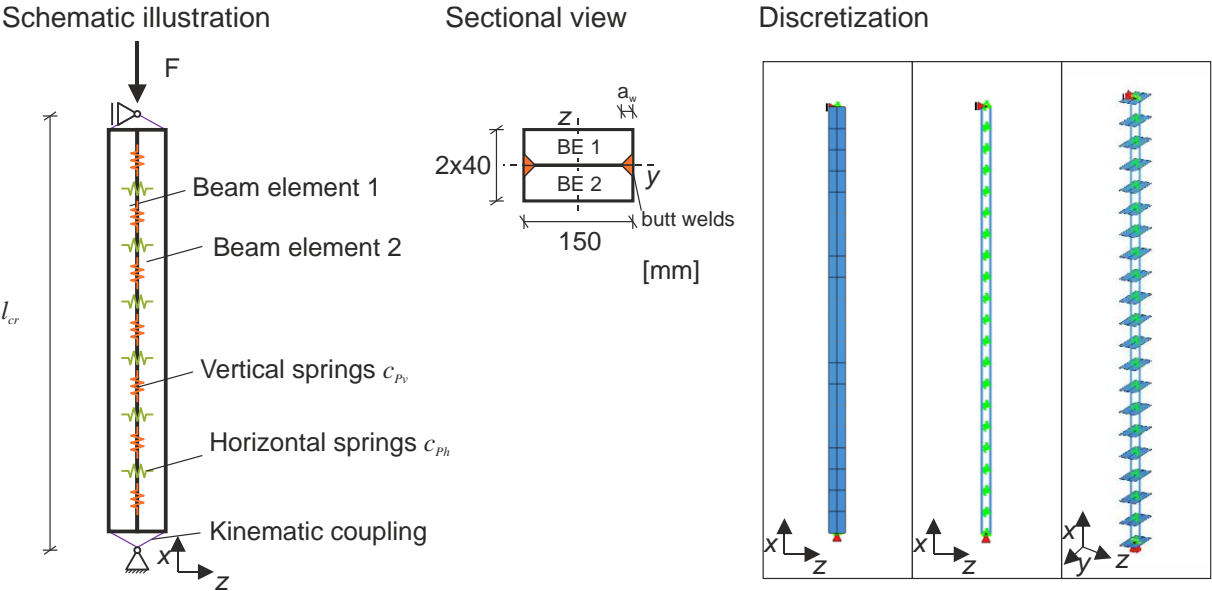


Figure 4-8 Simplified beam model in SOFiSTiK.

The buckling loads of the simplified beam model were evaluated for a parametrically increased vertical spring stiffness c_{Pv} (Figure 4-9). It became apparent that for a low spring stiffness of 1 kN/m, the buckling load met the analytical solution for 2 individual adjacent beams. With increasing stiffness, the buckling load increased and approached the buckling load of a single beam with the cross-section of twice the size asymptotically. This implied full shear connection of the individual beams. Further, it became apparent that a stiffness of 10^6 kN/m already was sufficient to yield such interaction. The shear stiffness of longitudinally loaded fillet welds amount to 5710 MPa/mm (e.g. [87]). For two butt welds with $a_w = 6$ mm, this stiffness could be

converted to a discrete spring stiffness of 6,852,000 kN/m (see ²). Thus, the stiffness of two fillet welds of such thickness would be sufficient to reach full interaction of the connected sections. In conclusion, the results of this buckling analysis verified the initial assumption to model the fillet welds using rigid solid connection.

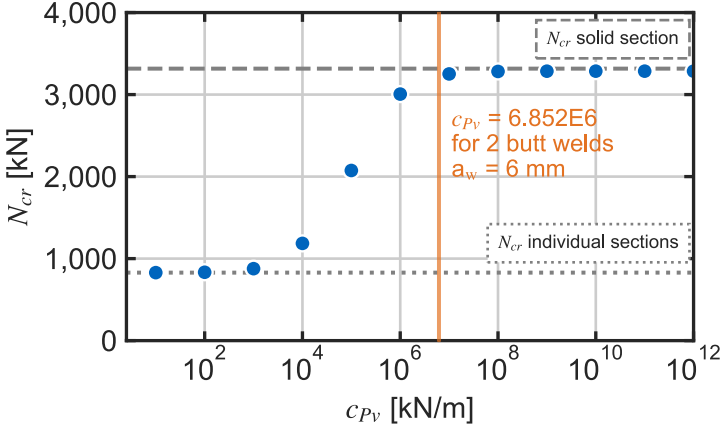


Figure 4-9 Critical buckling loads in dependence of vertical spring stiffness.

To validate the numerical modeling, the results from GMNIA are compared to the full-scale experimental tests. The four-point bending tests served as a good basis for the validation of the geometry, boundary conditions and contact conditions, since in these tests only a small influence of the eccentric core position and residual stresses on the load-deformation behavior was expected. The evaluation of the load-deformation behavior showed only small deviations for tests BR-2, BR-3, and BR-4 (Figure 4-10); test BR-1 was not considered in detail because of the interference signal in the measurement. The deviations in the load-deformation behavior can be explained by the flexibility of the experimental test setup, which could be evaded by comparing the effective flexural stiffness. The FE models and the experimental tests BR-2, BR-3 and BR-4 showed an accurate agreement (Figure 4-11) whereas the determined flexural stiffnesses were derived using different methods. For the numerical results, using Equation (3-5) yielded the most complying results, where the deformation at midspan was not influenced by any deformation of the bearings; in contrast to the experimental results, determined by the sections curvature.

² Two fillet welds with $a_w = 6 \text{ mm}$, length per beam-segment of 100 mm for each spring

$$c_{Pv} = 5710 \frac{N}{mm^3} \cdot 6 \text{ mm} \cdot 2 \cdot 100 \text{ mm} = 6,852,000 \frac{N}{mm}$$

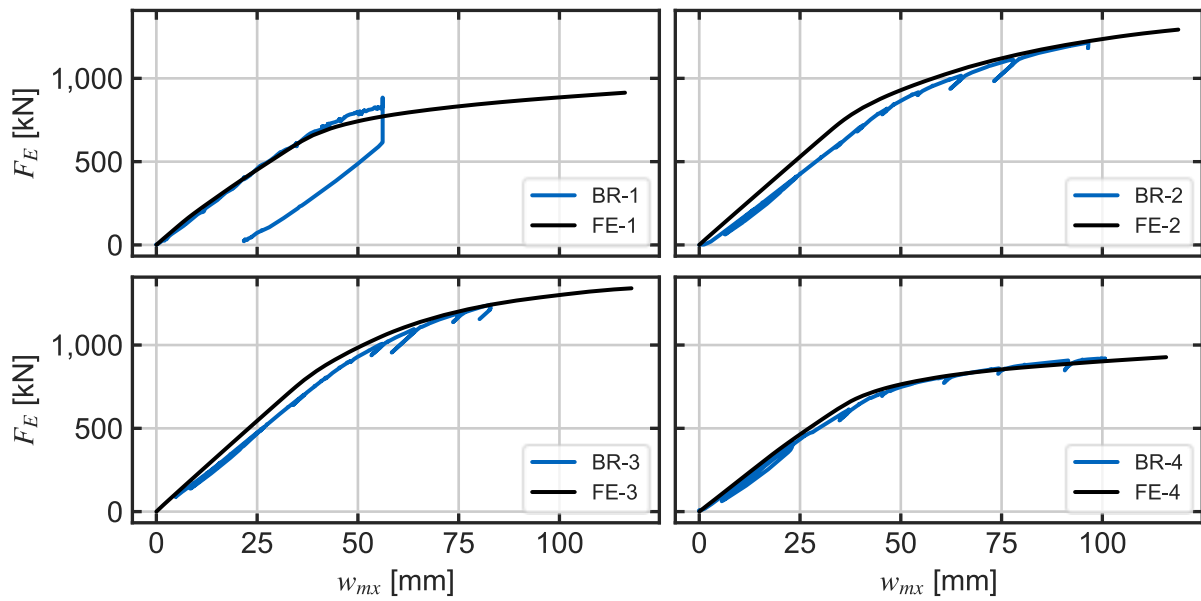


Figure 4-10 Load-deformation of FE-model and experiments under four-point-bending.

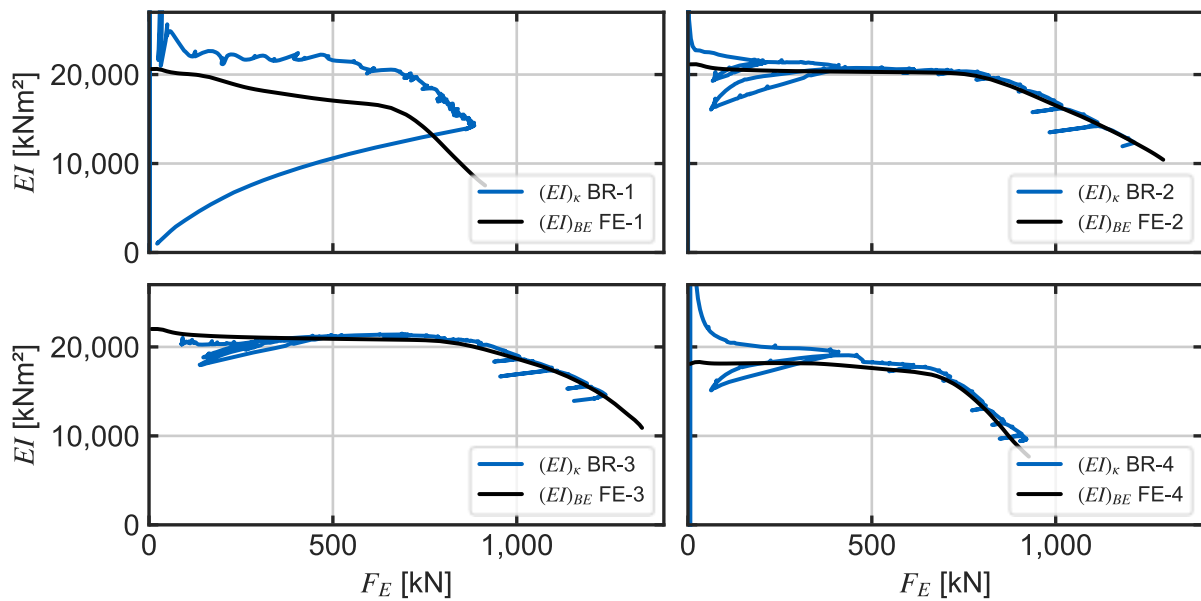


Figure 4-11 Flexural stiffness of FE-model and experiments under four-point-bending.

A comparison of the experimental buckling tests with the numerical models first showed a significant deviation in the deformation behavior and bearing loads. During the examination of the tested columns, a non-central position of the core profile was found for selected specimens. Since this was not measured for all columns, the imperfect core position had to be determined iteratively by comparing the load-deformation behavior. Core positions were varied in and against the buckling direction of up to 5 mm. Deviations due to e.g. inaccurate flame cutting were not considered. Thus, the imperfect position of the core profile e_{0k} was used as the only

variable. Ultimately, not only ultimate loads but also the load-deformation characteristics of the experimental tests could be reproduced numerically very accurately (Figure 4-12). An eccentricity of +5 mm (in the buckling direction) was found for KR-3 and -5 mm (against the buckling direction) for KR-9. As explained in Chapter 3.3, these imperfections can be considered realistic, since the distances to the cladding tube could not be achieved uniformly with the spacers used. By adjusting the core position, a maximum deviation of 3.5 % of the ultimate load from GMNIA and experiments was achieved.

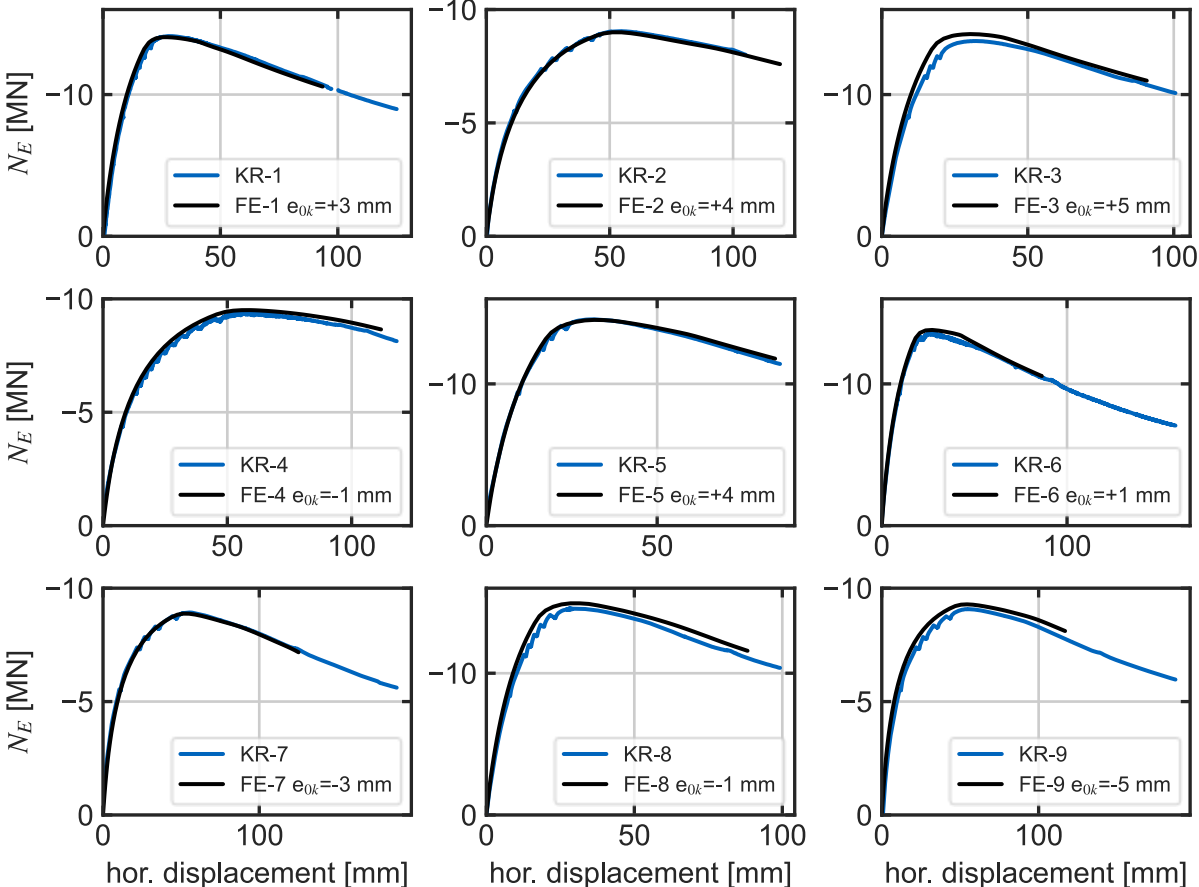


Figure 4-12 Comparison of load-deformation of numerical and experimental buckling tests.

These characteristics were also confirmed by comparing the flexural stiffnesses determined. Since the experimental values could not be unambiguously determined due to the eccentrically positioned core profiles, only a qualitative comparison of the flexural stiffnesses is possible (Figure 4-13). Matching characteristics could be seen here as well. For example, the experimental and numerical flexural stiffness of KR-3 with an eccentricity of the core $e_{0k} = 5$ mm initially increased until the ultimate load is reached, after which the flexural stiffness decreased and vice versa. Based on the comparisons between experimental and numerical results, the models can be considered validated.

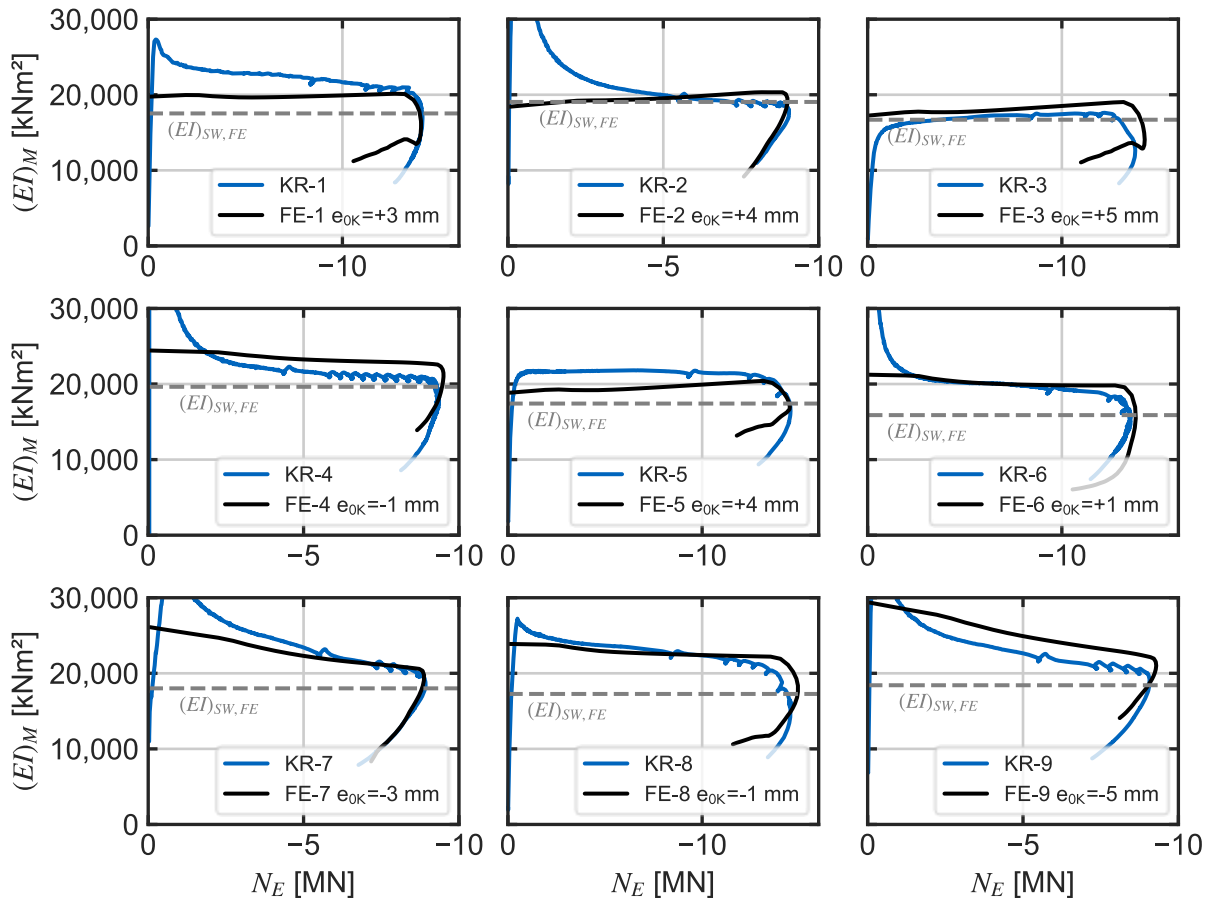


Figure 4-13 Comparison of flexural stiffness of numerical and experimental buckling tests.

4.3 Buckling behavior of high-strength flame-cut steel plates

Flame-cut steel plates of five different steel grades (S235, S355, S460, S700, S960) were investigated for their buckling behavior and the influence of the applied residual stresses. The corresponding relative slenderness were selected in four ranges ($\bar{\lambda} = 0,5; 1,0; 1,5; 2,0$) considering the yield strength σ_r accordingly. The cross-sections with width of 150 mm and thickness of 40 mm were modeled with residual stresses from flame cutting according to ECCS [18] using Equations (2-7) and (2-8). Residual stresses from the rolling process were modeled using a quadratic approach and maximum compressive stresses of -100 MPa at the edge in the thickness direction. A global bow imperfection of $L/1000$ was chosen for the pin ended specimens. Buckling failure was specified by support conditions in the respective cross-section axes. The results of the tests are shown in the European buckling curves for comparison (Figure 4-14).

In the z-direction, a strong relation between the buckling load and the steel grade was observed: with increasing steel grade, the assigned buckling curve increased. Plates from steel grade S355 presented sufficient agreement with the current classification according to prEN 1993-1-1:2020-08 [2] for the buckling curve c of rectangular cross-sections. For plates of steel grade S960, buckling curve a or a_0 appeared matching. In the region of low relative slenderness, there is only a small difference between the steel grades, so that at most buckling curve b could be assigned. For buckling in the y-direction, the effects were reversed. By increasing the yield strength, the width c of the section subjected to tensile residual stresses was reduced and the risk of buckling increased. In the low relative slenderness range, no buckling failure was achieved for normal strength steels; the ultimate loads were above the Euler hyperbola because local failure was restricted by the boundary conditions. As the relative slenderness increased, the buckling loads approached the a_0 buckling curve, but the highest steel strength achieved the lowest reduction factors χ . In summary, buckling in the z-direction could be determined to be critical when applying the shown residual stresses on flame-cut plates.

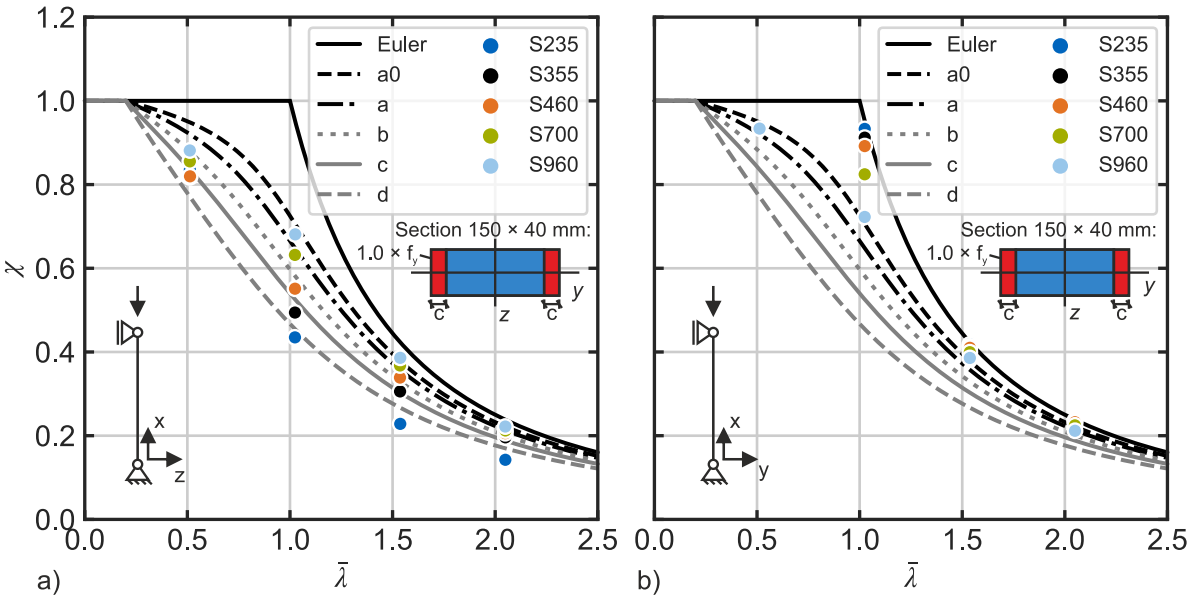


Figure 4-14 Buckling of flame-cut plates with different steel grades.

4.4 Buckling behavior of high-strength tubular sections

The tubular hollow sections were examined using the residual stress modeling approaches for cold and hot formed sections according to prEN 1993-1-14:2023 [37] (Figure 4-15). In contrast, the distribution of the residual stresses was considered with compressive stresses on the

inside of the tube and tensile stresses on the outer surface, according to e.g. Stamenkovic et al. [88]. It could be seen that regardless of the diameter and wall thickness of the hollow sections in the hot finished condition and steel grade S890, a classification in the buckling curve a_0 appeared appropriate. Cold-finished hollow sections were situated at the level of buckling curve c in the range of low relative slenderness ($\bar{\lambda} < 1,5$) and slightly below at higher relative slenderness ($\bar{\lambda} \geq 1,5$). The classification of the buckling curve a_0 for tubes of steel grade S890 complied with the provisions of prEN 1993-1-1:2020-08 [2], initially approved for steels up to grade S700. The classification of cold formed sections to buckling curve c also validated the classification of the code, regardless of the steel grade.

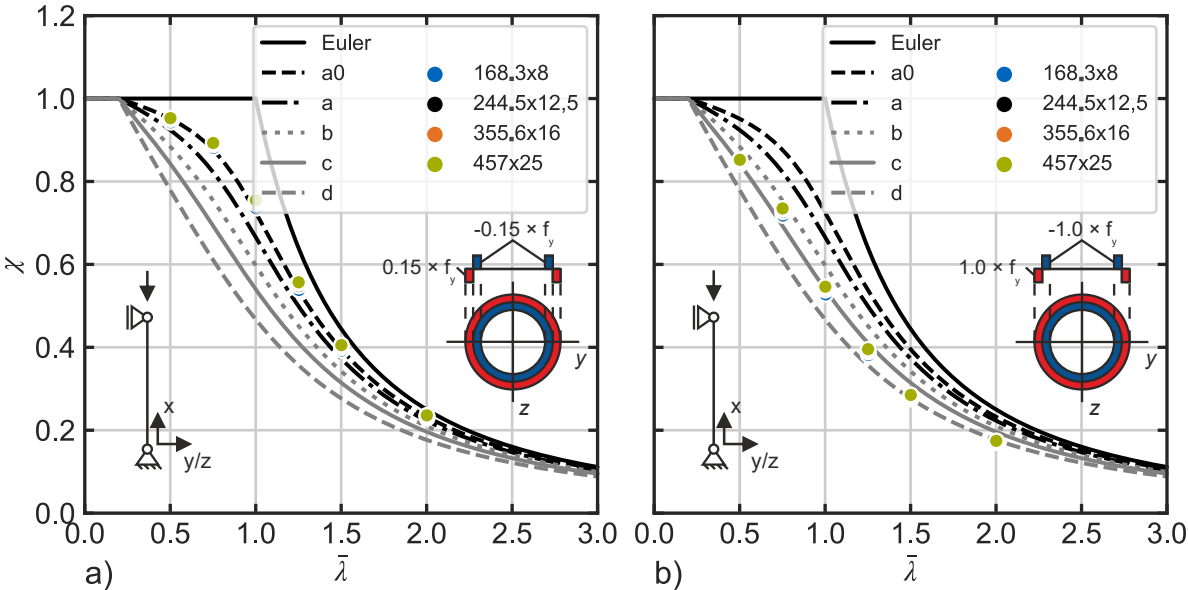


Figure 4-15 Buckling of unfilled tubular hollow sections a) hot finished and b) cold formed.

4.5 Parametric investigation

Parametric studies help to extrapolate previous findings and ensure the transferability of the results to different geometries. Therefore, four further sections with different tube diameters, combinations of HSLP, and extent of shear connection were designed in the numerical models, following previous descriptions. As bolted connections did not achieve satisfactory results and implied significant labor efforts, no further consideration of this shear connection was conducted but only welding of the laminated plates was used.

Methods

The design of the sections was similar to the previous design consisting of a tubular hollow section and a steel core of max. 40 mm plate thickness with adjusted widths in order to achieve a concrete cover of 25 mm (Table 6-10 to Table 6-14). Little research could be found on the risk of local buckling in concrete filled tubular hollow sections made of high-strength steels. In prEN 1994-1-1:2024 the yield strength is not considered for different threshold values of the ratio of diameter d to wall thickness t but $d/t \leq 90 \cdot 235/f_y$. Although Bradford et al. [89] resp. [90] developed an analytical basis for a smaller wall thickness and first experimental results suggest a more favorable threshold value for high-strength steels, only limited experimental results are known to date. Thus, the tubular hollow sections were selected for the threshold of current standards, resulting in comparably large wall thicknesses for large diameters. All parametric sections were modeled considering five different lengths (Table 6-15), resulting in relative slenderness $\bar{\lambda}$ of 0.5, 0.75, 1.0, 1.25, 1.5 and 2.0. The effective flexural stiffness for the relative slenderness was determined according to Equation (8.49) from prEN 1994-1-1:2024 [9]. Residual stresses of the steel plates were considered using the simplified method from ECCS, using Equation (2-7) and (2-8). Tubular hollow section of the deployed steel grades are currently only available in hot-finished states, so residual stresses were considered according to prEN 1993-1-14:2023 [37] with a constant stress magnitude of $0.15 \cdot f_y$ over the wall thickness. The length and positioning of welding connections between the laminated plates was varied in the investigation (see Figure 4-16) between configuration a) at the columns ends (as in experimental tests) and b) discontinuous with the total length of the weld l_w divided by the number of welds n_w .

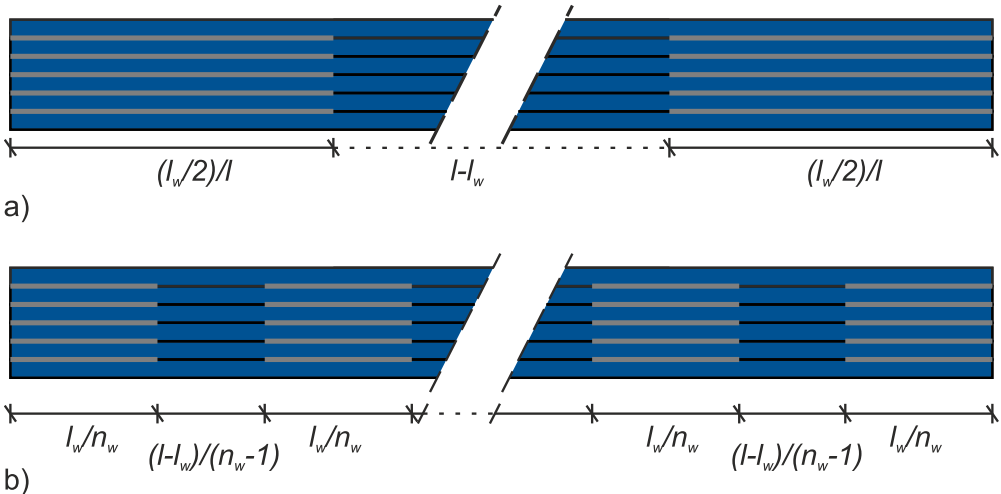


Figure 4-16 Parametric studies welding configurations.

The following hypotheses were the basis of the numerical investigation:

1. The effective flexural stiffness and thus the load bearing capacity of the composite column can be increased with the help of longer weld seams on the laminated steel plates along its lengths.
2. By dividing the weld seams into discontinuous weld seams, the flexural stiffness can be further increased with the same total weld seam length.
3. Regardless of the outer cladding tube diameter, a minimum degree of shear transfer can be achieved for the individual plates of the core section through the confinement effects and bonding from the concrete filling.

To evaluate the influence of different welding configurations between the laminated steel plates in the column's core, section cuts were used in the Finite Element Model. Using the principal of stress integration of cut finite elements, resulting internal forces could be determined for each component. Following the moment-curvature relationship the curvature κ of a plane section corresponds to the bending moment M_E divided by the flexural stiffness of the beam EI (Equation (4-3)). This can be extrapolated to the bending moment of a component by its flexural stiffness (Figure 4-17).

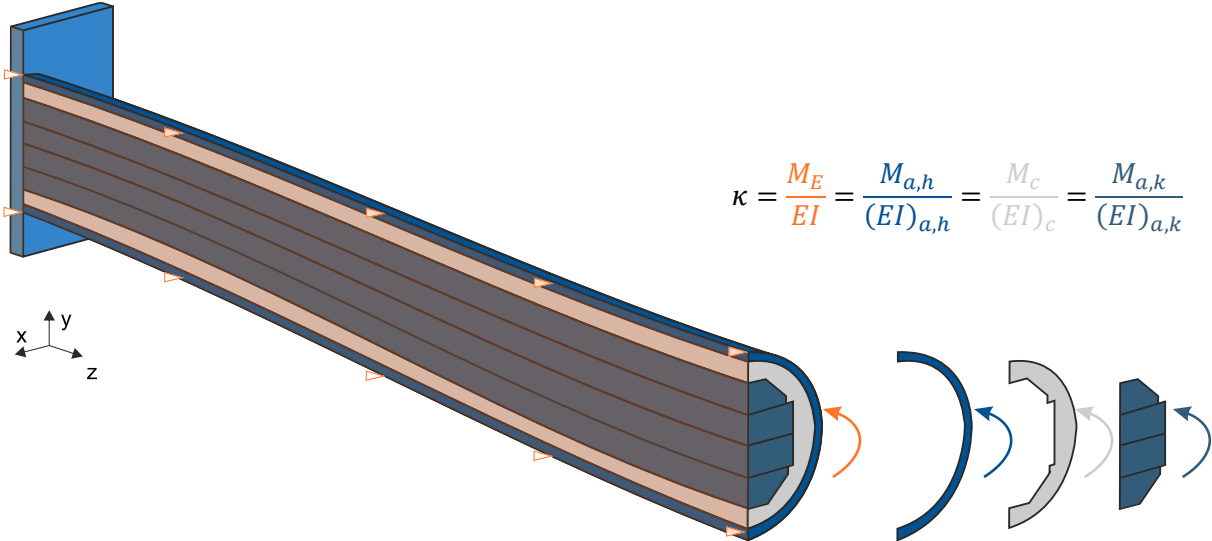


Figure 4-17 Moment-curvature relation (Index a,h: structural steel section, tube; c: concrete; a,k: structural steel section, core profile).

$$\kappa = \frac{M_E}{EI} = \frac{M_{E,i}}{(EI)_i} \quad (4-3)$$

$(EI)_i$ Flexural stiffness of the component

$M_{E,i}$ Acting bending moment of the component

The aim was to adjust the flexural stiffness of the columns with locally limited welds. Equation (4-3) can be rearranged to Equation (4-4) to investigate the achieved change in flexural stiffness of the individual components $(EI)_i$.

$$(EI)_i = M_{E,i} \cdot \frac{EI}{M_E} \quad (4-4)$$

For composed sections with individual centers of gravity not coinciding the combined center of gravity, as the laminated steel plates inside the column cross-section, the activated area moment of inertia is of interest to determine the flexural stiffness. Each area moment of inertia results from the principal moment of inertia in its center of mass (PMoI) and its Steiner terms. These were evaluated in the following as $(EI)_{a,k,St.}/(EI)_{a,k,St.,100\%}$ displaying a fraction of a solid section with full shear interaction, see Equation (4-5).

$$\frac{(EI)_{a,k,St.}}{(EI)_{a,k,St.,100\%}} = \frac{(EI)_{a,k,FEM} - (EI)_{a,k,PMoI}}{(EI)_{a,k,100\%} - (EI)_{a,k,PMoI}} \quad (4-5)$$

$(EI)_{a,k,St.}$ Flexural stiffness of activated Steiner terms of the core section

$(EI)_{a,k,St.,100\%}$ Flexural stiffness of the core section's Steiner terms at 100 % shear interaction

$(EI)_{a,k,FEM}$ Flexural stiffness of the core section from FEM

$(EI)_{a,k,Eigen}$ Flexural stiffness of the principal moments of inertia

$(EI)_{a,k,100\%}$ Flexural stiffness of the core section at 100 % shear interaction

4.5.1 Flexural stiffness of HSLP composite columns under pure bending

To determine the influence of a limited connection between the plates, the parametric cross-sections were modeled under four-point bending without normal force. For the models under four-point-bending, the axis of symmetry between the two loads and along the longitudinal direction of the column was considered. A constant distance of 1.0 m was provided between load and supports.

The comparison of the numerical results under four-point bending confirmed the anticipated relation between the length of the welding seams and the effective flexural stiffness. In Figure 4-18, the flexural stiffness of a column under four-point bending is displayed for a length of welding seams in percentage of the total length, located at the columns ends (configuration a). The effective flexural stiffness of the tubular and concrete sections seemed unaffected of the welding length of the core section. With an in total lower flexural stiffness, more plastic deformation occurred at the same level acting bending moment. Additionally, it could be observed that the concrete section exhibited significantly lower flexural stiffnesses than anticipated by prEN 1994-1-1:2024 [9] with $0.6 \cdot (EI)_c$. The flexural stiffness of the core section could significantly be increased with a higher amount of welded length. Without any shear connection between the plates, minimal flexural stiffness of the core could be achieved through friction.

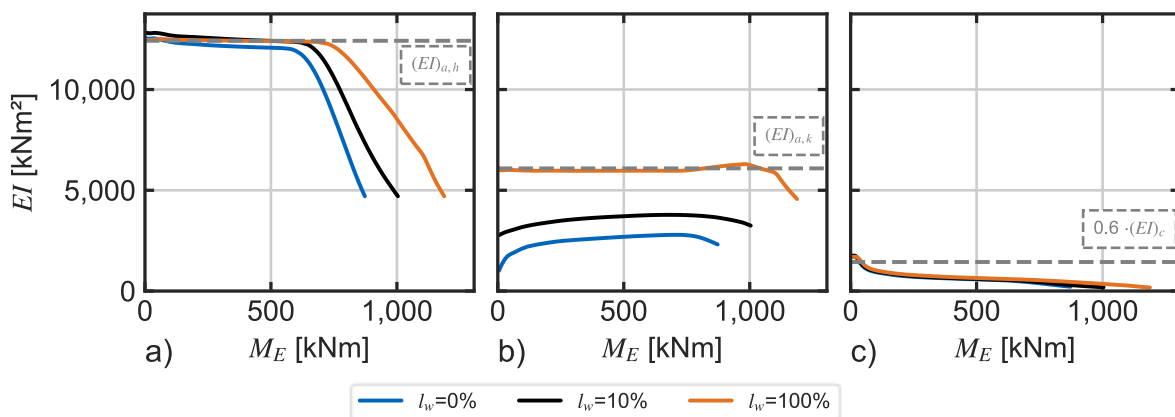


Figure 4-18 Flexural stiffness of components with different models compared to analytical flexural stiffness a) of the tube (a,h), b) core profile (a,k) and c) concrete (c) under four-point bending, welding configuration a), l_w indicated in the legend in % of total length.

This effect could be shown more thoroughly using Equation (4-5), see Figure 4-19. Displayed values above the ratio of 100 % as well as the incline of the flexural stiffness when reaching higher loads were due to the limitation of the elastic beam theory as basis for the evaluation, and numerical inaccuracies due to couplings in the model and therefore locally constrained

elements. For all specimens from QS2 to QS4, over 30 % of activated Steiner terms could be observed with no welding seam. For pure bending, the ratio of activated Steiner terms was not related to the section ratio of the core related to the total section, comparing QS2 and QS3 with equivalent core sections. The proportion of Steiner terms seemed unaffected of the ratios between core section compared to the total section, indicated by similar observations of QS2 and QS3, sections with same HSLP core in different tube diameters.

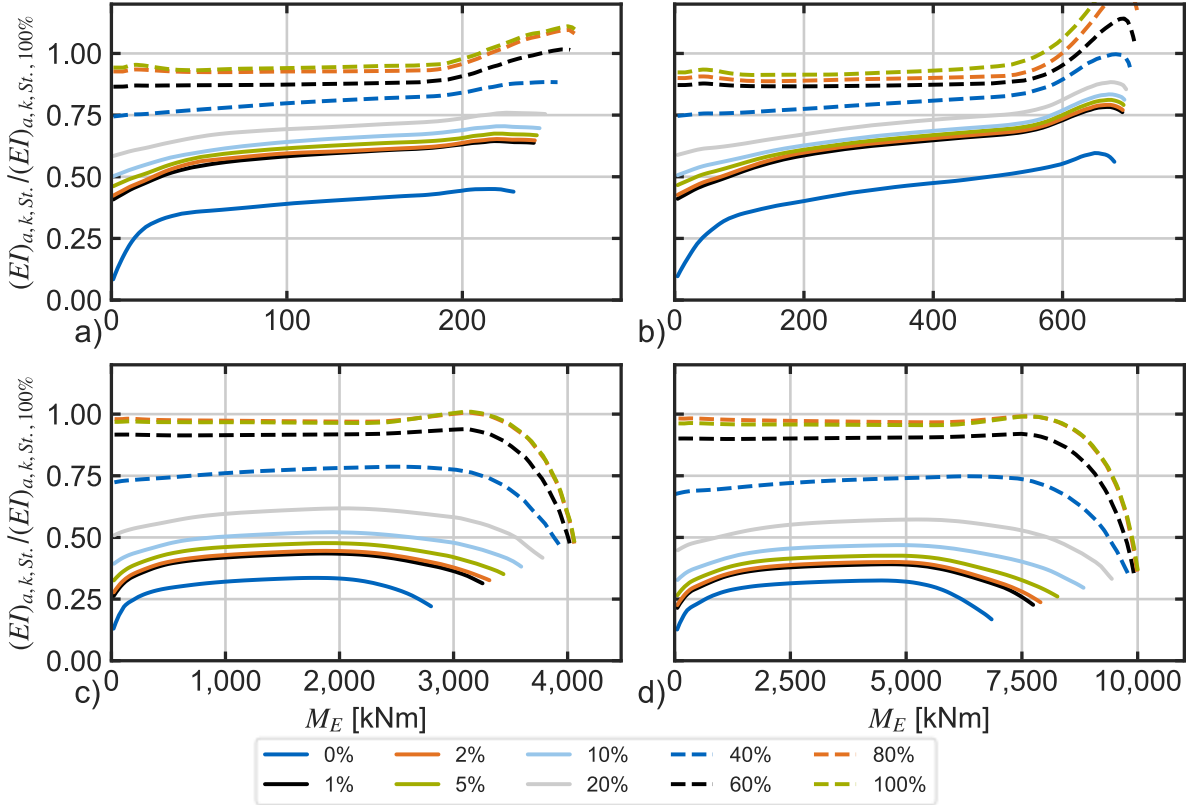


Figure 4-19 Activated Steiner terms under four-point bending with different welding lengths for a) QS2 b) QS3 c) QS4 and d) QS5; welding configuration a).

4.5.2 Flexural stiffness of HSLP composite columns under compression

The flexural stiffness of a column is dependent on the relative slenderness. This results from the phenomenon of plastic buckling. For columns of low relative slenderness, the section is dominated by high compressive loads that induce plastic utilization of the material. Consequently, these parts of the cross-sections experience a change of the elastic modulus a to tangent modulus with reduced stiffness and so little flexural resistance is expected.

This could be objectified in the evaluation of the numerical study, where the flexural stiffness of each component for QS1 was significantly reduced for relative slenderness of $\bar{\lambda} \leq 1.0$,

compared to the calculated stiffness, when reaching ultimate load (Figure 4-20). With increasing relative slenderness, effects of plastic buckling decreased and the effective flexural stiffness of the structural steel sections corresponded approximately constant values. The flexural stiffness of the core section did not reach the calculated value because of limited shear connection ($I_w = 10\%$). Due to the high-strength steel used for the columns, large plastic strains were obtained when reaching ultimate load. Thus, the concrete section experienced large strains and damage, resulting in a largely decreased flexural stiffness with only a fraction of the expected value of $0.6 \cdot (EI)_c$. With the combination of S890, and S960 for the tubular section, and the core section, respectively, the concrete flexural stiffness was obtained with only approximately 30 % of $(EI)_c$.

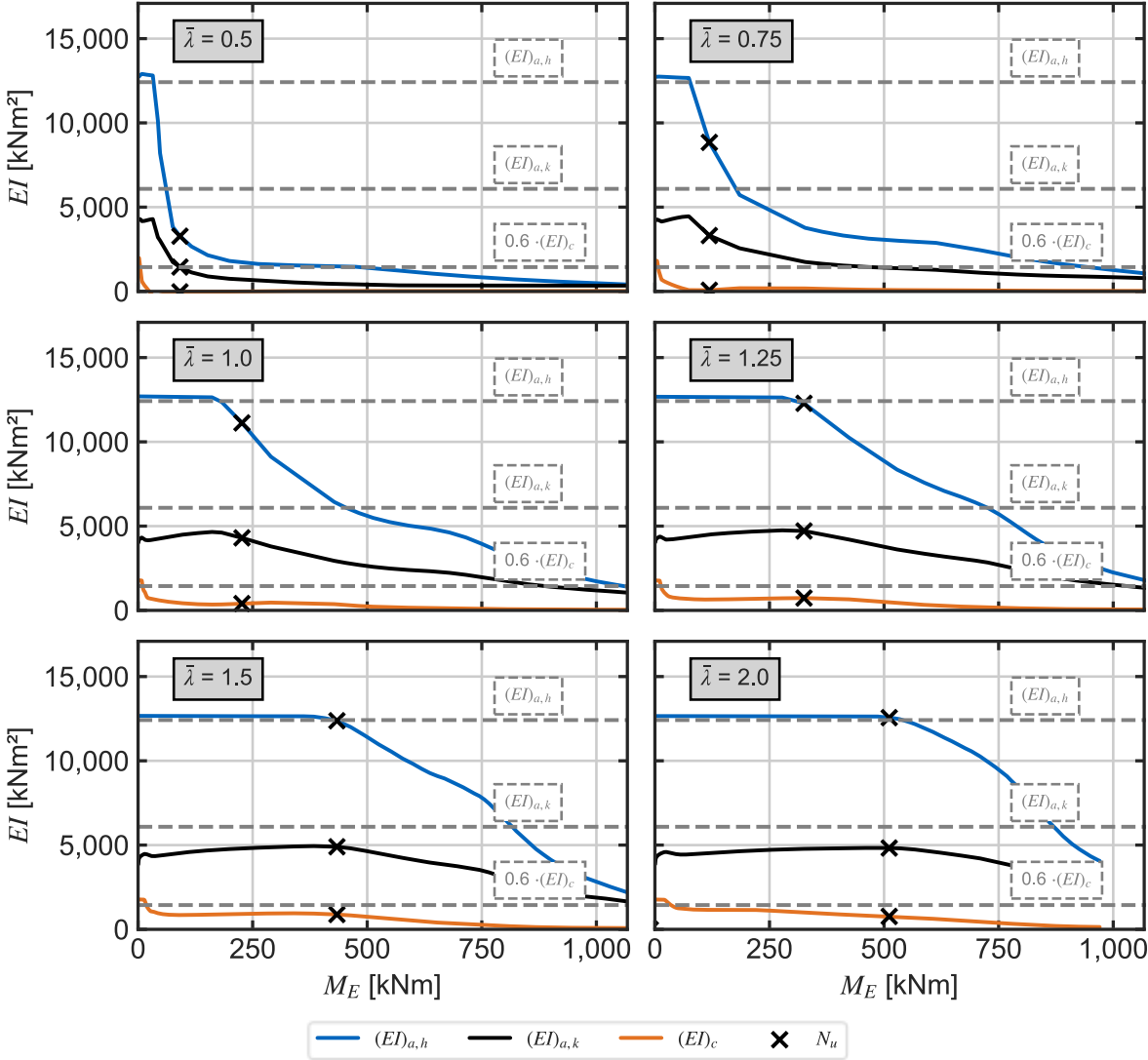


Figure 4-20 Flexural stiffness of individual section components of centrally loaded QS1 ($I_w = 10\%$).

As the flexural stiffness of axial loaded columns is dominated by effects of plastic buckling, the evaluations concerning effects of a variation of welding seams were executed for columns with a relative slenderness of $\bar{\lambda} = 2.0$.

In the parametric study, all sections were analyzed with different lengths of shear connections including 0 % to 5 %, 20 %, 60 % and 100 % of welding along the length of the core section. From the results of the parametric analysis, it could be observed that the increase of welding length for configuration a) (welding from both ends) followed a linear trend. This also meant a linear decrease in unwelded length. Furthermore, a correlation of the activated Steiner terms and the proportion of plastic resistance of the core section $N_{pl,a,k}/N_{pl,Rk}$ could be observed, comparing QS1 and QS2. Scaling the achieved activated Steiner terms with these factors, a linear trend resulted (Figure 4-21). This trend also encompassed configurations that lacked a shear connection between the laminated steel plates in the core section.

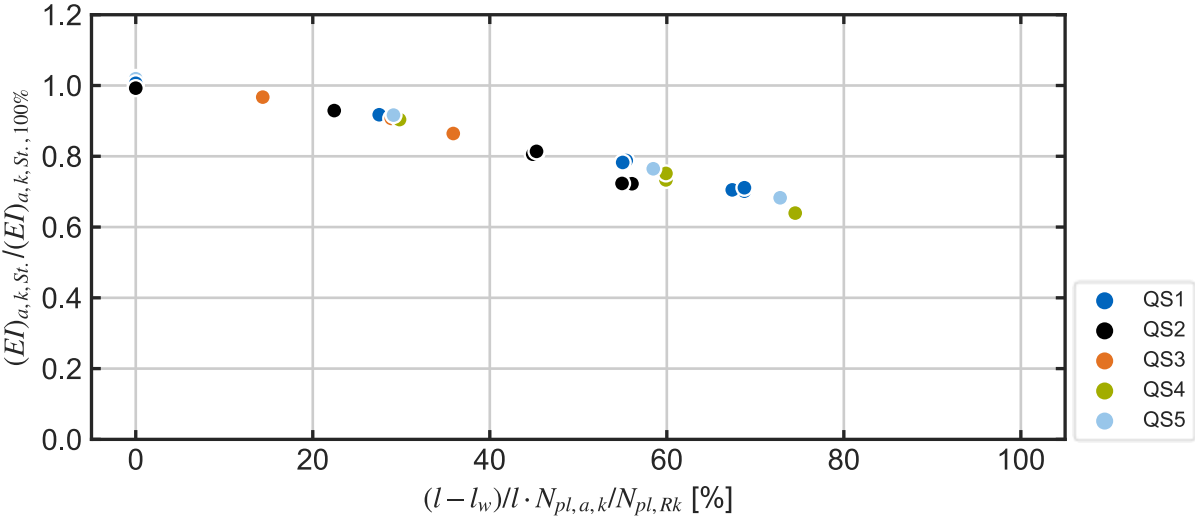


Figure 4-21 Activated Steiner terms with different welding lengths (configuration a).

The use of discontinuous welds underlined this finding: The flexural stiffness of the composite columns is dependent on the free unwelded length between the welded segments. Consequently, an increase in the number of welding seams at a constant total length of welding seam resulted in a notable enhancement of flexural stiffness. This could be seen for the specimens with increased number of discontinuous welds n_w (configuration b) to 4 and 6, with a varied length of welding from 5 % to 40 % of the total length (Figure 4-22). The results could be approximated using a linear regression ($R^2 = 0.986$).

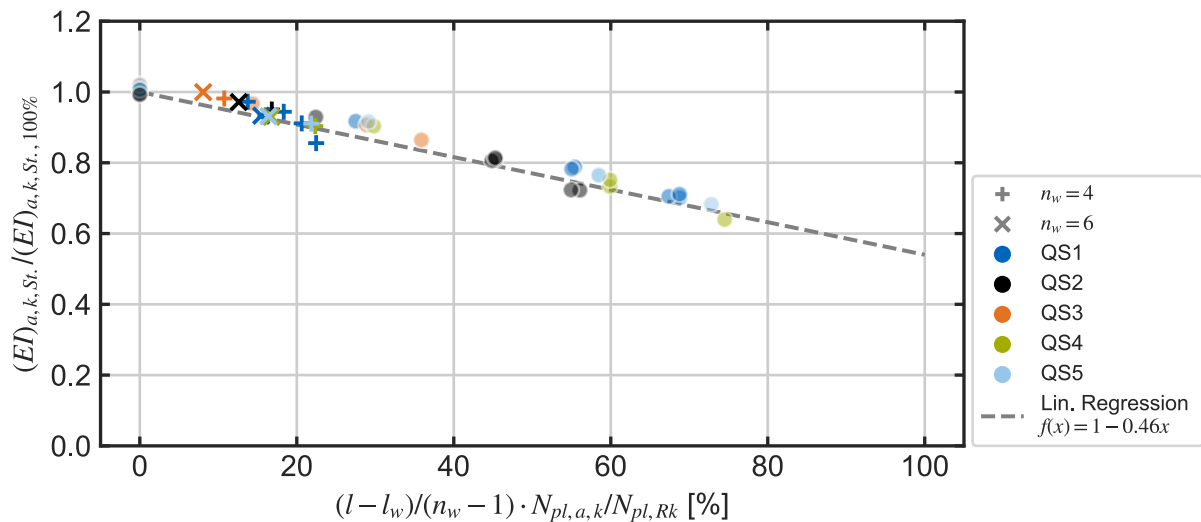


Figure 4-22 Activated Steiner terms with different welding lengths (configuration a & b).

The plastic buckling of the columns caused large compressive strains and yielding of the section. Additionally, tensile stresses from bending occurred on the direction of failure when reaching ultimate load, causing crack propagation and failure of the concrete under tension. This led to a reduced flexural stiffness in the center of the column, as proven in the experimental results (Figure 3-8). The yield strain of the tubular section and the core section were at 4.3 ‰ and 4.68 ‰, respectively, far above the strain at ultimate stress of the concrete section at 2.3 ‰. Confinement effects of the hollow section prevented spalling and a total failure of the concrete. Furthermore, the tubular section could bear large tensile strain. In consequence of the two effects, compression damage caused by large compressive strains, and failure due to tensile stresses, led to a significantly reduced flexural stiffness of the concrete section, which could be proven by the numerical results (Figure 4-23). In all investigated section designs, the concrete section had nearly no flexural resistance at low relative slenderness. The strong reduction decreased with an increase of slenderness but a mean value of $(EI)_c$ at $\bar{\lambda} = 2.0$ amounted to 0.3, strongly deviating from the anticipated ratio of 0.6.

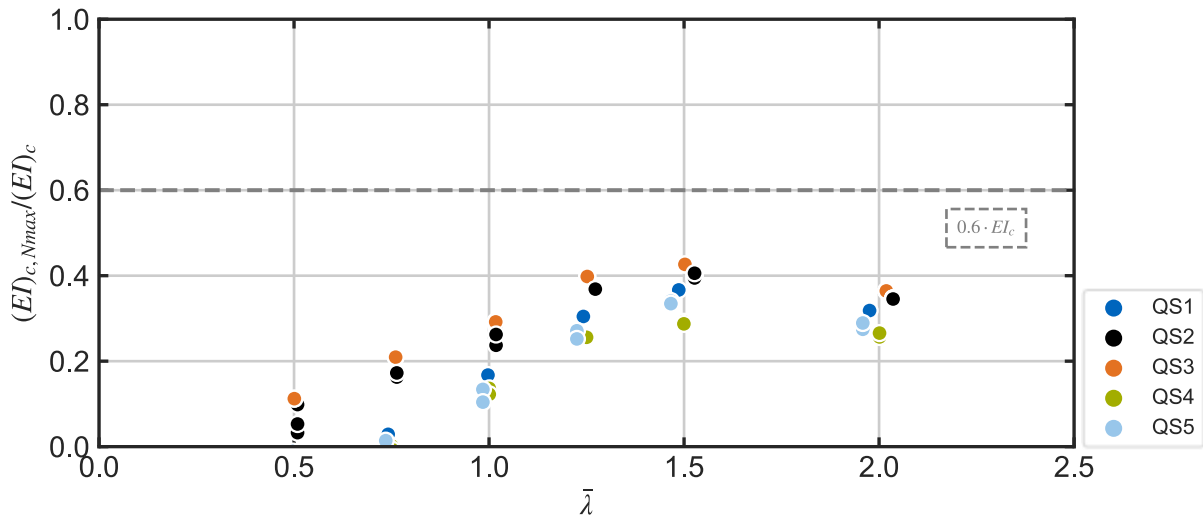


Figure 4-23 Effective flexural stiffness of the concrete section.

4.5.3 Comparison of HSLP composite columns under bending and under compression

When comparing the effective flexural stiffnesses of axial loaded pin ended columns with columns under pure bending, a significant difference could be observed (Figure 4-24). For columns with limited welding ($I_w = 10\%$), the flexural stiffness under axial load was significantly higher than under pure bending for the same welding length, approximately at values for a fully welded section with $I_w = 100\%$. For columns with a relative slenderness of $\bar{\lambda} = 2.0$ the flexural stiffness was higher than under pure bending, presumably effected by lateral strains and confining effects. For shorter columns, effects of plastic buckling dominated the failure mode, so the determined flexural stiffness at ultimate load was far below the values obtained from columns under pure bending.

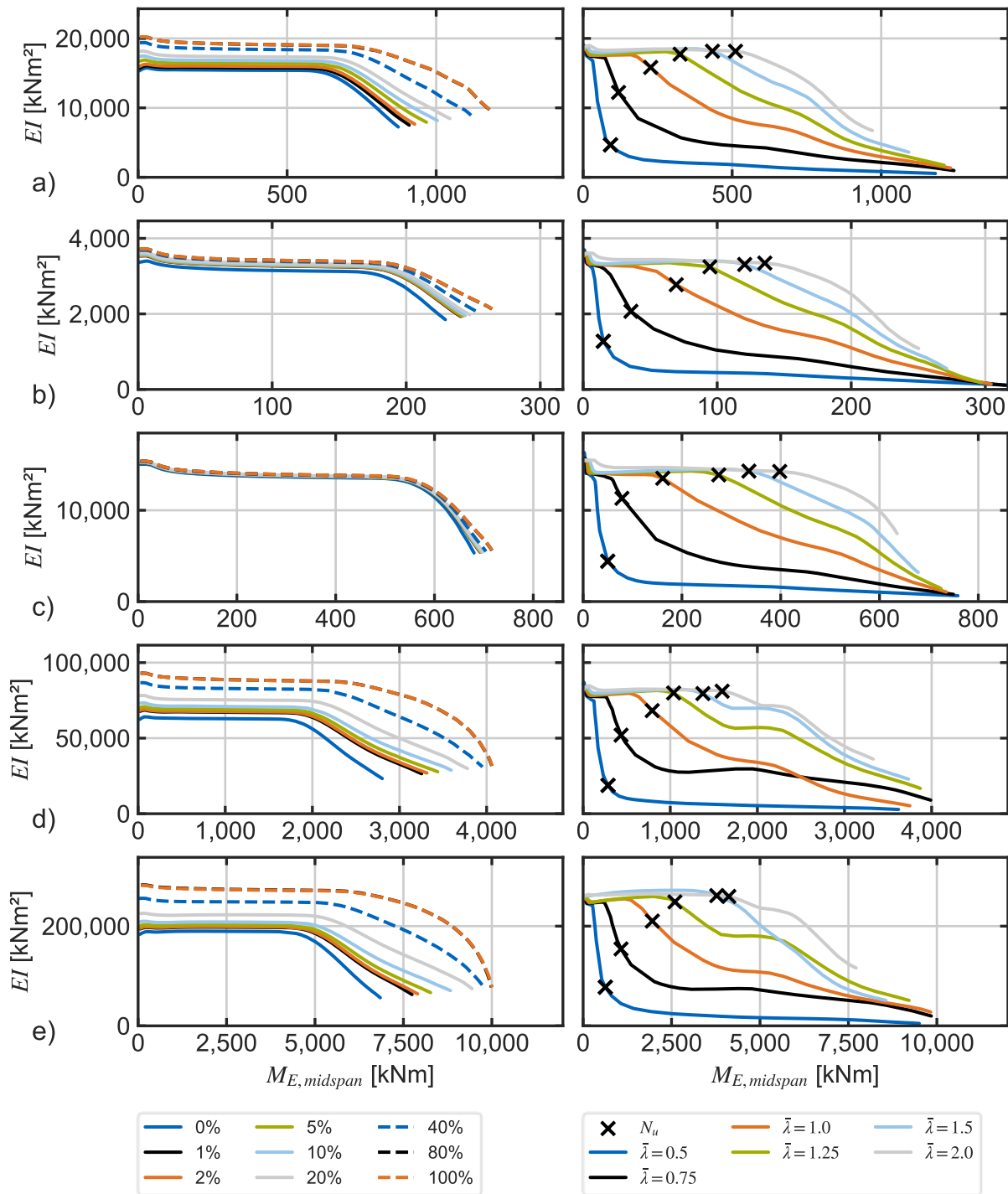


Figure 4-24 Flexural stiffness under pure bending (left) and various weld length and centric axial load (right) with $l_w = 10\% l$ for a) QS1, b) QS2, c) QS3, d) QS4, e) QS5; welding configuration a).

4.5.4 Eccentrically loaded HSLP composite columns under compression

In the experimental tests it became apparent that the position of the core profile in the tubular hollow section is subjected to plural imperfections of the individual component. Eccentric positions are possible and must be considered. These geometric imperfections also lead to eccentric loading of the column, as other influences from erection and tolerances can induce. The aim of the investigation was to verify if a design for analysis second-order theory might be possible. Current design methods for bearing load of composite columns consider strain-based interaction of axial load and bending moment.

For instance, results of bending moment and normal load interaction of eccentrically loaded columns with parametric section QS1 (considering welding configuration a) with 20 % welded length) under uniaxial bending and compression with varying relative slenderness are displayed (Figure 4-25). Different amounts of bending action were achieved with a variance of eccentricity of the compressive load. The column interaction curves were derived using the full plastic interaction as well as a strain limited design method. Current design methods respected the ultimate compressive strain of the concrete which is an accurate display for the failure criterion of e.g. fully encased sections. Failure is determined from spalling and breaking away of the concrete. When the concrete is confined by a cladding steel tube, those failure modes can be excluded. Thus, the yield strain of the tube was considered as the limiting strain for these studies.

It became apparent that the axial load-moment interaction was highly dependent on the slenderness of the columns. Low relative slenderness achieved results close to the plastic interaction curve. With increasing relative slenderness, ultimate loads appeared closer to the strain limited interaction curve, as elastic buckling, and effects of local yielding of the section increased.

As anticipated, confinement effects of the tubular hollow section prevent spalling and a total failure of the concrete, and the limiting design criterion of ultimate concrete strain is not applicable. Large differences in ultimate strains of high-strength steel and normal-strength concrete amplify the contrasting configuration. Design methods based on strain limited interaction will lead to conservative and therefore uneconomic results. Design methods must be developed to account for the strong dependency of axial load-moment interaction of a column and the columns slenderness. Further derivation of equivalent geometric imperfections for capacity designs using second-order analysis lack a definition of limiting bending moment.

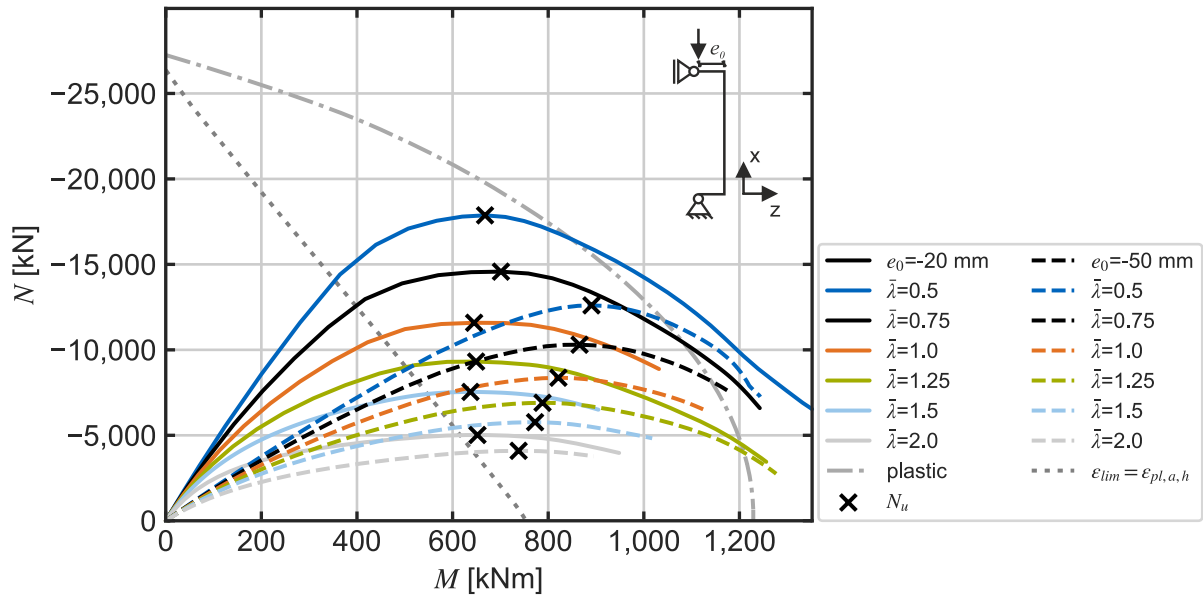


Figure 4-25 Column interaction diagram of section QS1.

4.6 Comparison of the numerical results to the European buckling curves

Extensive experimental and numerical research was undertaken, evaluating the load-bearing behavior of a newly developed section for composite columns with high-strength steels. Results have shown that a limited shear connection between the laminated steel plates with locally limited welding seams has a significant influence on load-bearing behavior.

The effects of the shear connection were evaluated in detail. Based on the results, a regularization could be derived, modifying the flexural stiffness according to the targeted deployment of shear connection. The length of unwelded regions $l_{unwelded}$ was the decisive factor for the effective flexural stiffness of these columns, combined with the ratio of plastic normal force capacity of the core $N_{pl,a,k}$ compared to the total normal force capacity of the section $N_{pl,Rk}$. The interaction of the individual plates, names as factor α , considering the degree of activated Steiner terms, could be linearized (Equation (4-6)).

$$\alpha = 1 - 0.46 \cdot \left(\frac{l_{unwelded}}{l} \cdot \frac{N_{pl,a,k}}{N_{pl,Rk}} \right) \quad (4-6)$$

The flexural stiffness of the concrete section appeared reduced and could be addressed accordingly. By these means, a modified approach of the effective flexural stiffness $(EI)_{eff,mod}$ was developed (Equation (4-7)):

$$(EI)_{eff,mod} = (EI)_{a,t} + (EI)_{a,k,Eigen} + \alpha \cdot (EI)_{a,k,Steiner} + 0.3 \cdot (EI)_c \quad (4-7)$$

$(EI)_{a,t}$ Flexural stiffness of the tubular hollow section

$(EI)_{a,k,Eigen}$ Flexural stiffness of the principal moments of inertia of the core section

$(EI)_{a,k,Steiner}$ Flexural stiffness of the Steiner terms of the core section

$(EI)_c$ Flexural stiffness of the concrete section

Considering the modification of the flexural stiffness provided by the code, a design using the concept of European buckling curves (bc) appears possible. To prove the concept of the modified approach and the use of buckling curves, the ultimate loads of the parametric study were plotted in the buckling curves. Results were compared to the approach of $(EI)_{eff}$ from

Equation (8.49) of prEN 1994-1-1:2024 [9] and to the modified flexural stiffness $(EI)_{eff,mod}$, as shown in Figure 4-26. In the initial approach, a vertical scattering became apparent with no definitive assignment to a buckling curve. Considering the limited shear connection of the core section in the modified calculation of the effective flexural stiffness, the relative slenderness was adjusted. Consequently, the results showed a lower scattering, following the shape of buckling curves. Visually, an assignment to buckling curve a_0 became apparent. Only for columns with a low relative slenderness $\bar{\lambda}_{mod}$ up to 0.75, the modification showed little influence, and the vertical alignment still was present.

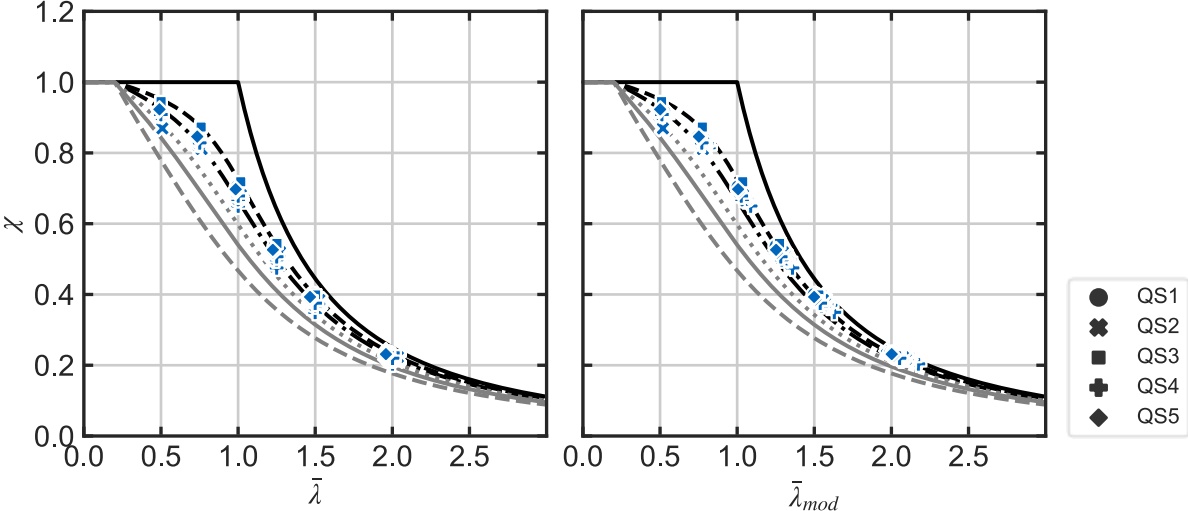


Figure 4-26 Numerical results in the European buckling curves.

The agreement of the numerical results with buckling curve a_0 could be assessed with a comparison of the numerical result N_{FE} and the theoretical resistance (Figure 4-27). This consisted of the reduction factor χ from the buckling curve and the characteristic value of the plastic resistance to compression $N_{pl,Rk}$, for which the concrete section α_{cc} was accounted with 1.0. High conformity of numerical results and the buckling curve result in a value of 1.0; values below implicate non-sufficient conformity with the buckling curve. The distribution of the results considering the unmodified definition of the flexural stiffness followed the observation from Figure 4-26: a vertical scattering was present with results mostly lower than 1.0. The results for the effective flexural stiffness from EC 4-1-1 yielded a mean value of 0.9574 (Table 4-2). Thus, the assignment of the buckling curve might be in question. Through the proposed modification of the flexural stiffness an alternated distribution could be seen with less scattering. For a relative slenderness above $\bar{\lambda}_{mod} = 1.0$, values resulted around and above 1.0. A mean value of 0.9979 could be observed, supporting the assignment to bc a_0 . Consequently, the modification resulted in an increase of the standard deviation and variance

for all sections from 0.030 to 0.036, and 0.0009 to 0.0013, respectively. The individual sections yielded sufficient conformity, especially valid for QS3 (Table 4-2). The mean values of all sections could be improved.

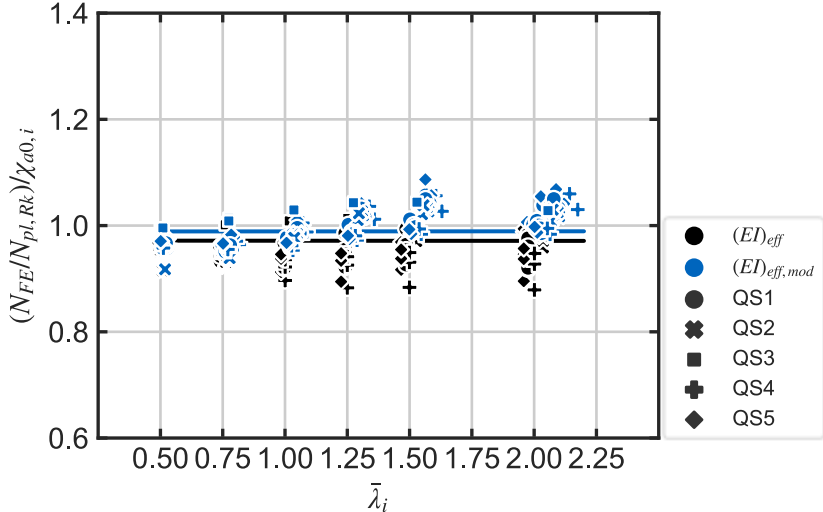


Figure 4-27 Numerical results compared to bc a_0 .

Table 4-2 FEM results compared to buckling curve a_0 .

$\frac{N_{FEM}}{\chi_{a0} \cdot N_{pl,Rk}}$	$(EI)_{eff}$			$(EI)_{eff,mod}$		
	Mean value \bar{x}	Stand. Dev. σ	Variance σ^2	Mean value \bar{x}	Stand. Dev. σ	Variance σ^2
QS1	0.957	0.014	0.0002	0.993	0.029	0.0008
QS2	0.962	0.029	0.0009	0.987	0.044	0.0020
QS3	1.002	0.008	0.0001	1.025	0.017	0.0002
QS4	0.943	0.015	0.0002	0.985	0.031	0.0010
QS5	0.957	0.017	0.0003	0.997	0.038	0.0015

The effects of the modification could further be examined plotting the individual factors of the modification on the x-axis (Figure 4-28). Trends are expressed in inclined lines in the plot, a horizontal distribution indicates an effective adjustment and is aimed for. Both considered modifications yielded a favorable distribution of the numerical results as linear regression lines changed from inclined slope to a nearly horizontal shape.

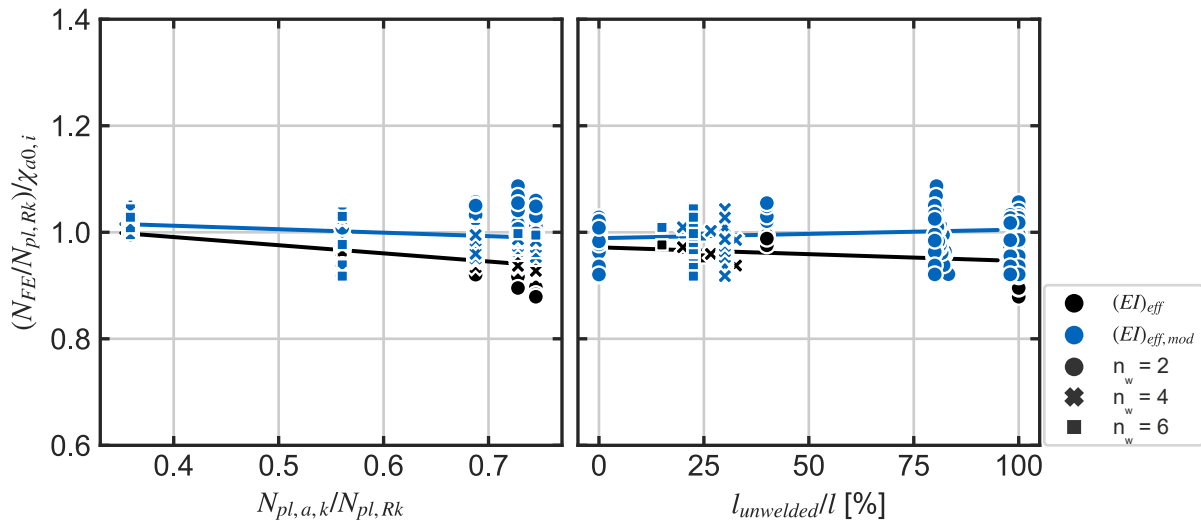


Figure 4-28 Trends of the key parameters considering $(EI)_{eff,mod}$, compared to bc a_0 .

Prior examination and the comparison with European buckling curves showed proof for the concept of a modified flexural stiffness and consequently a modified relative slenderness. The experimental buckling tests have shown a significant influence of geometric imperfection of the core section; as the manufacturing of the specimens was at industry standards, a future manufacturing of columns without any deviations appears impossible. Thus, imperfections must be considered in the design process. The imperfections were subjected to scattering with maximum values of 5 mm of core eccentricity being determined for the experimental specimens.

In order to quantify the influence of possible manufacturing tolerances, the parametric models were adapted with an eccentric position of the core into the same direction as the bow imperfection to amplify both effects. The obtained value for the core eccentricity e_{0k} of 5 mm from the experimental tests was equivalent to 1/50 of the tube diameter. Thus, this practical value was adapted for the parametric sections. The shear configuration was regarded as configuration a) (see Figure 4-16) with a total length of welding of 20 % along the core length, measured from the column ends.

The effect of the applied eccentricity e_{0k} deviated for the individual specimens (Figure 4-29). For QS3, containing the smallest ratio of core profile compared to the rest of the section, an eccentricity of the core profile had the least effect. For the other sections, approximately similar effects could be observed. The previously described deviations for columns with lower slenderness versus columns with larger slenderness could also be seen. Results for the test series QS1 to QS5 (except for QS3) reached to bc c and increased with the relative slenderness up to bc a_0 for slenderness of 2.0. Visually, the effect of the modified flexural

stiffness could again be confirmed, as the vertical scattering of the results obtained by the flexural stiffness from EC 4-1-1 changed to a more fitting distribution along the buckling curve.

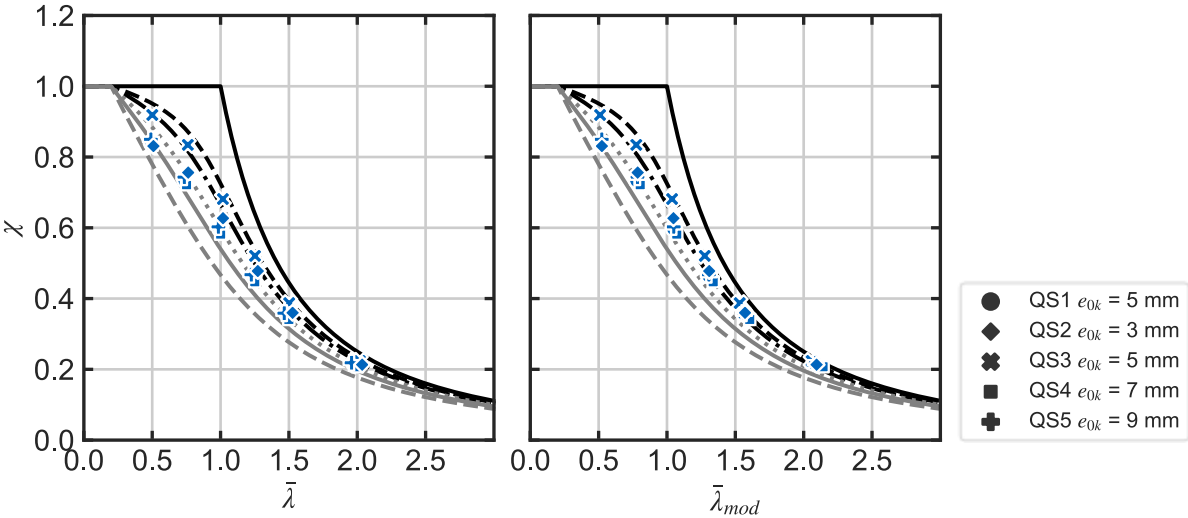


Figure 4-29 Numerical results with eccentric HSLP core in European buckling curves.

Again, the agreement of numerical results with the buckling curves was investigated. Therefore, the deviation of all numerical results N_{FEM} to the respective buckling curves was calculated (Figure 4-30). Mean values (indicated by horizontal lines) for the studied columns were below 1.0 for buckling curve a_0 , but above for the comparison with buckling curve a . Without a modification of the effective flexural stiffness, mean values were only above 1.0 for buckling curve b . As all values yielded results above 1.0 for bc c , this curve seemed too conservative. However, the scattering of each individual section became obvious as the section QS3 which seemed least affected might have positively influenced the overall mean value. Therefore, the individual mean values separated by each section were determined. The positive influence on the mean value of QS3 became apparent regarding the mean deviations (Table 4-3). For other sections the mean value was above 1.0 for bc b . Buckling curves c and d yielded mean values of above 1.0 indicating a too conservative assignment.

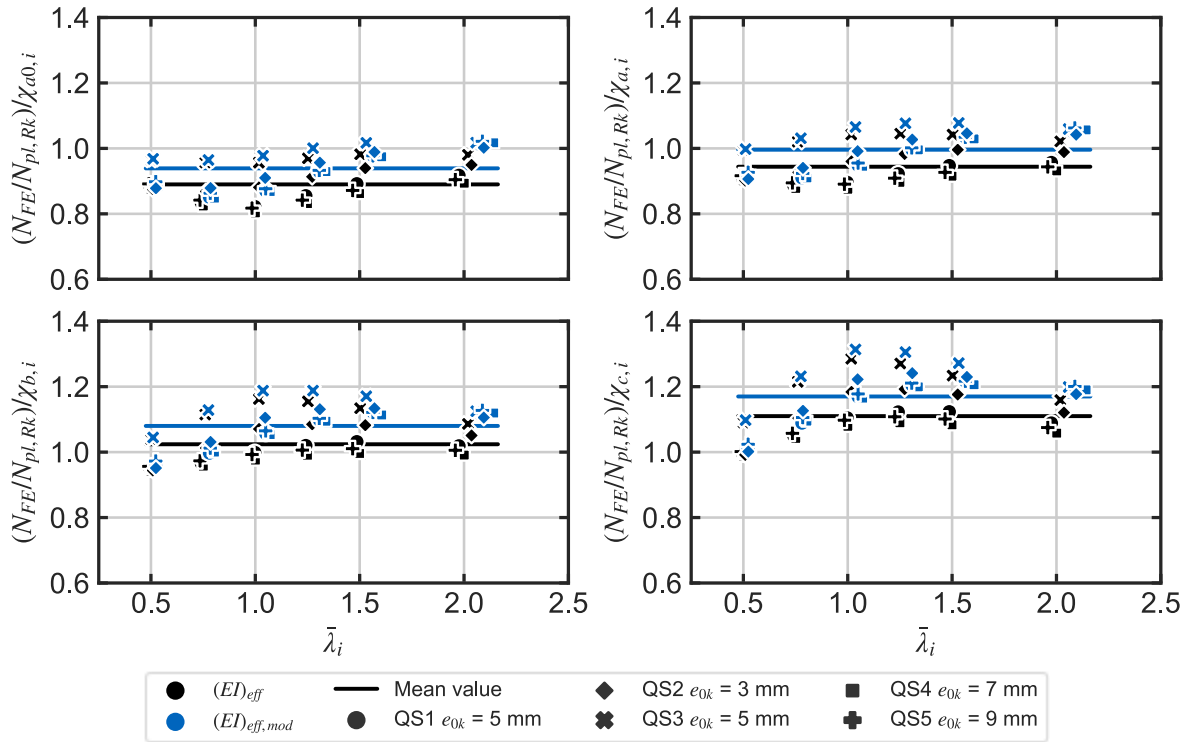


Figure 4-30 Comparison of eccentric HSLP with different buckling curves.

Table 4-3 FEM results with eccentric HSLP compared to buckling curves considering $(EI)_{eff,mod}$.

Buckling curve	a_0	a	Mean values		
			b	c	d
QS1	0.921	0.976	1.059	1.147	1.296
QS2	0.936	0.992	1.076	1.166	1.318
QS3	0.991	1.051	1.141	1.237	1.398
QS4	0.920	0.975	1.057	1.145	1.293
QS5	0.928	0.984	1.067	1.156	1.306

4.7 Discussion of the numerical results

The analysis of numerical models of the columns provided conclusive insights into the structural behavior of HSLP composite columns and presented the deciding influences on the load-bearing behavior of such columns. Results from experimental tests could be complemented with the numerical investigations including research of detailed phenomena. The extension enabled to consolidate the understanding and generalize the findings. Three-dimensional non-linear finite element models were developed, verified, and validated based on large scale and miniature material test results. Major finding of the validation process was the presence of geometric imperfections in the experimental buckling specimens of up to ± 5 mm that were determined subsequently. Specimens subjected to pure bending showed a behavior significantly more resistant to geometric imperfection and provided a useful extension for the validation of boundary conditions. The analysis of flexural stiffness showed higher resistance for columns under compression and bending than under pure bending. However, the columns flexural stiffness proved to be highly dependent on the relative slenderness.

The validated models were used in parametric studies to extend the empirical database by simulated test results. The models further helped investigating individual effects of the column components. The influence of the shear connection between individual plates of the HSLP core was presented in detail. Two key parameters of the flexural stiffness could be determined: The length of the unconnected plate segments had significant impact on the effective flexural rigidity implying the use of discontinuous welds with major benefits. Next, the ratio of plastic normal force capacity of the core profile compared to the total section defined the load ratio of the core and thus its influence on the total flexural stiffness. Due to large compressive strains in the high-strength steel section, the concrete section presented a significantly reduced flexural stiffness. A modification of the effective flexural stiffness considering these findings was derived. The comparison of the results to the European buckling curves considering a modified relative slenderness showed a proof of concept and suggested a sufficient agreement with buckling curve a_0 for all specimens. In regions of low relative slenderness, larger deviations from the buckling curves were experienced. The modification of the effective flexural stiffness did not affect the results compared to the current design approach by EC 4-1-1.

Geometric imperfections as consequences of construction tolerances were determined for the experimental buckling tests and appeared inevitable for such composite columns. Thus, non-centric positions of the core profile were implemented in numerical models with adapted dimension from the practical experience. The results suggested an adjustment to buckling curve a , although a scattering could be observed for the 30 models considered.

The proposed modification of the flexural stiffness for the design of HSLP composite columns based on European buckling curves showed targeted adjustment and a higher agreement with the buckling curves compared to prior methods. The investigations of the influencing parameters (Figure 4-28) showed that the dependencies were recorded almost free of trends, when considering this modification. Thus, the concept of modifying the effective flexural stiffness for slender columns was confirmed. Overall, the columns could be assigned to buckling curves based on the characteristic results. Buckling curve a_0 could be confirmed for perfectly fabricated columns, with a mean value of 0.998. As fabrication imperfections in form of an eccentric core position were found inevitable in the experimental testing, this was considered in the same direction of geometric bow-imperfection. Consequently, the assigned buckling curve needed to be reduced to buckling curve a with a mean value of 0.99, considering all investigated columns. Section QS3 with a proportion of the flexural stiffness of the core section of only 0.04 showed less influence of the imperfection and could be assigned to buckling curve a_0 , despite the eccentric core positions. The numerical models used to evaluate the results were based on several conservative assumptions: The modulus of elasticity of the steel sections were found to be below the presumed values of 210 GPa in miniature tensile tests and have been addressed accordingly. Also, the concrete strength was considered with a reduced strength regarding the findings from experimental tests. Further, only the nominal yield strength of the steel section was considered, representing the minimum strength for plates up to 50 mm according to EN 10025-6:2019 [91]. The eccentric position of the core profile was chosen as a deterministic maximum threshold of $D/50$ for each section, resulting from experimental experiences.

Regarding the scatter of the results, higher deviations were observed for columns of low relative slenderness. The consideration of a modified flexural stiffness did not achieve any effect compared to the current EC 4-1-1 method, mainly due to the overall greatly reduced flexural stiffness due to the high axial load. Values resulted lower than anticipated by the buckling curve. As the comparison was based on characteristic values, the development of safety factor must be considered for the design. Until now EC 3-1-1 and EC 4-1-1 consider a partial factor for resistance of members to instability assessed by member checks of steel and steel concrete composite sections with γ_{M1} . For the German Annex of EC 3-1-1 [92], the value of γ_{M1} is 1.1. Following the concept of EN 1990, the safety factors of a design concept γ_M is composed by factor for uncertainty of material properties γ_m and a factor for the modeling uncertainty of γ_{Rd} . No information is known about the composition of the components of the current factor. The underestimation of the results at low slenderness is a common phenomenon for steel and steel-concrete composite columns and is included in the application of a general safety factor. The evaluation of a safety factor for the proposed column sections

could be executed by a concept for statistical determination of resistance models of EN 1990 [93] Annex D, supported by experimental tests. To date, the variability of material properties is defined for steel sections $>S460$ in EC 3-1-1, even though the general scope of the code is permitted for steel grades only up to S700. For the steel grades S890 and S960 used in this study, the variability of their properties must be assumed to comply with current guidelines. Further, the development of a safety factor should account for a variance of geometric imperfection in the form of a core eccentricity in both positive and negative directions. This manufacturing tolerance was found to be unavoidable in the experimental tests under normal industry manufacturing standards. However, it has not been investigated in previous research and therefore no empirical data or statistically derived assumptions are known to date. In addition, the number of models investigated, 20 per section, is insufficient for a statistically reliable evaluation and needs to be expanded. For statistic evaluations a minimum of 200 results is recommended (e.g. [94]). Given these limitations, a statistical determination of the model uncertainty factor did not seem possible to date and precludes further evaluations after EN 1990.

Overall, the individual influences on the load-bearing behavior vary greatly over the course of the buckling curve. For columns of low slenderness, the scatter of three factors is particularly important due to the dominant effects of the stress problem: the yield strength, the residual stress state and the cross-sectional area. In the transition area of medium slenderness, the influence of the scattering values of geometric imperfections, moment of inertia and modulus of elasticity of the materials increases and dominates the load-bearing behavior of columns with high relative slenderness. Consequently, a consideration of the model and material uncertainty as a function of these variables would provide the highest precision but has not yet been considered in this way.

In conclusion, the results showed a sufficient agreement with the assigned buckling curves. The concept of a modified effective slenderness was confirmed. Due to the lack of further knowledge, the application of current partial safety factors seems valid to consider the uncertainty of the results. Additionally, conservative assumptions were made for the finite element models. The conformity with all values resulting on the safe side is shown in Figure 4-31, for columns without a geometric core imperfection compared to bc a_0 and columns with eccentric core profiles compared to bc a . The lower values of columns with low slenderness appeared tolerable in the background of the low scattering and level of uncertainty of the dominating parameters for the load-bearing behavior. In case of additional knowledge about the material behavior of high strength steel grades over S700 or an extensive empirical

knowledge about the occurrence of manufacturing imperfections, a re-evaluation of the results is recommended.

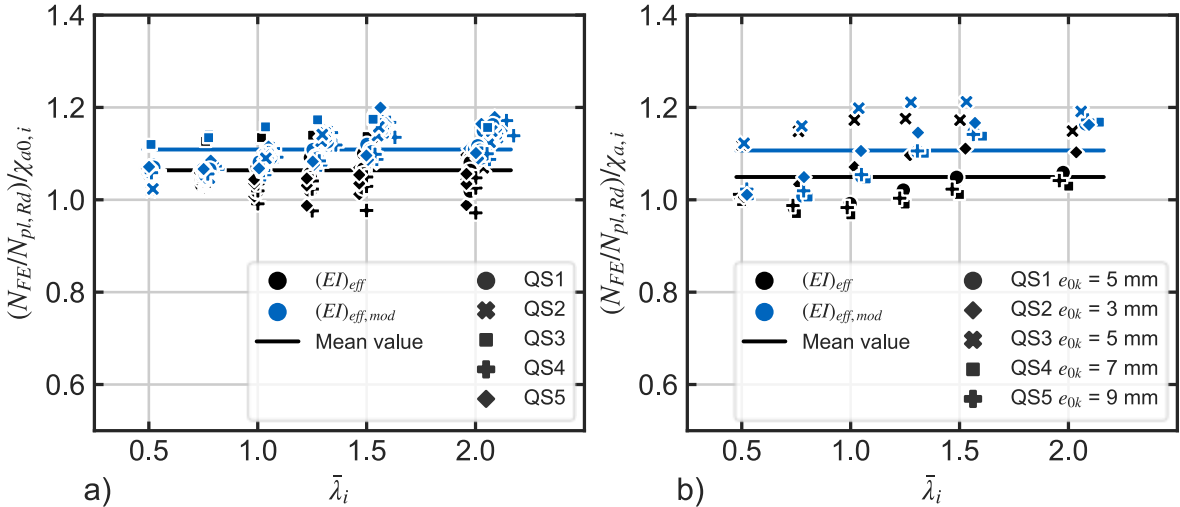


Figure 4-31 Comparison of the results for a) perfect columns and b) with core eccentricity on design level.

5 Conclusion

Composite columns are a high-strength and fire-safe alternative to concrete or steel columns in situations of high vertical loads. Their resistance is mainly determined by the section design and the material properties of its components. With high-strength steels as driving innovation in modern structural steel and bridge engineering, they also play an important role in advancing composite columns. The improved resistance not only allow for significant material savings and more space saving, but the efficient structures might result in cost-effective designs.

In the present work, a new type of section for steel-concrete composite columns was developed, consisting of laminated high-strength steel plates in a high-strength hollow section filled with normal-strength concrete. The use of individual laminated high-strength steel plates as the core profile not only allows a largely increased load-bearing capacity. Compared to conventional solid sections, the homogeneous distribution of yield strength and low residual stresses are important advantages. The availability of high-strength steel products is still limited and mainly restricted to small dimensions. Therefore, design flexibility is provided by the laminated steel plates as large cross-sections can be assembled freely. Further benefits are achieved regarding the production effort and limitation of structural imperfections with a customized lamination of the plates with locally concentrated welds, adjusted to the required resistance.

Given the limited experimental data available on the distribution of residual stresses in high-strength steel plates, the aim was to quantify this phenomenon of structural imperfections. The investigation revealed a high concentration of tensile residual stresses at the edges of the flame cut and a low level of compressive residual stresses in the center of the cross-section, which were in equilibrium. This distribution was found to be consistent with previous approaches in the literature.

Another objective of the research was to investigate the effect of optimized production with locally limited weld seams on the flexural stiffness of the composite column. It was shown that the length of the unwelded area of the laminated plates was a pivotal factor. The arrangement of the connections in equidistant sections to reduce the free length had a significant influence on the flexural stiffness. The increase of local stiffness by placing welds between the individual plate cross-sections of the core profile was dominated by the elastic stiffness of the welds, the plastic shear strength showed little impact. The use of high-strength steels resulted in increased stress on the confining concrete, which led to a further reduction of its stiffness. The previous determination of flexural stiffness according to EC 4-1-1 could be adapted with a modification so that a design using European buckling curves appeared possible. Even though

the investigated sections should be considered as steel columns, regarding the factor δ of above 0.9, the characteristics of this type of column are only achievable with a confining concrete.

A significant impact of geometric imperfections was found in the experimental tests. The individual components of the assembled columns, such as hollow sections and steel plates, had their own manufacturing tolerances in terms of plate thickness, precision of the flame-cutting, ovality, and more. Further tolerances for cutting and the assembly were additional variables and led to a non-centric position of the profile for all columns. As these tolerances appeared inevitable, the imperfections and their scattering should be considered in the design. So far, no statistical evaluation of such imperfection was evaluated but must be developed in agreement with the partial safety concept of EC 0. In the presented numerical models, an eccentricity of $D/50$ was estimated as deterministic upper threshold from practical experience. The value can be discussed with regard to quality control measures and visual inspection possibilities and should therefore further be investigated.

Geometric equivalent imperfections for design according to second-order analysis could not be determined for the innovative columns. Previous principles of design with regard to limiting the maximum cross-sectional strains to the ultimate compressive strain of the concrete proved to be uneconomical. The hollow section prevents complete failure of the concrete and enables larger plastic strain capacities. The need for further research on concrete-filled hollow section composite columns with high-strength steels was pointed out.

The column type shown enables the production of new high performance composite columns with a highly flexible cross-section. Field of beneficial application of such columns are in areas of low relative slenderness so the load-bearing capacity and the number of floors to be built on them could be significantly increased with simultaneous small cross-sectional dimensions, compared to common solutions. The increase in relative slenderness due to the high-strength steel reduces the load-increasing effects, but the results presented suggest an assignment to improved buckling curves and therefore increased resistances.

The investigations carried out represent only an excerpt of a new type of column cross-section: due to the flexible design of the cross-section geometry and the composition of the components, only a limited number of the infinitely possible geometries were investigated experimentally and numerically. The eccentric position of the core profile could only be determined by recalculating the experimental tests. A systematic decomposition of future test specimens is recommended to quantify imperfect positions. The parameter range of the experimental results were complemented by numerical results.

A comparison of the results with the European buckling curves showed a good agreement with the buckling curve a_0 for centrally positioned core profiles based on characteristic values. Considering the conservative imperfections as eccentric core profile position, the buckling curve a appeared adequate. For the comparison at the design level, the application of the partial factor for resistance of members to instability assessed by member checks of steel γ_{M1} with 1.1 from the German Annex of EC 3-1-1 gave consistent results on the safe side. In conclusion, the presented concept of a modified calculation of the flexural stiffness appeared applicable and the use of buckling curve a can be recommended for the design of HSLP-CFST composite columns. If the centric position of the core profile can be ensured by constructive measures, the buckling curve a_0 can be recommended for the design.

Nevertheless, the results can be discussed. The development of a safety factor for the design concept according to EC 0 could not be derived due to the lack of statistically analyzed assumptions about manufacturing imperfections as core eccentricity. In addition, current standards do not include partial factors for an assumed uncertainty of material properties for high-strength steel grades $> S700$. Further research is needed to address these limitations and the procedure should be re-evaluated based on the results. Additional numerical calculations should be performed to increase the number of results. However, the conservative assumptions considered in the numerical modeling compensated for the impractical statistical evaluation.

Three specific phenomena discovered during the investigations require further research. Columns with low relative slenderness scattered largely from otherwise assigned buckling curves leading to higher deviations of conformity. The calculation of the relative slenderness could further be modified accounting for the initial relative slenderness leading to an iterative calculation. The eccentric position of the core section appeared of significant influence on the ultimate loads and should consequently be accounted for. Possible methods consist of the use of an equivalent eccentric load by calculating the shift of the center of gravity considering the material stiffness for a design for second-order analysis or the development of new buckling curves with eccentricities [41]. For the design for second-order analysis, incompatibilities of the ultimate strains of high-strength steels (approx. 4.5 ‰) and normal-strength concrete (approx. 3.5 ‰) in CFST composite columns became obvious and prior assumptions of strain limited designs were not applicable. Profound studies of this interaction must be conducted.

Overall, this study provided useful insights for applications of high-strength steels in the fast-growing field of composite columns. The presented results show possibilities for an optimized design and promise structural benefits of novel composite structures.

List of Tables

Table 3-1 Experimental test program of the buckling tests.	36
Table 3-2 Ultimate loads of the buckling tests.	41
Table 3-3 Results of Southwell's method.	44
Table 3-4 Experimental testing program under four-point bending.....	49
Table 4-1 Input parameters for the CDP module.	74
Table 4-2 FEM results compared to buckling curve a_0	97
Table 4-3 FEM results with eccentric HSLP compared to buckling curves considering $E_{eff, mod}$	100
Table 6-1 Strain recording sectioning of specimen 1-1.	131
Table 6-2 Strain recording sectioning of specimen 1-2.	131
Table 6-3 Strain recording sectioning of specimen 2-1.	132
Table 6-4 Strain recording sectioning of segment 2-2.....	132
Table 6-5 Strain recording sectioning of segment 3-1.....	133
Table 6-6 Strain recording sectioning of segment 3-2.....	134
Table 6-7 Residual stress measurement X-ray diffraction in depth on bottom part.	135
Table 6-8 Residual stress measurement X-ray diffraction in depth on top part.	135
Table 6-9 Residual stress measurement X-ray diffraction on waterjet cut surface.	136
Table 6-10 Dimensions of section 1.....	136
Table 6-11 Dimensions of section 2.....	137
Table 6-12 Dimensions of section 3.....	137
Table 6-13 Dimensions of section 4.....	137
Table 6-14 Dimensions of section 5.....	138
Table 6-15 Lengths of the parametric columns in cm.	138

Table of Figures

Figure 1-1 Fire safe iron column of Peter Wight from 1857, from [1].	17
Figure 1-2 Development of yield strengths of high-strength constructional steels	19
Figure 2-1 Stiffness reduction induced by local yielding during buckling failure acc. to [11].	23
Figure 2-2 Simulation results of fully cooled steel plate (values in ksi) from [55].	30
Figure 2-3 Residual stress distribution of steel plates	31
Figure 2-4 Residual stresses of two-sided flame-cut plates from [18].	33
Figure 3-1 Sections of specimens for large scale tests [63].	34
Figure 3-2 Schematic display of the construction process [63].	35
Figure 3-3 Experimental setup a) and failed test specimen in testing facility b) [63].	38
Figure 3-4 Experimental procedure acc. to prEN 1994-1-1:2024 Annex B.	39
Figure 3-5 Definition of axes of the test specimens in buckling tests.	40
Figure 3-6 Displacement in buckling direction of the buckling tests [63].	41
Figure 3-7 Displacement perpendicular to buckling direction of the buckling tests [63].	41
Figure 3-8 Flexural stiffness on upper, lower and mid measurement level	42
Figure 3-9 Calculated experimental flexural stiffness under applied load	43
Figure 3-10 Southwell-Method on experimental buckling tests	44
Figure 3-11 Strain distribution of buckling tests with yielded zones over the section height.	46
Figure 3-12 Relative displacement of the core profile	47
Figure 3-13 Rupture of the filled welding seam of endplate and hollow section (KR-6).	47
Figure 3-14 Concrete section after testing	48
Figure 3-15 Concrete section in the compressive zone (top) and tensile zone (bottom)	48
Figure 3-16 Four-point bending test setup	50
Figure 3-17 Load displacement behavior at midspan under four-point bending.	52
Figure 3-18 Relative displacement of individual plates in the core section	53
Figure 3-19 Experimental flexural stiffness over acting moment	54
Figure 3-20 Comparison of the experimental flexural stiffness	54
Figure 3-21 Strain distribution under four-point load, load steps in kNm.	56

Figure 3-22 Bow imperfection of the specimens before test.	58
Figure 3-23 Radial imperfection of hot rolled tubular sections on three levels.....	59
Figure 3-24 Non-centric position of the core profile of tested specimen KR-3.....	60
Figure 3-25 Test specimens for the sectioning method with prepared holes.....	61
Figure 3-26 Deformeter MGM 250.....	62
Figure 3-27 a) Strain measurement with deformeter b) sawing of the segments and c) water jet cutting of the segments.....	63
Figure 3-28 Longitudinal residual stresses from the sectioning method.....	65
Figure 3-29 Longitudinal residual stresses from X-Ray diffraction	66
Figure 3-30 Longitudinal residual stresses from X-Ray diffraction	66
Figure 4-1 Boundary conditions of the Abaqus buckling model.....	72
Figure 4-2 Boundary conditions of the parametric Abaqus buckling model.....	72
Figure 4-3 Boundary conditions of the Abaqus model under four-point bending	73
Figure 4-4 Compressive behavior of concrete with CDP acc. to [80].	74
Figure 4-5 Tensile behavior of concrete acc. to [62].	74
Figure 4-6 Material behavior of the steel sections for recalculation.....	75
Figure 4-7 Bilinear material behavior of the steel section for parametric studies.	75
Figure 4-8 Simplified beam model in SOFiSTiK.....	76
Figure 4-9 Critical buckling loads in dependance of vertical spring stiffness.	77
Figure 4-10 Load-deformation of FE-model and experiments under four-point-bending.	78
Figure 4-11 Flexural stiffness of FE-model and experiments under four-point-bending.....	78
Figure 4-12 Comparison of load-deformation of numerical and experimental buckling tests.	79
Figure 4-13 Comparison of flexural stiffness of numerical and experimental buckling tests. .	80
Figure 4-14 Buckling of flame-cut plates with different steel grades.....	81
Figure 4-15 Buckling of unfilled tubular hollow sections.....	82
Figure 4-16 Parametric studies welding configurations.....	83
Figure 4-17 Moment-curvature relation.....	84
Figure 4-18 Flexural stiffness of components	86

Figure 4-19 Activated Steiner terms under four-point bending	87
Figure 4-20 Flexural stiffness of individual section components of centrally loaded QS1 ($I_w = 10\%$)	88
Figure 4-21 Activated Steiner terms with different welding lengths (configuration a).....	89
Figure 4-22 Activated Steiner terms with different welding lengths (configuration a & b).	90
Figure 4-23 Effective flexural stiffness of the concrete section.....	91
Figure 4-24 Flexural stiffness under pure bending (left) and various weld length and centric axial load (right).....	92
Figure 4-25 Column interaction diagram of section QS1.....	94
Figure 4-26 Numerical results in the European buckling curves.	96
Figure 4-27 Numerical results compared to bc a_0	97
Figure 4-28 Trends of the key parameters considering $EI_{eff, mod}$, compared to bc a_0	98
Figure 4-29 Numerical results with eccentric HSLP core in European buckling curves.	99
Figure 4-30 Comparison of eccentric HSLP with different buckling curves.	100
Figure 4-31 Comparison of the results for a) perfect columns and b) with core eccentricity on design level.	104
Figure 6-1 Recordings of experimental buckling test KR-1.	122
Figure 6-2 Recordings of experimental buckling test KR-2.	123
Figure 6-3 Recordings of experimental buckling test KR-3.	124
Figure 6-4 Recordings of experimental buckling test KR-4.	125
Figure 6-5 Recordings of experimental buckling test KR-5.	126
Figure 6-6 Recordings of experimental buckling test KR-6.	127
Figure 6-7 Recordings of experimental buckling test KR-7.	128
Figure 6-8 Recordings of experimental buckling test KR-8.	129
Figure 6-9 Recordings of experimental buckling test KR-9.	130

Literature

- [1] Peter B. Wight, "Fire-proofing Department: Details of fire-proof construction with burned clay," *The BrickBuilder*, no. 7, pp. 173–175, 1897.
- [2] *prEN 1993-1-1:2020-08, Eurocode 3 – Design of steel structures – Part 1-1: General rules and rules for buildings*, CEN.
- [3] K. Roik and P. Schaumann, "Tragverhalten von Vollprofilstützen Fließgrenzenverteilung an Vollprofilquerschnitten," 1980.
- [4] M. Chanou, *Zum Tragverhalten von Hohlprofil-Verbundstützen mit Mehrkernquerschnitten*, 2018.
- [5] M. Mensinger, R. Röß, J. Zehfuß, and S. Ameri, "Stabbündelstützen mit hochfester Bewehrung," Lehrstuhl für Metallbau, Technische Universität München, 2022.
- [6] N. Sauerborn, "Verbundstützen im Hochhausbau," *Bautechnik*, vol. 83, no. 4, pp. 284–287, 2006, doi: 10.1002/bate.200690045.
- [7] H. Pasternak, H.-U. Hoch, and D. Füg, *Stahltragwerke im Industriebau*. Berlin: Ernst, 2010.
- [8] H. Ban, G. Shi, Y. Shi, and M. A. Bradford, "Experimental investigation of the overall buckling behaviour of 960MPa high strength steel columns," *Journal of Constructional Steel Research*, vol. 88, pp. 256–266, 2013, doi: 10.1016/j.jcsr.2013.05.015.
- [9] *prEN 1994-1-1:2024, Eurocode 4 – Design of composite steel and concrete structures – Part 1-1: General rules and rules for buildings*.
- [10] M. Schäfers, S. Ameri, M. Mensinger, and J. Zehfuß, "Blechlamellenstützen aus hochfesten Stählen für den Hochbau; Schlussbericht zum IGF Vorhaben 21366 N,"
- [11] C. F. Kollbrunner and M. Meister, *Knicken: Theorie und Berechnung von Knickstäben, Knickvorschriften*. Berlin, Heidelberg, s.l.: Springer Berlin Heidelberg, 1955.
- [12] F. Engesser, "Ueber die Knickfestigkeit gerader Stäbe," *Zeitschrift des Architekten- und Ingenieur-Vereins zu Hannover*, vol. 35, 1889.
- [13] L. Tetmajer, *Die Gesetze der Knickung und zusammengesetzten Druckfestigkeit der technisch wichtigsten Baustoffe*, 3rd ed. Wien: F. Deuticke, 1903.
- [14] C. Petersen, *Statik und Stabilität der Baukonstruktionen: Elasto- und plasto-statische Berechnungsverfahren druckbeanspruchter Tragwerke: Nachweisformen gegen Knicken, Kippen, Beulen*, 2nd ed. Braunschweig: Vieweg, 1992.
- [15] H. Beer and G. Schulz, "Die Traglast des planmäßig mittig gedrückten Stabs mit Imperfektionen," *Konstruktion und Fertigung*, Nr. 21+23, 1969.
- [16] H. Beer and G. Schulz, "The theoretical basis of the new buckling curves," *Construction Métrallique*, N. 3, 1970.

- [17] H. Beer and G. Schulz, "The European column curves," *IABSE reports of the working commissions*, Nr. 23, 1975, doi: 10.5169/SEALS-19828.
- [18] ECCS, "Manual on Stability of Steel Structures," 1976.
- [19] R. Maquoi and J. Rondal, "Maquoi Rondal Analytische Formulierung der neuen Europäischen Knickspannungskurven," 1978.
- [20] N. Boissonnade, R. Greiner, J. P. Jaspart, and J. Lindner, "Rules for Member Stability in EN 1993-1-1: Background documentation and design guidelines," 2006.
- [21] J. Jönsson and T.-C. Stan, "European column buckling curves and finite element modelling including high strength steels," *Journal of Constructional Steel Research*, vol. 128, pp. 136–151, 2017, doi: 10.1016/j.jcsr.2016.08.013.
- [22] R. V. Southwell, "On the analysis of experimental observations in problems of elastic stability," *Proc. R. Soc. Lond. A*, vol. 135, no. 828, pp. 601–616, 1932, doi: 10.1098/rspa.1932.0055.
- [23] H. R. Fisher, "An Extension of Southwell's Method of Analysing Experimental Observations in Problems of Elastic Stability," *Proceedings of the Royal Society of London. Series A, Containing Papers of a*, vol. 144, 1934.
- [24] J. Singer, "On the applicability of the Southwell plot to plastic buckling," *Experimental Mechanics*, pp. 205–208, 1989.
- [25] J. Marcinowski, M. Sadowski, and V. Sakharov, "On the applicability of Southwell's method to the determination of the critical force of elastic columns of variable cross sections," *Acta Mech*, vol. 233, no. 11, pp. 4861–4875, 2022, doi: 10.1007/s00707-022-03345-w.
- [26] J. Nonn and M. Feldmann, "Imperfections of LTB tests with directionally true loading using the extended Southwell-method," *ce papers*, vol. 4, 2-4, pp. 2215–2220, 2021, doi: 10.1002/cepa.1541.
- [27] M. Empelmann, V. Oettel, and S. Kim, "Innovative Stützen für den Hochhausbau," in *Massivbau im Wandel: Festschrift zum 60. Geburtstag von Josef Hegger*, Berlin: Ernst, 2014.
- [28] K. Roik, R. Bergmann, H. Bode, and G. Wagenknecht, "Tragfähigkeit von ausbetonierten Hohlprofilstützen aus Baustahl," *Technisch-wissenschaftliche Mitteilungen*, Institut für den konstruktiven Ingenieurbau, Ruhr-Univ. Bochum, 1975.
- [29] K. Roik and G. Wagenknecht, "Ermittlung der Grenztragfähigkeit von ausbetonierten Hohlprofilstützen aus Baustahl," *Der Bauingenieur*, vol. 51, pp. 183–188, 1976.
- [30] R. Bergmann, "Zur Geschichte der Biegesteifigkeit bei Verbundstützen," *Stahlbau*, vol. 73, no. 9, pp. 656–660, 2004.
- [31] K. Roik, R. Bergmann, H. Bode, and G. Wagenknecht, "Tragverhalten von Stahlstützen im Verbund mit Beton (Hohlprofile)," *Abschlussbericht Projekt P08.1 Studiengesellschaft für Anwendungstechnik von Eisen und Stahl e.V.*, 1975.

- [32] R. Bergmann, "Traglastberechnung von Verbundstützen," Inst. für Konstruktiven Ingenieurbau, Ruhr-Univ. Bochum, 1981.
- [33] J. Lindner, "Geometrische Ersatzimperfectionen für Verbundstützen, die in die Knickspannungslinien b und c eingestuft sind," Schlußbericht zum Forschungsvorhaben DIBt IV 1-5-787/96, 1996.
- [34] J. Lindner, "Ein Vorschlag für einheitliche vereinfachte Tragsicherheitsnachweise von Stahlstützen und Verbundstützen," *Stahlbau*, vol. 63, no. 9, 1994.
- [35] J. Lindner and R. Bergmann, "Zur Bemessung von Verbundstützen nach 18800 Teil 5," *Stahlbau*, vol. 67, no. 7, 1998.
- [36] M. D. Denavit, J. F. Hajjar, T. Perea, and R. T. Leon, "Elastic flexural rigidity of steel-concrete composite columns," *Engineering Structures*, vol. 160, pp. 293–303, 2018, doi: 10.1016/j.engstruct.2018.01.044.
- [37] *prEN 1993-1-14:2023, Eurocode 3: Design of steel structures - Part 1-14: Design assisted by finite element analysis*, CEN.
- [38] M. Lippes, *Zur Bemessung von Hohlprofil-Verbundstützen aus hochfesten Stählen und Betonen*. Wuppertal, 2008.
- [39] M. Neuenschwander, M. Knobloch, and M. Fontana, "Fire behavior of concrete filled circular hollow section columns with massive steel core," *Proceeding SDSS Rio 2010 STABILITY AND DUCTILITY OF STEEL STRUCTURES*, 2010.
- [40] I. Kleibömer, "Zum Verbundverhalten von Verbundstützen mit massivem Stahlkern im Brandfall," 2018.
- [41] J. Nonn *et al.*, "Universelle Hochleistungsstützen aus S960 ohne Schweißen; Schlussbericht zum IGF-Vorhaben 21458 N," 2024.
- [42] J. Liew and D. X. Xiong, "Ultra-High Strength Concrete Filled Composite Columns for Multi-Storey Building Construction," *Advances in Structural Engineering*, vol. 15, no. 9, pp. 1487–1503, 2012.
- [43] J. Liew and D. X. Xiong, "Experimental investigation on tubular columns infilled with ultra-high strength concrete," pp. 637–645, 2011, doi: 10.1201/b10564-88.
- [44] M. L. Romero *et al.*, "Circular concrete-filled dual steel columns with ultrahigh-strength concrete," *Steel Construction*, vol. 9, no. 4, pp. 323–330, 2016, doi: 10.1002/stco.201610038.
- [45] P. Schurgacz and M. Knobloch, "Betongefüllte Hohlprofilverbundstützen für Geschossbauten - Innovation und Bemessung; Schlussbericht zum IGF-Vorhaben 19677 N," Ruhr-Universität Bochum, Lehrstuhl für Stahl-, Leicht- und Verbundbau, 2021.

- [46] A. Espinos, M. L. Romero, and D. Lam, "Fire performance of innovative steel-concrete composite columns using high strength steels," *Thin-Walled Structures*, vol. 106, pp. 113–128, 2016, doi: 10.1016/j.tws.2016.04.014.
- [47] B. Lai, J. Liew, and Richard Y., "Design and testing of concrete encased steel composite beam-columns with C90 concrete and S690 steel section," *Engineering Structures*, vol. 220, p. 110995, 2020, doi: 10.1016/j.engstruct.2020.110995.
- [48] B.-L. Lai, R.-L. Bao, M.-Y. Zhang, Y.-H. Wang, and J. R. Liew, "Evaluation on the static and seismic performance of steel reinforced concrete composite columns with high strength materials," *Journal of Building Engineering*, vol. 79, p. 107886, 2023, doi: 10.1016/j.job.2023.107886.
- [49] J. L. Bonet, M. L. Romero, and P. F. Miguel, "Effective flexural stiffness of slender reinforced concrete columns under axial forces and biaxial bending," *Engineering Structures*, vol. 33, no. 3, pp. 881–893, 2011, doi: 10.1016/j.engstruct.2010.12.009.
- [50] L.-H. Han, "Flexural behaviour of concrete-filled steel tubes," *Journal of Constructional Steel Research*, vol. 60, no. 2, pp. 313–337, 2004, doi: 10.1016/j.jcsr.2003.08.009.
- [51] L.-H. Han, H. Lu, G.-H. Yao, and F.-Y. Liao, "Further study on the flexural behaviour of concrete-filled steel tubes," *Journal of Constructional Steel Research*, vol. 62, no. 6, pp. 554–565, 2006, doi: 10.1016/j.jcsr.2005.09.002.
- [52] B. Lai and J. Liew, "Axial-moment interaction of high strength concrete encased steel composite columns: Experimental investigation," *Journal of Constructional Steel Research*, vol. 175, p. 106370, 2020, doi: 10.1016/j.jcsr.2020.106370.
- [53] A. Tretyakov, I. Tkalenko, F. Wald, J. Novak, R. Stefan, and A. Kohoutková, "Flexural stiffness of the composite steel and fibre-reinforced concrete circular hollow section column," *IOP Conf. Ser.: Mater. Sci. Eng.*, vol. 246, p. 12021, 2017, doi: 10.1088/1757-899X/246/1/012021.
- [54] Z. Huang, B. Uy, D. Li, and J. Wang, "Behaviour and design of ultra-high-strength CFST members subjected to compression and bending," *Journal of Constructional Steel Research*, vol. 175, p. 106351, 2020, doi: 10.1016/j.jcsr.2020.106351.
- [55] G. A. Alpsten, "Thermal residual stresses in hot-rolled steel members," Fritz Engineering Laboratory, Lehigh University, Bethlehem, Pennsylvania, Fritz Engineering Laboratory Report 337.3, 1968.
- [56] Y. Kishima, G. A. Alpsten, and L. Tall, "Residual stresses in welded shapes of flame-cut plates in ASTM A572(50) steel," Fritz Engineering Laboratory, Lehigh University, Bethlehem, Pennsylvania, Fritz Engineering Laboratory Report, 1969.
- [57] B. W. Young and J. B. Dwight, "Residual stresses and their effect on the moment-curvature properties of structural steel sections," CIRIA Notes 32, 1971.
- [58] N. R. Rao and L. Tall, "Residual stresses in welded plates," *The Welding Journal*, no. 40, 1961.

- [59] E. Odar, Nishino F., and L. Tall, "Residual stresses in rolled heat treated T-1 shapes," Fritz Engineering Laboratory, Lehigh University, Bethlehem, Pennsylvania, 1965.
- [60] E. Odar, "Residual stresses in T-1 constructional alloy steel plates," Master's Thesis, Lehigh University, 1964.
- [61] R. Thiébaud and J.-P. Lebet, "Experimental study of residual stresses in thick steel plates," *Proceedings of the Annual Stability Conference Structural Stability Research Council*, 2012.
- [62] T. Schaupp, D. Schröpfer, A. Kromm, and T. Kannengiesser, "Welding Residual Stress Distribution of Quenched and Tempered and Thermo-Mechanically Hot Rolled High Strength Steels," *AMR*, vol. 996, pp. 457–462, 2014, doi: 10.4028/www.scientific.net/AMR.996.457.
- [63] M. Schäfers, T. Ghanbari-Ghazijahani, S. Ameri, J. Zehfuß, and M. Mensinger, "-currently under revision- Full-Scale Experiments on Novel Hybrid Columns Including Laminated High-Strength Plates Infilled in Hollow Sections," *Journal of Structural Engineering*, submitted 2024.
- [64] N. Sauerborn and J. Kretz, "Verbundstützen," in *Stahlbau-Kalender*, vol. 12.2010, *Stahlbau-Kalender 2010*, U. Kuhlmann, Ed., 12th ed., Berlin: Wiley, 2010, pp. 423–482.
- [65] Creaform Inc., "Produktdatenblatt HandySCAN 3D BLACK Elite,"
- [66] M. Schäfer, M. Bergmann, and Q. Zhang, "Bemessung von Verbundstützen – Update prEN 1994-1-1," *Stahlbau*, vol. 90, no. 12, pp. 903–912, 2021, doi: 10.1002/stab.202100089.
- [67] *DIN EN 10210-2:2019-06, Warmgefertigte Hohlprofile für den Stahlbau – Teil 2: Grenzabmaße, Maße und statische Werte*, DIN Deutsches Institut für Normung e.V.
- [68] M. Schäfers, E. Müller, and M. Mensinger, "Experimental investigations of residual stresses in thick high-strength steel plates," *ce/papers*, vol. 6, 3-4, pp. 545–550, 2023, doi: 10.1002/cepa.2369.
- [69] *SIS 05 5900-1967*, Standardiseringskommissionen i Sverige.
- [70] *EN ISO 8501-1:2007-12, Preparation of steel substrates before application of paints and related products - Visual assessment of surface cleanliness - Part 1: Rust grades and preparation grades of uncoated steel substrates and of steel substrates after overall removal of previous coatings (ISO 8501-1:2007)*, CEN.
- [71] K. Tanaka and Y. Akinawa, "Diffraction Measurements of Residual Macrostress and Microstress Using X-Rays, Synchrotron and Neutrons," *JSME Int. J., Ser. A*, vol. 47, no. 3, pp. 252–263, 2004, doi: 10.1299/jsmea.47.252.
- [72] T. Sasaki, R. Mizuno, S. Takago, and Y. Mishima, "Standardization of Cos α Method for X-Ray Stress Measurement," *MSF*, vol. 1016, pp. 1240–1245, 2021, doi: 10.4028/www.scientific.net/MSF.1016.1240.
- [73] C. Kittel, *Kittel's Introduction to Solid State Physics, 9. Edition*: Wiley.

- [74] N. Tebedge, G. Alpsten, and L. Tall, "Residual-stress measurement by the sectioning method," *Experimental Mechanics*, vol. 13, no. 2, pp. 88–96, 1973, doi: 10.1007/BF02322389.
- [75] ECCS, "Testing Procedures," 1984.
- [76] R. C. Spoorenberg, H. H. Snijder, L.-G. Cajot, and M. S. May, "Experimental investigation on residual stresses in heavy wide flange QST steel sections," *Journal of Constructional Steel Research*, vol. 89, pp. 63–74, 2013, doi: 10.1016/j.jcsr.2013.06.009.
- [77] L. Schaper, F. Jörg, R. Winkler, U. Kuhlmann, and M. Knobloch, "The simplified method of the equivalent compression flange," *Steel Construction*, vol. 12, no. 4, pp. 264–277, 2019, doi: 10.1002/stco.201900033.
- [78] F. A. Kandil, J. D. Lord, Fry A. T., and P. V. Grant, "A review of residual stress measurement methods: A guide to technique selection," Teddington, NPL report MATC A NPL MATC A 4, 2001.
- [79] SIMULIA, *Abaqus/Standard 2020*: D'Assault Systèmes.
- [80] M. Sargin, *Stress-strain Relationship for Concrete and the Analysis of Structural Concrete Sections*: Solid Mechanics Division University of Waterloo, 1971.
- [81] *EN 1992-1-1:2011-01, Eurocode 2: Design of concrete structures – Part 1-1: General rules and rules for buildings*, CEN.
- [82] A. Hillerborg, M. Modéer, and P.-E. Petersson, "Analysis of crack formation and crack growth in concrete by means of fracture mechanics and finite elements," *Cement and Concrete Research*, vol. 6, no. 6, pp. 773–781, 1976, doi: 10.1016/0008-8846(76)90007-7.
- [83] M. Hafezolghorani, F. Hejazi, R. Vaghei, M. S. B. Jaafar, and K. Karimzade, "Simplified Damage Plasticity Model for Concrete," *Structural Engineering International*, vol. 27, no. 1, pp. 68–78, 2017, doi: 10.2749/101686616X1081.
- [84] A. H. Al-Zuhairi, A. H. Al-Ahmed, A. A. Abdulhameed, and A. N. Hanoon, "Calibration of a New Concrete Damage Plasticity Theoretical Model Based on Experimental Parameters," *Civ Eng J*, vol. 8, no. 2, pp. 225–237, 2022, doi: 10.28991/CEJ-2022-08-02-03.
- [85] D. Kueres, A. Stark, M. Herbrand, and M. Claßen, "Numerische Abbildung von Beton mit einem plastischen Schädigungsmodell – Grundlegende Untersuchungen zu Normalbeton und UHPC/Finite element simulation of concrete with a plastic damage model – Basic studies on normal strength concrete and UHPC," *Bauingenieur*, vol. 90, no. 06, pp. 252–264, 2015, doi: 10.37544/0005-6650-2015-06-44.
- [86] *EN 1090-2:2018, Execution of steel structures and aluminium structures - Part 2: Technical requirements for steel structures*, CEN.
- [87] W. Römer, "Tragfähigkeitsberechnungen für Kehlnähte auf Grundlage experimentell gestützter Werkstoffmodellierung," Dissertation, kassel university press, 2015.

- [88] A. Stamenkovic and M. J. Gardner, "Effect of residual stresses on the column behaviour of hot-finished structural steel hollow sections," *Proceedings of the Institution of Civil Engineers*, no. 75, pp. 599–616, 1983.
- [89] M. A. Bradford, H. Y. Loh, and B. Uy, "Local Buckling of Concrete-Filled Circular Steel Tubes," in *Composite construction in steel and concrete IV: Proceedings of the conference, May 28 - June 2, 2000, Banff, Alberta, Canada, 2002*, pp. 563–572.
- [90] M. A. Bradford, H. Y. Loh, and B. Uy, "Slenderness limits for filled circular steel tubes," *Journal of Constructional Steel Research*, vol. 58, no. 2, pp. 243–252, 2002, doi: 10.1016/S0143-974X(01)00043-8.
- [91] *EN 10025-6:2019, Hot rolled products of structural steels - Part 6: Technical delivery conditions for flat products of high yield strength structural steels in the quenched and tempered condition*, CEN.
- [92] *DIN EN 1993-1-1/NA:2022-10, National Annex – Nationally determined parameters – Eurocode 3: Design of steel structures – Part 1-1: General rules and rules for buildings*.
- [93] *EN 1990:2021-10, Eurocode: Basis of structural design*, CEN.
- [94] R. C. Spoorenberg, H. H. Snijder, L.-G. Cajot, and N. Popa, "Buckling curves for heavy wide flange QST columns based on statistical evaluation," *Journal of Constructional Steel Research*, vol. 101, pp. 280–289, 2014, doi: 10.1016/j.jcsr.2014.05.017.

6 Annex

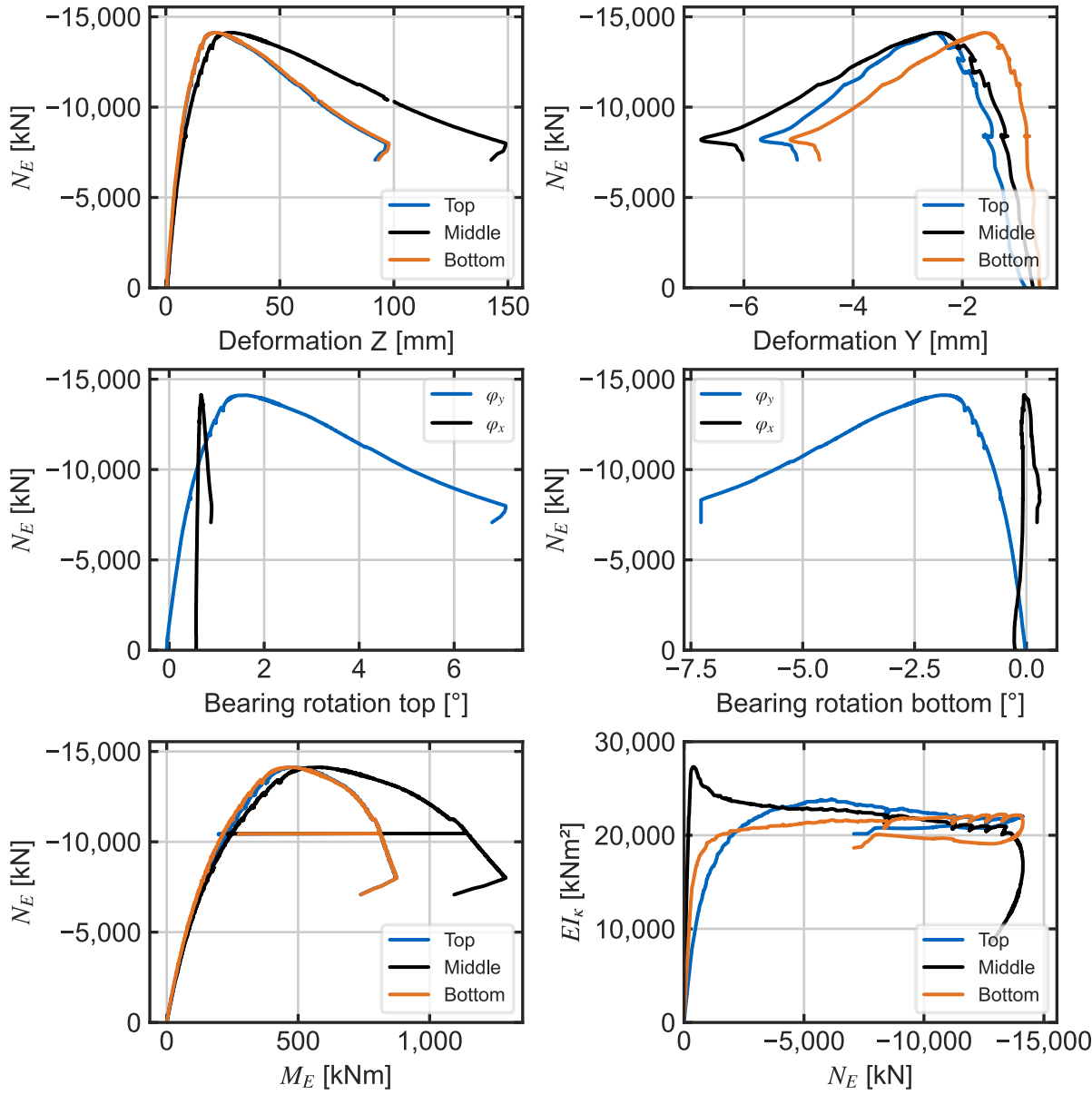


Figure 6-1 Recordings of experimental buckling test KR-1.

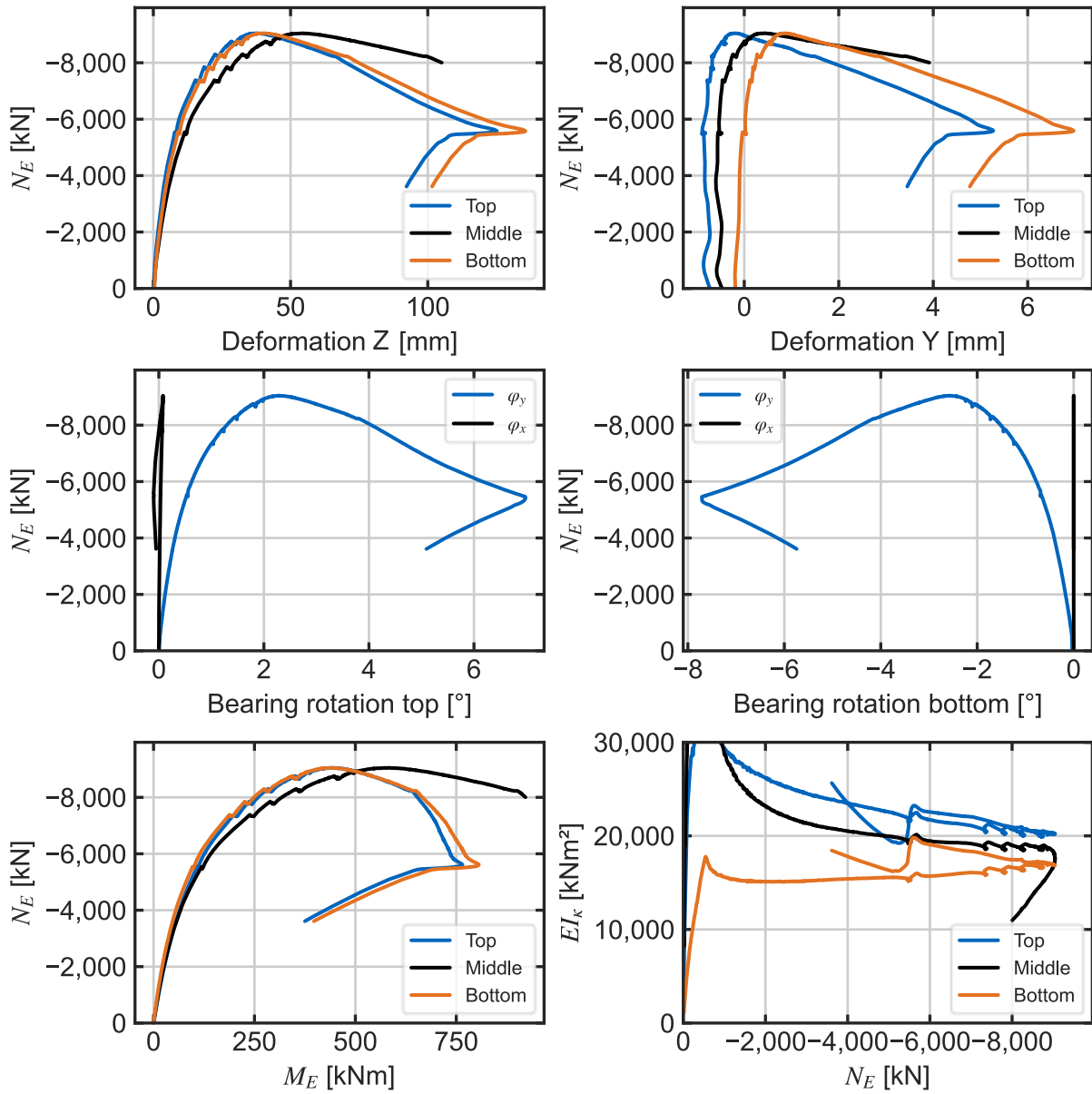


Figure 6-2 Recordings of experimental buckling test KR-2.

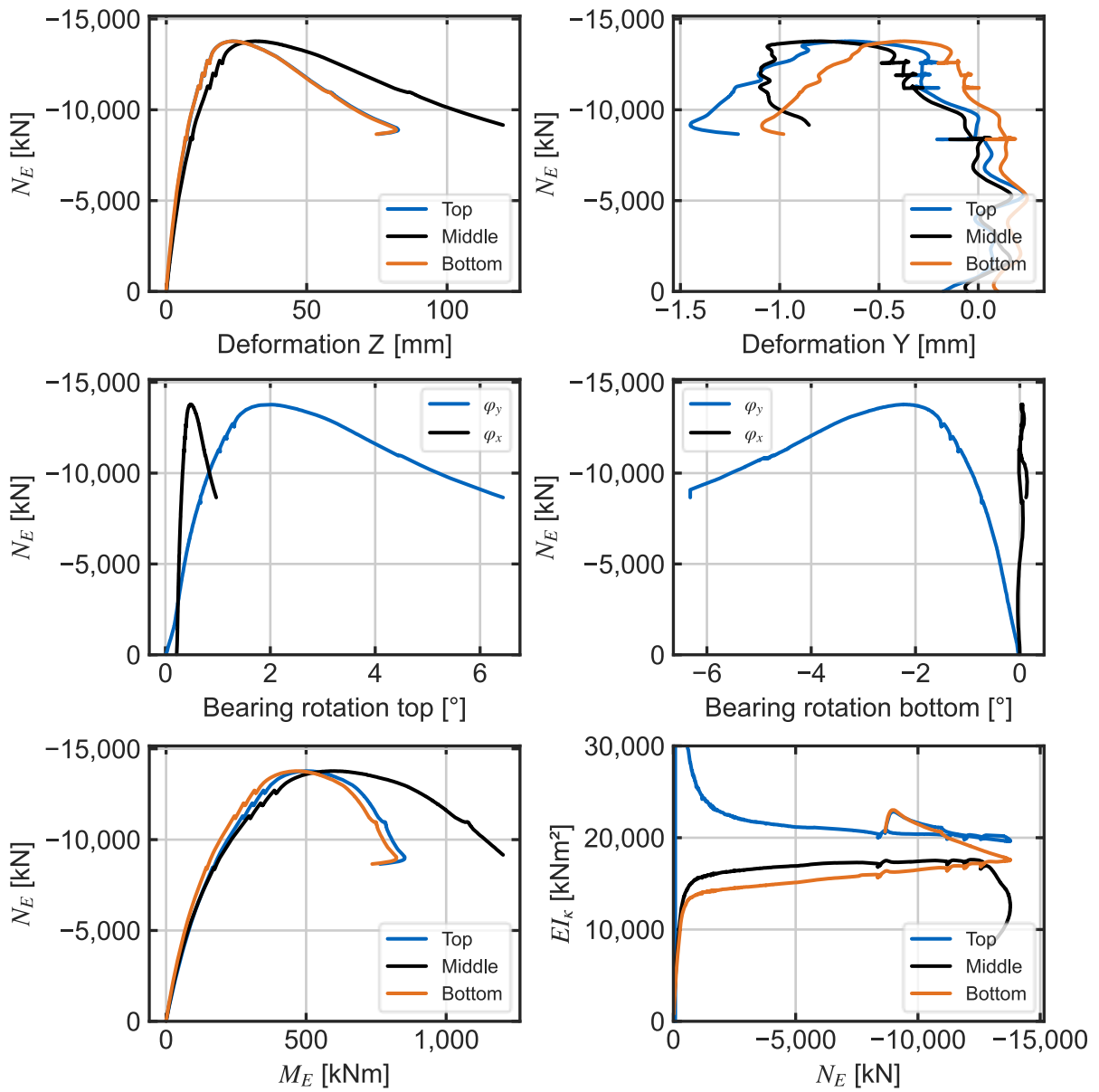


Figure 6-3 Recordings of experimental buckling test KR-3.

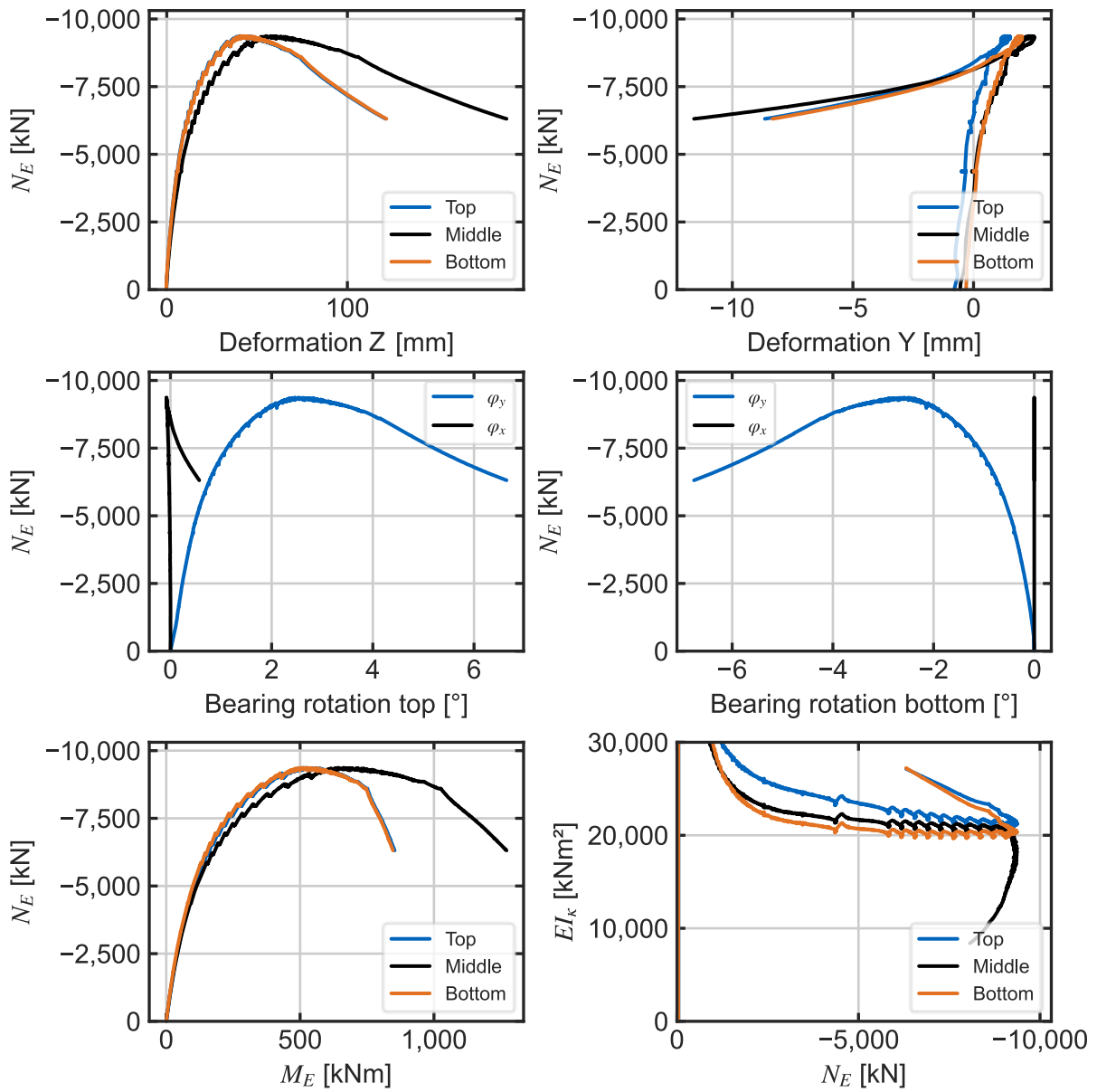


Figure 6-4 Recordings of experimental buckling test KR-4.

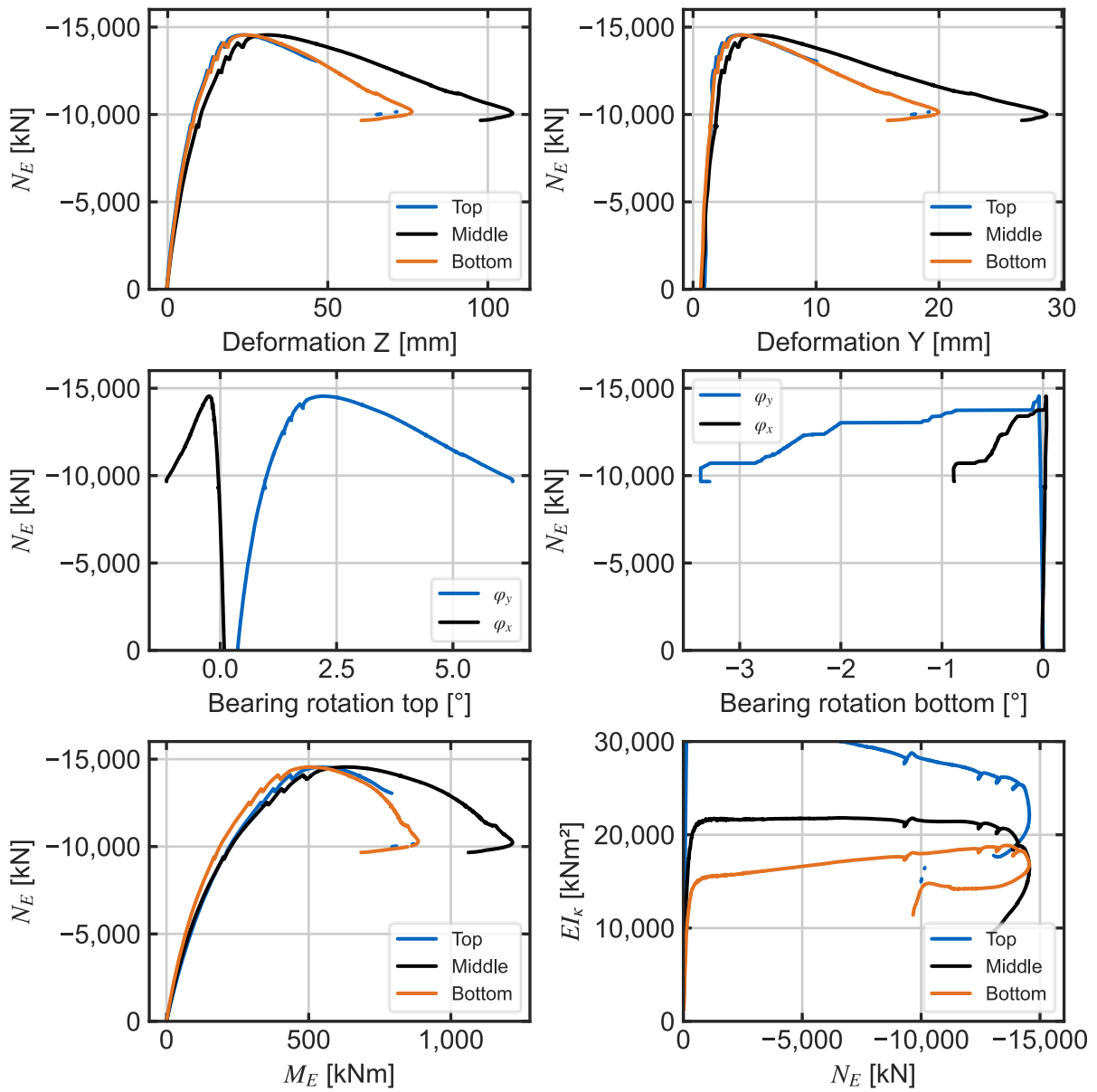


Figure 6-5 Recordings of experimental buckling test KR-5.

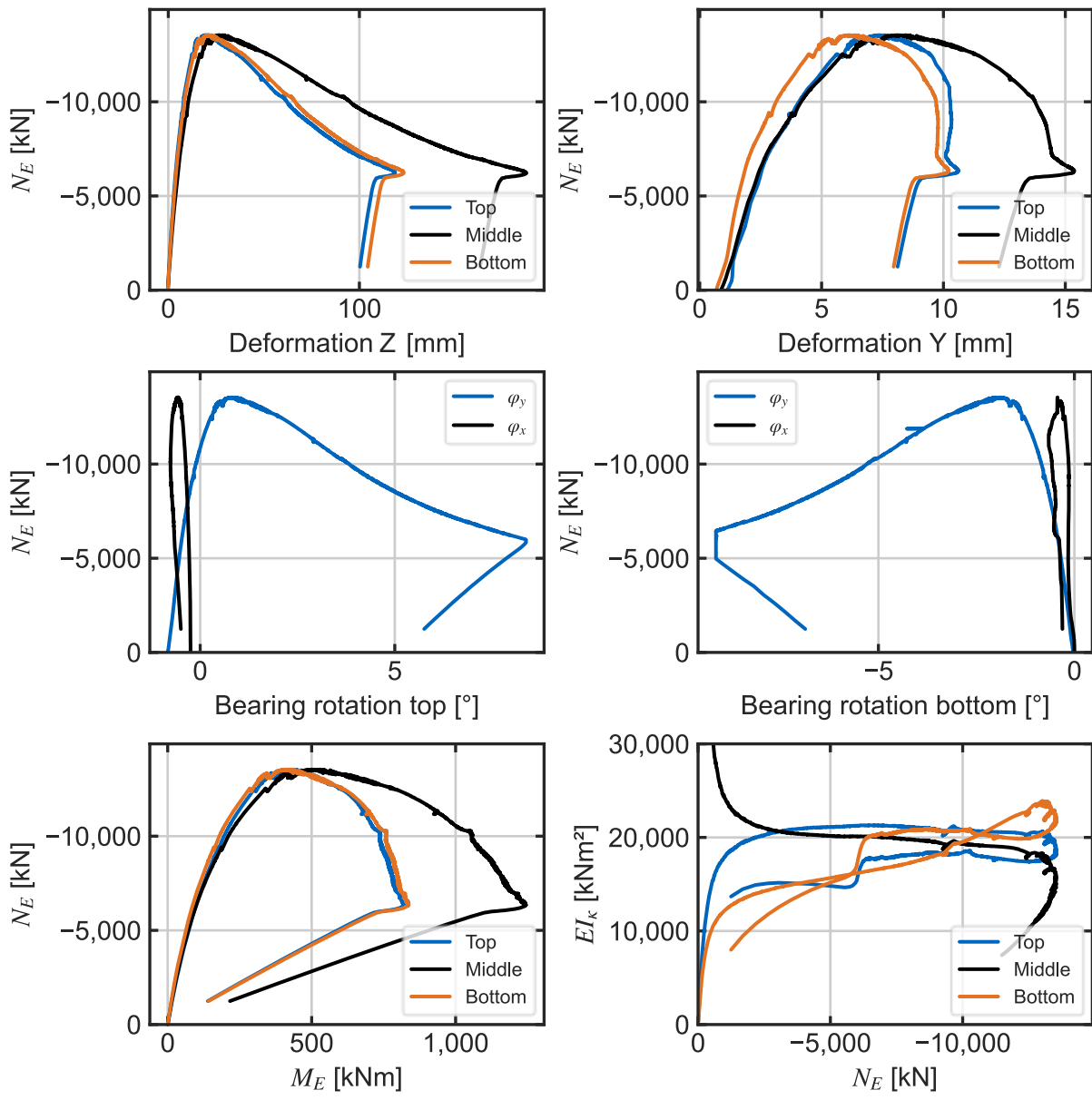


Figure 6-6 Recordings of experimental buckling test KR-6.

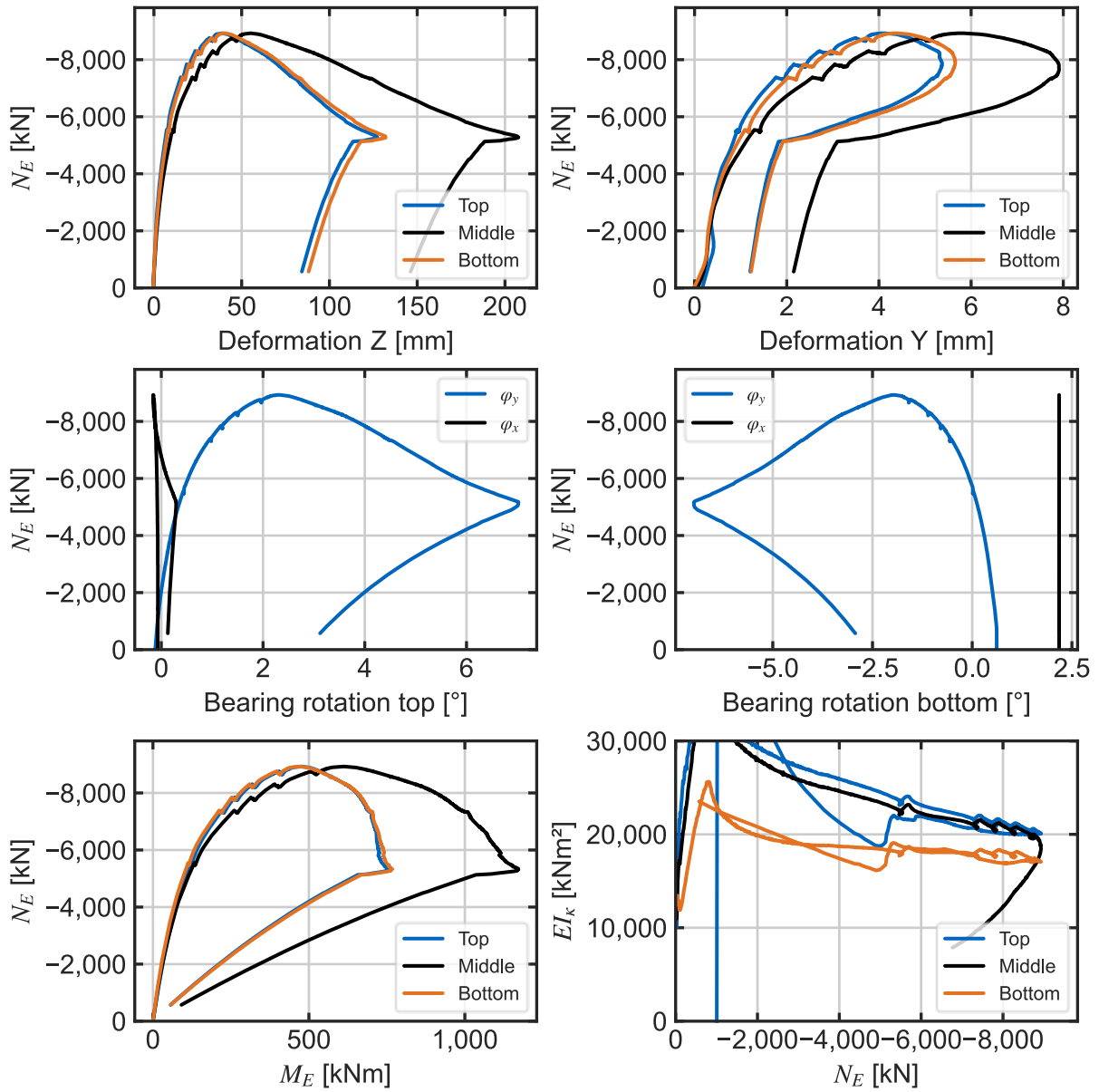


Figure 6-7 Recordings of experimental buckling test KR-7.

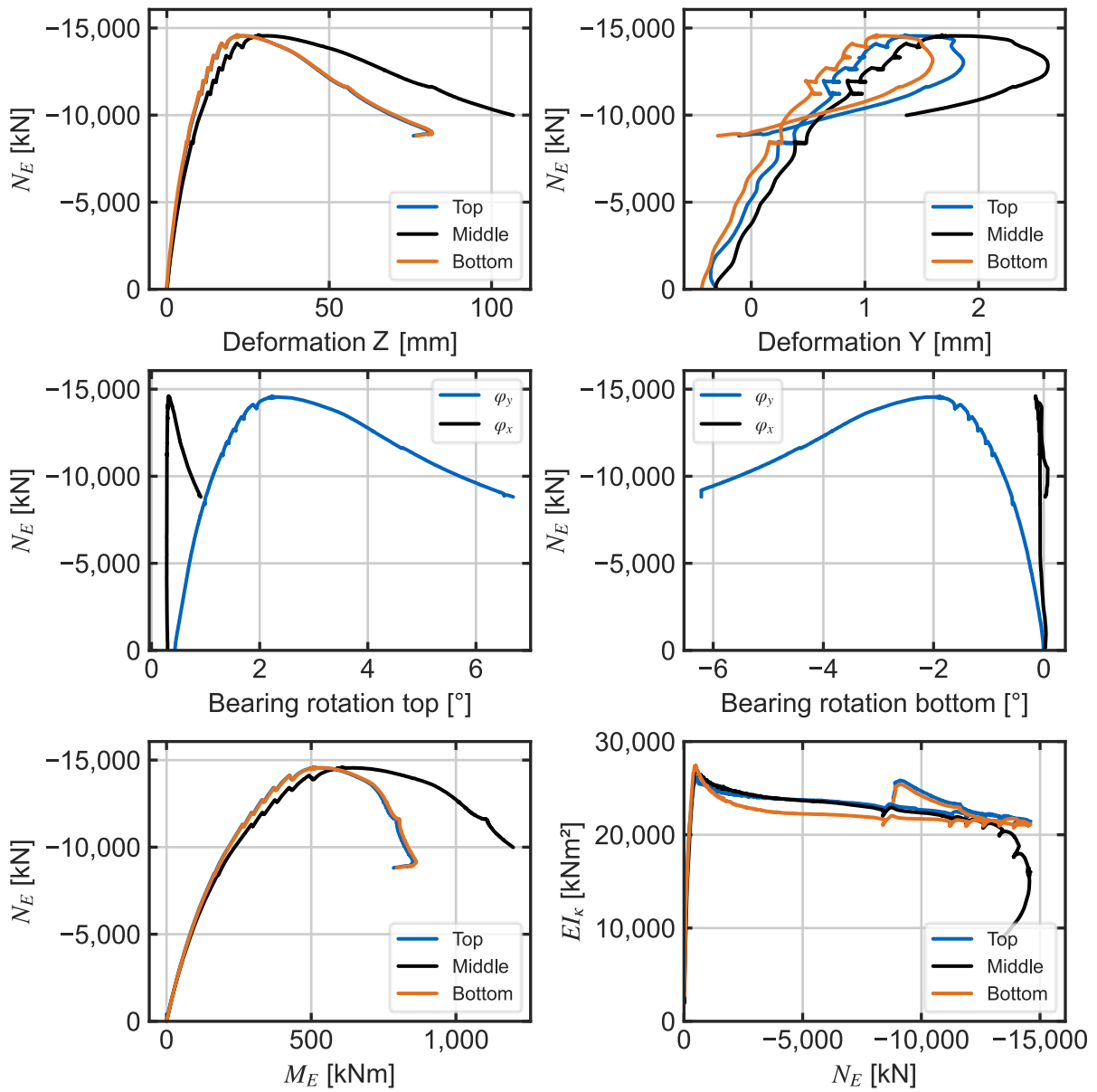


Figure 6-8 Recordings of experimental buckling test KR-8.

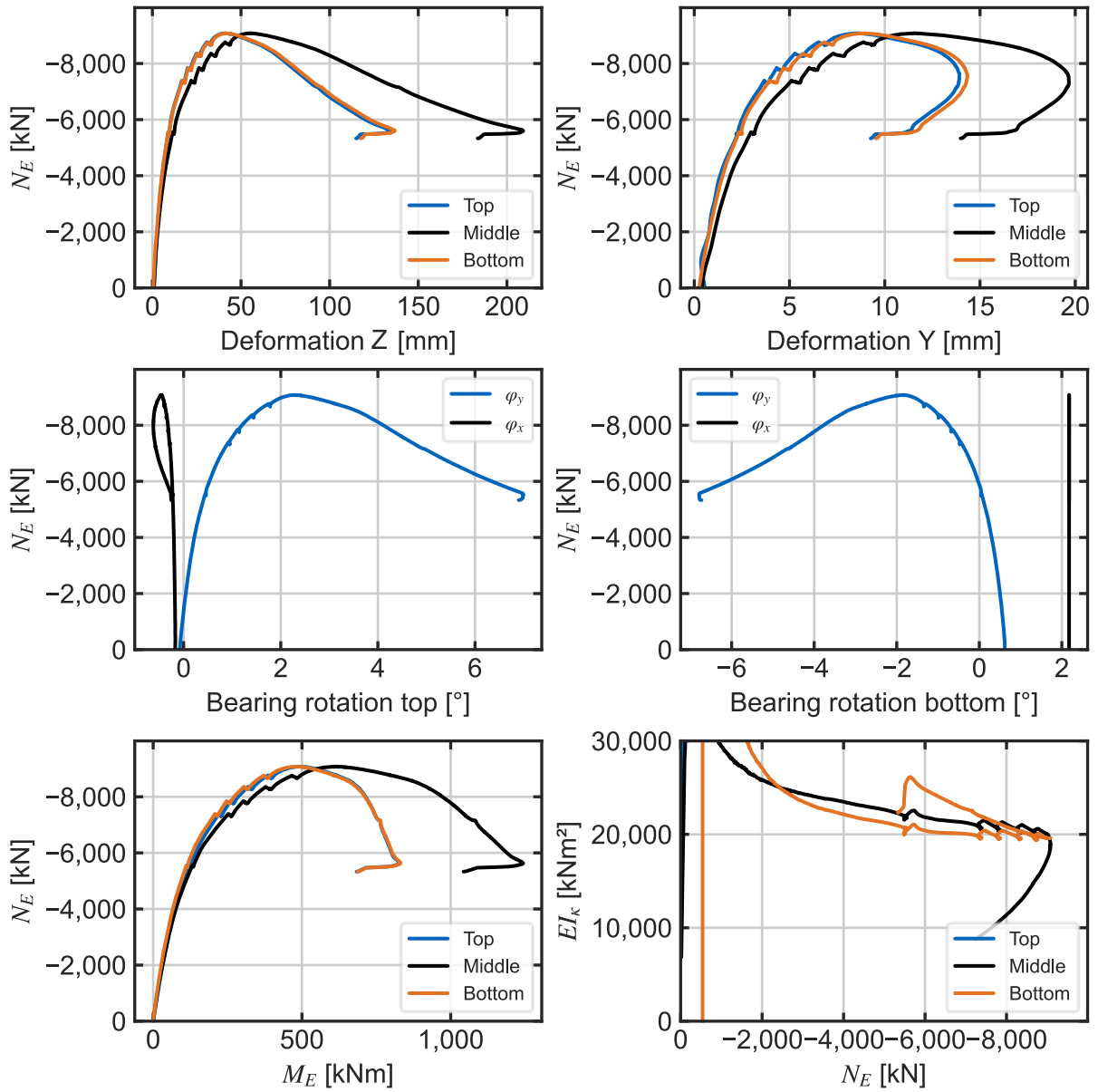


Figure 6-9 Recordings of experimental buckling test KR-9.

Results from sectioning method

Table 6-1 Strain recording sectioning of specimen 1-1.

Segment	ε_{top} [-]	ε_{bottom} [-]	ε_{corr} [-]	ε_{tot} [-]	$\sigma_{RS} = E \cdot \varepsilon_{tot}$ [MPa]
1-1-1	0.00108	0.00013	0.00002	0.00123	127.96
1-1-2	-0.00014	-0.00015	0.00000	-0.00029	-29.51
1-1-3	-0.00031	-0.00003	0.00000	-0.00034	-35.51
1-1-4	-0.00020	-0.00002	0.00000	-0.00022	-22.42
1-1-5	-0.00036	0.00012	0.00000	-0.00024	-24.61
1-1-6	-0.00032	-0.00005	0.00000	-0.00037	-37.70
1-1-7	-0.00025	0.00010	0.00000	-0.00015	-15.81
1-1-8	-0.00019	-0.00001	0.00000	-0.00020	-20.50
1-1-9	-0.00019	-0.00002	0.00000	-0.00021	-21.08
1-1-10	-0.00030	-0.00002	0.00000	-0.00032	-33.02
1-1-11	-0.00017	-0.00003	0.00000	-0.00020	-20.22
1-1-12	-0.00025	-0.00007	0.00000	-0.00032	-32.80
1-1-13	-0.00063	0.00000	0.00000	-0.00063	-64.21
1-1-14	-0.00013	-0.00005	0.00000	-0.00018	-19.09
1-1-15	0.00115	0.00042	0.00000	0.00157	161.06

Table 6-2 Strain recording sectioning of specimen 1-2.

Segment	ε_{top} [-]	ε_{bottom} [-]	ε_{corr} [-]	ε_{tot} [-]	$\sigma_{RS} = E \cdot \varepsilon_{tot}$ [MPa]
1-2-1	0.00107	-0.00005	0.00001	0.00102	101.48
1-2-2	-0.00017	-0.00023	0.00000	-0.00040	-44.14
1-2-3	-0.00015	-0.00019	0.00000	-0.00033	-36.80
1-2-4	-0.00003	-0.00024	0.00000	-0.00027	-29.96
1-2-5	-0.00009	-0.00022	0.00000	-0.00032	-34.49
1-2-6	-0.00005	-0.00016	0.00000	-0.00021	-24.03
1-2-7	-0.00017	-0.00023	0.00000	-0.00040	-42.62
1-2-8	-0.00008	-0.00001	0.00000	-0.00009	-10.81
1-2-9	-0.00026	-0.00011	0.00000	-0.00037	-40.08
1-2-10	-0.00023	-0.00011	0.00000	-0.00034	-36.54
1-2-11	-0.00007	-0.00016	0.00000	-0.00023	-25.32
1-2-12	-0.00003	-0.00016	0.00000	-0.00019	-21.52
1-2-13	-0.00005	-0.00015	0.00000	-0.00021	-23.40
1-2-14	-0.00020	0.00000	0.00000	-0.00020	-22.55
1-2-15	0.00135	0.00050	0.00002	0.00187	191.03

Table 6-3 Strain recording sectioning of specimen 2-1.

Segment	ε_{top} [-]	ε_{bottom} [-]	ε_{corr} [-]	ε_{tot} [-]	$\sigma_{RS} = E \cdot \varepsilon_{tot}$ [MPa]
2-1-1	0.00127	0.00028	0.00000	0.00078	158.95
2-1-2	-0.00013	-0.00012	0.00000	-0.00025	-25.65
2-1-3	-0.00018	-0.00005	0.00000	-0.00023	-23.83
2-1-4	-0.00013	-0.00006	0.00000	-0.00019	-19.45
2-1-5	-0.00011	-0.00023	0.00000	-0.00034	-34.73
2-1-6	-0.00017	-0.00020	0.00000	-0.00037	-37.49
2-1-7	-0.00015	-0.00020	0.00000	-0.00035	-35.67
2-1-8	-0.00024	-0.00027	0.00000	-0.00051	-52.06
2-1-9	-0.00028	-0.00004	0.00000	-0.00032	-32.59
2-1-10	-0.00019	0.00003	0.00000	-0.00016	-16.17
2-1-11	-0.00029	0.00002	0.00000	-0.00027	-27.64
2-1-12	-0.00023	-0.00010	0.00000	-0.00033	-33.42
2-1-13	-0.00025	-0.00008	0.00000	-0.00033	-33.98
2-1-14	-0.00022	-0.00013	0.00000	-0.00035	-35.92
2-1-15	0.00123	0.00025	0.00000	0.00148	152.00

Table 6-4 Strain recording sectioning of segment 2-2.

Segment	ε_{top} [-]	ε_{bottom} [-]	ε_{corr} [-]	ε_{tot} [-]	$\sigma_{RS} = E \cdot \varepsilon_{tot}$ [MPa]
2-2-1	0.00138	0.00020	0.00003	0.00081	166.07
2-2-2	-0.00033	-0.00028	0.00000	-0.00061	-62.86
2-2-3	-0.00040	-0.00023	0.00000	-0.00062	-63.88
2-2-4	-0.00056	-0.00021	0.00000	-0.00077	-79.13
2-2-5	-0.00035	-0.00008	0.00000	-0.00043	-44.35
2-2-6	-0.00052	-0.00005	0.00000	-0.00057	-58.73
2-2-7	-0.00065	-0.00008	0.00000	-0.00073	-75.30
2-2-8	-0.00056	-0.00001	0.00000	-0.00057	-58.28
2-2-9	-0.00065	-0.00005	0.00000	-0.00069	-71.11
2-2-10	-0.00031	-0.00008	0.00000	-0.00038	-39.37
2-2-11	-0.00065	-0.00011	0.00000	-0.00076	-78.33
2-2-12	-0.00058	-0.00020	0.00000	-0.00078	-80.05
2-2-13	-0.00054	-0.00027	0.00000	-0.00081	-82.96
2-2-14	-0.00042	-0.00023	0.00000	-0.00064	-65.93
2-2-15	0.00119	0.00012	0.00006	0.00137	140.16

Table 6-5 Strain recording sectioning of segment 3-1.

Segment	ε_{top} [-]	ε_{bottom} [-]	ε_{corr} [-]	ε_{tot} [-]	$\sigma_{RS} = E \cdot \varepsilon_{tot}$ [MPa]
3-1-1	0.00127	0.00084	0.00002	0.00106	216.02
3-1-2	-0.00002	-0.00025	0.00000	-0.00013	-27.58
3-1-3	-0.00005	-0.00023	0.00000	-0.00014	-28.40
3-1-4	-0.00020	-0.00020	0.00000	-0.00020	-40.99
3-1-5	-0.00023	-0.00020	0.00000	-0.00021	-43.74
3-1-6	-0.00020	-0.00018	0.00000	-0.00019	-38.05
3-1-7	-0.00022	-0.00013	0.00000	-0.00018	-36.43
3-1-8	-0.00010	-0.00020	0.00000	-0.00015	-30.29
3-1-9	-0.00015	-0.00024	0.00000	-0.00019	-39.65
3-1-10	-0.00012	-0.00021	0.00000	-0.00016	-33.66
3-1-11	-0.00018	-0.00021	0.00000	-0.00020	-40.47
3-1-12	-0.00021	-0.00022	0.00000	-0.00021	-43.45
3-1-13	-0.00020	-0.00016	0.00000	-0.00018	-36.66
3-1-14	-0.00027	-0.00011	0.00000	-0.00019	-38.85
3-1-15	-0.00021	-0.00016	0.00000	-0.00019	-38.59
3-1-16	-0.00023	-0.00010	0.00000	-0.00017	-34.03
3-1-17	-0.00018	-0.00020	0.00000	-0.00019	-39.54
3-1-18	-0.00009	-0.00017	0.00000	-0.00013	-27.16
3-1-19	-0.00023	-0.00013	0.00000	-0.00018	-37.03
3-1-20	-0.00027	-0.00013	0.00000	-0.00020	-41.14
3-1-21	-0.00021	-0.00018	0.00000	-0.00020	-40.02
3-1-22	-0.00003	-0.00019	0.00000	-0.00011	-23.06
3-1-23	-0.00023	-0.00014	0.00000	-0.00019	-38.12
3-1-24	-0.00017	-0.00011	0.00000	-0.00014	-28.63
3-1-25	-0.00021	-0.00006	0.00000	-0.00014	-27.82
3-1-26	-0.00025	-0.00011	0.00000	-0.00018	-36.23
3-1-27	-0.00033	-0.00017	0.00000	-0.00025	-51.01
3-1-28	-0.00031	-0.00013	0.00000	-0.00022	-45.53
3-1-29	-0.00027	-0.00013	0.00000	-0.00020	-41.33
3-1-30	0.00138	0.00043	0.00004	0.00093	185.91

Table 6-6 Strain recording sectioning of segment 3-2.

Segment	ε_{top} [-]	ε_{bottom} [-]	ε_{corr} [-]	ε_{tot} [-]	$\sigma_{RS} = E \cdot \varepsilon_{tot}$ [MPa]
3-2-1	0.00111	0.00067	0.00003	0.00090	182.18
3-1-2	-0.00014	-0.00004	0.00000	-0.00009	-18.72
3-1-3	-0.00011	-0.00019	0.00000	-0.00015	-30.43
3-1-4	-	-0.00021	0.00000	-0.00011	-43.82
3-1-5	-0.00016	-0.00024	0.00000	-0.00020	-41.43
3-1-6	-0.00017	-0.00016	0.00000	-0.00017	-33.96
3-1-7	-0.00016	-0.00011	0.00000	-0.00014	-27.85
3-1-8	-0.00015	0.00014	0.00000	0.00000	-0.84
3-1-9	-0.00001	-0.00012	0.00000	-0.00006	-13.13
3-1-10	-0.00009	-0.00006	0.00000	-0.00008	-15.58
3-1-11	-0.00003	-0.00008	0.00000	-0.00006	-11.48
3-1-12	0.00000	-0.00008	0.00000	-0.00004	-8.47
3-1-13	-0.00016	0.00001	0.00000	-0.00007	-15.02
3-1-14	-0.00007	-0.00006	0.00000	-0.00006	-12.61
3-1-15	-0.00019	-0.00001	0.00000	-0.00010	-20.52
3-1-16	-0.00027	-0.00002	0.00000	-0.00014	-29.52
3-1-17	-0.00017	-0.00009	0.00000	-0.00013	-27.43
3-1-18	-0.00006	0.00003	0.00000	-0.00002	-3.84
3-1-19	0.00001	0.00006	0.00000	0.00004	7.39
3-1-20	-0.00009	0.00009	0.00000	0.00000	0.03
3-1-21	0.00006	-0.00007	0.00000	0.00000	-0.84
3-1-22	-0.00003	-0.00006	0.00000	-0.00004	-9.02
3-1-23	-0.00017	0.00005	0.00000	-0.00006	-12.89
3-1-24	-0.00004	0.00007	0.00000	0.00002	3.57
3-1-25	-0.00004	0.00005	0.00000	0.00001	1.11
3-1-26	0.00012	0.00006	0.00000	0.00009	18.58
3-1-27	-0.00011	0.00015	0.00000	0.00002	4.70
3-1-28	-0.00011	0.00001	0.00000	-0.00005	-10.09
3-1-29	-0.00012	0.00009	0.00000	-0.00001	-2.97
3-1-30	0.00145	0.00068	0.00001	0.00107	218.89

Table 6-7 Residual stress measurement X-ray diffraction in depth on bottom part.

Depth [mm]	σ_{RS} Seg. 1-2-15 [MPa]	σ_{RS} Seg. 1-2-7 [MPa]	σ_{RS} Seg. 2-1-7 [MPa]
0	-520	-327	-110
50	-468	-447	-
100	-534	-556	-
150	-524	-517	-
200	-425	-375	-84
250	-538	-106	-
300	-	-	-9
330	-477	-65	-
380	-333	-70	-
460	-146	-41	-
500	-	-	-83
600	14	-59	-92
660	93	-54	-
760	44	-327	-

Table 6-8 Residual stress measurement X-ray diffraction in depth on top part.

Depth Seg. 1-2-15 [mm]	σ_{RS} Seg. 1-2-15 [MPa]	Depth Seg. 1-2-7 [mm]	σ_{RS} Seg. 1-2-7 [MPa]	Depth Seg. 2-1-7 [mm]	σ_{RS} Seg. 2-1-7 [MPa]
0	-402	0	-311	0	-36
50	-518	-45	-329	-50	-78
130	-525	-150	-467	-150	-54
190	-584	-250	-538	-200	-65
280	-482	-340	-372	-250	-60
350	-454	-440	-131	-300	-60
450	-271	-500	-113	-350	-65
650	-176	-540	-88		
700	-153	-600	-94		
800	-99	-650	-72		

Table 6-9 Residual stress measurement X-ray diffraction on waterjet cut surface.

Measurement position [mm]	σ_{RS} Seg. 1-2-7 [MPa]	σ_{RS} Seg. 1-2-15 [MPa]
1.5	-76	-88
2.5	3	-64
3.5	-26	-60
4.5	-25	-47
5.5	-50	-52
6.5	24	16
7.5	13	26
9	-14	-6
11	16	-11
13	-7	-28
14	8	43

Dimensions of parametric columns

Table 6-10 Dimensions of section 1.


 QS1	Number x width x thickness [- x mm x mm]	f_y or f_{ck} [MPa]	$N_{pl,Rk}$ [kN]	$N_{pl,Rk,i}/N_{pl,Rk,tot}$ [-]	$E_i \times I_i$ [kN/cm ²] x [cm ⁴]	$(E_i)/\sum(E_i)$ [-]
Tubular section	244.5 x 12.5	890	89 x 91	0.30	20,200 x 6,147	0.65
Laminated plates	2 x 56 x 20 2 x 120 x 20 2 x 150 x 20 2 x 160 x 20	960	96 x 194	0.69	20,500 x 2,969	0.25
Concrete	-	25	2.5 x 184	0.01	2,068 x 8,966	0.10
Total			27,417	1.00	192,459,802	1.00

Table 6-11 Dimensions of section 2.

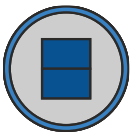
QS2 	Number x width x thickness [- x mm x mm]	f_y or f_{ck} [MPa]	$N_{pl,Rk}$ [kN]	$N_{pl,Rk,i}/N_{pl,Rk,tot}$ [-]	$E_i \times I_i$ [kN/cm ²] x [cm ⁴]	$(EI)_i/\Sigma(EI)$ [-]
Tubular section	168.3 x 8	890	89 x 40	0.40	20,200 x 1,297	0.712
Laminated plates	2 x 65 x 40	960	96 x 52	0.56	20,500 x 277	0.155
Concrete	-	25	2.5 x 130	0.04	2,068 x 2,364	0.133
Total			8,903	1.00	36,780,085	1.00

Table 6-12 Dimensions of section 3.

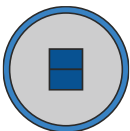
QS3 	Number x width x thickness [- x mm x mm]	f_y or f_{ck} [MPa]	$N_{pl,Rk}$ [kN]	$N_{pl,Rk,i}/N_{pl,Rk,tot}$ [-]	$E_i \times I_i$ [kN/cm ²] x [cm ⁴]	$(EI)_i/\Sigma(EI)$ [-]
Tubular section	244.5 x 12.5	890	89 x 91	0.58	20,200 x 6.147	0.94
Laminated plates	2 x 65 x 40	960	96 x 52	0.36	20,500 x 277	0.04
Concrete	-	25	2.5 x 326.4	0.06	2,068 x 11.118	0.02
Total			13,917	1.00	152,854,360	1.00

Table 6-13 Dimensions of section 4.


QS4 	Number x width x thickness [- x mm x mm]	f_y or f_{ck} [MPa]	$N_{pl,Rk}$ [kN]	$N_{pl,Rk,i}/N_{pl,Rk,tot}$ [-]	$E_i \times I_i$ [kN/cm ²] x [cm ⁴]	$(EI)_i/\Sigma(EI)$ [-]
Tubular section	355.6 x 16	890	89 x 170.7	0.24	20,200 x 24,663	0.60
Laminated plates	2 x 130 x 40 2 x 220 x 40 2 x 260 x 40	960	96 x 488	0.75	20,500 x 11,883	0.29
Concrete	-	25	2.5 x 334.45	0.01	2,068 x 41,945	0.10
Total			62,876	1.00	828,529,360	1.00

Table 6-14 Dimensions of section 5.


 QS5	Number × width × thickness [- × mm × mm]	f_y or f_{ck} [MPa]	$N_{pl,Rk}$ [kN]	$N_{pl,Rk,i}/N_{pl,Rk,tot}$ [-]	$E_i \times I_i$ [kN/cm ²] × [cm ⁴]	$(EI)_i/\sum(EI)$ [-]
	Tubular section	457 × 25	890	89 × 340	0.26	20,200 × 79,415
Laminated plates	2 × 160 × 40 2 × 260 × 40 2 × 320 × 40 2 × 350 × 40	960	96 × 872	0.73	20,500 × 48,171	0.36
Concrete	-	25	2.5 × 429	0.01	2,068 × 86,523	0.06
Total			114,982	1.00	2,770,614,343	1.00

Table 6-15 Lengths of the parametric columns in cm.

	$\bar{\lambda} = 0.5$	$\bar{\lambda} = 0.75$	$\bar{\lambda} = 1.0$	$\bar{\lambda} = 1.25$	$\bar{\lambda} = 1.5$	$\bar{\lambda} = 2.0$
QS1	124 + 8	189 + 8	257 + 8	322 + 8	387 + 8	517 + 8
QS2	92 + 8	142 + 8	192 + 8	242 + 8	292 + 8	392 + 8
QS3	152 + 8	235 + 8	317 + 8	392 + 8	472 + 8	637 + 8
QS4	182 + 8	278 + 8	373 + 8	468 + 8	563 + 8	754 + 8
QS5	236 + 8	358 + 8	482 + 8	602 + 8	722 + 8	967 + 8